PhD-FSTC-2017-40
The Faculty of Sciences, Technology and Communication
Physics and Materials Science Research Unit

Self-assembly of binary colloidal nanocrystals

Dissertation

Presented on 05/07/2017 in Luxembourg

to obtain the degree of

Docteur de l'université du Luxembourg

en physique

by

Marko Mravlak

Dissertation defense committee

Dr. **Tanja Schilling**, Dissertation supervisor
Professor, Albert-Ludwigs Universität Freiburg

Dr. **Tobias Kraus**
Professor, Universität des Saarlandes

Dr. **Jan Lagerwall**, Chairman
Professor, Université du Luxembourg

Dr. **Paul van der Schoot**
Professor, Technische Universiteit Eindhoven & Universiteit Utrecht

Dr. **Ludger Wirtz**
Professor, Université du Luxembourg

'We shall not cease from exploration, and the end of all our exploring will be to arrive where we started and know the place for the first time.'

T. S. Eliot

Abstract

The synthesis of functional nanoparticles is an important step in the hierarchical construction of hybrid materials for nanotechnological applications. A useful path to build these components is to use colloidal nanocrystals that can spontaneously agglomerate into ordered structures under confinement. The focus of this thesis is to explore the diversity of superstructures that can be self-assembled using binary dispersions where the dispersed colloids have spherical or quasi-spherical shapes and interact through simple potentials with repulsive cores and short-range attractions. Using computer simulations we demonstrate that agglomeration experiments with heterogeneous binary mixtures of nanoparticles can be exploited for the synthesis of structured clusters which are proposed as potential intermediate building blocks in hierarchical self-assembly of colloidal molecules and crystals.

To describe the structural properties of aggregates resulting from confined mixtures of particles with heterogeneous attractions we analyse the structure diagrams of binary Lennard-Jones clusters by means of a basin-hopping global optimisation approach for a broad range of cluster sizes, compositions and interaction energies and present a large database of minimal energy structures. We identify a variety of structures such as core-shell clusters, Janus clusters and clusters in which the minority species is located at the vertices of icosahedra.

For a binary mixture with heterogeneous particle diameters we use molecular dynamics simulations to demonstrate that pressure-dependent inter-particle potentials affect the self-assembly route of the confined particles. This is in agreement with experiments where crystalline superlattices, Janus particles, and core-shell particle arrangements form in the same dispersions for moderate changes in the working pressure or the surfactant that sets the Laplace pressure inside the droplets. Comparison of experimental analysis and simulations confirms that the onset of self-assembly depends on particle size and pressure.

Finally, we explore regular superlattices into which clusters can arrange by investigating the equilibrium phase behaviour for a monodisperse system of Mackay icosahedra. Monte Carlo simulations show that either a fluid phase, a crystal phase or rotator phases with different degrees of rotational correlations form. We analyse the correlations using the positional and orientational pair correlation functions and find that the densest lattice packing of hard icosahedra is stable at finite temperatures.

Contents

Chapter 1

Introduction

1.1 Colloidal dispersions

A colloidal dispersion is a mixture of small particles, droplets or bubbles dispersed in the surrounding medium which can also be either solid, liquid or gas. The dispersed units, often called *colloids* themselves, have at least in one direction the dimension in a range from 1 nm to around 1 μm and are significantly larger than the molecules of the continuous phase in their surrounding [1]. A wide range of materials that we encounter in our everyday life are colloidal dispersions, from consumer products such as inks, paints, toothpaste, mayonnaise, ketchup, ice cream, whipped cream to biological fluids such as milk and blood [2]. They constitute an important category under study in the field of *soft condensed matter* physics alongside polymers, surfactants and liquid crystals [3]. What do all these seemingly different materials have in common? As explained by de Gennes in his Nobel Lecture their complexity and flexibility are two major features that characterise these systems which are sometimes accordingly called *complex fluids* [4]. They are complex because their building units, for example colloidal grains, are themselves made of thousands of smaller parts such as atoms and molecules. The second common aspect is flexibility which means that drastic changes in their properties can occur under small adjustments of external conditions, for example they are easily deformed by moderate external fields or forces. It is immediately evident that such materials have significant applications in industry, e.g. in development of novel materials for biomedical and optoelectronic applications, but they are also important as model systems in theoretical and experimental physics.

One essential property of colloids and other building parts of complex fluids can be seen by examining a dilute colloidal dispersion under the microscope where we observe a continuous and random jiggling motion of dispersed particles which is a consequence of collisions with the molecules in their environment. This phenomenon is called *Brownian motion* after the botanist Robert Brown who first described it in a system of plant pollen in 1827 [5]. It

enables particles to move around and explore different configurations in a dispersion which consequently facilitates a system to move towards the equilibrium state and leads to another key concept in the study of soft matter called *self-assembly* that will be introduced in section 1.1.1. The dispersed particles that are to be governed by thermal fluctuations and undergo random motion first have to stabilise the gravity otherwise if they are density unmatched with the surrounding medium they can either rise to the surface and cream or sediment to the bottom of the container. The effects of gravity are minimised and can be ignored when the dispersed particles are small enough. This is typically true in the approximately submicron size range which defines the upper limit for the length scales of the building blocks in soft matter systems.

An extremely large area of interface between the dispersed phase and the surrounding medium and the corresponding interfacial energy distinctly characterises colloidal systems. It seems natural that the dispersed particles should tend to reduce this energy by combining and forming a larger aggregate. Indeed, the term colloid, which was coined by a chemist Thomas Graham in 1861, is derived from its Greek meaning *glue-like* since the particles he studied were unable to pass through a fine membrane but instead stuck to it [6]. From the point of view of interaction with the ambient medium the colloids can form two distinct thermodynamic states. Solutions are thermodynamically stable states representing a global minimum in the free energy which is typically the case when the dispersed particles are well matched in properties such as density and refractive index to the continuous phase. More often, however, the dispersed units are not soluble in the surrounding medium and prefer to phase separate, but due to different means of kinetic stabilisation, this does not happen, and instead a non-equilibrium suspension is formed representing a local minimum in the free energy landscape [7].

Small colloidal particles that are influenced by random, Brownian motion can collide with each other and form aggregates due to attractive interactions between them. This can be prevented by making them repel each other which can be achieved, for example, using stabilisation charges on their surfaces. Another way to make dispersed particles more compatible with the continuous phase is by steric stabilisation using surfactant brushes on their surfaces. Such repulsive forces are providing kinetic stabilisation to colloidal suspensions which are in turn characterised as a thermodynamically unstable state.

1.1.1 Self-assembly

A tendency of a system composed of micrometer- and submicrometer-sized components to spontaneously organise into well-defined, ordered structures is called *self-assembly* [8]. This term is usually reserved for building blocks that arrange themselves through weak forces such as hydrogen bonds or van der Waals interactions, and hard-core particles with excluded volume interactions. However, in a broader sense it can also include the ordering of particles

that interact with covalent bonds as in the crystallisation of atomic solids. External forces such as electric or magnetic fields can also be used to drive or enhance the ordering of building blocks but this has to be contrasted with serial manipulation where individual particles are dragged into final positions. Self-assembly is a key construction principle used by nature to fabricate the complex machinery of the living matter to incredible perfection which frequently relies merely on simple interactions and mechanisms [9]. Some noticeable examples from biological systems include the self-assembly of DNA [10], formation of micelles, bilayers and vesicles from amphiphilic molecules [11], aggregation and folding of peptides and proteins [12], bio-molecular machines and motors [13], and cellular membranes and scaffolds [14, 15]. In nature self-assembly often proceeds in a hierarchical fashion, e.g. in viruses where highly regular capsids are made of genetic material structured into proteins [16]. In colloidal science a typical example of self-assembly is the spontaneous formation into ordered crystalline structures, for example in opal films [17], or into one of the several liquid crystalline mesophases that can be found in solutions of surfactants or block copolymers. Many similar phenomena have fascinated scientists from different disciplines to develop experiments to mimic them, and as they often express the close connection between biology, chemistry, material science and physics they prompted unavoidable interdisciplinary collaboration in the domain of modern soft condensed matter physics.

The expression self-assembly is nowadays so ubiquitous that is has almost replaced the more precise thermodynamic term, i.e. the minimisation of the system's free energy during relaxation of the initially disordered state to a potentially ordered final equilibrium state. It is however more specific in that it commonly refers to a situation where the final structure is composed of finite size aggregates such as micelles that form spontaneously under appropriate external conditions. In general, a system will relax into a thermodynamic equilibrium that corresponds to a minimum of the appropriate thermodynamic potential, such as the Helmholtz free energy for a system at constant volume and temperature,

$$F = U - TS \,, \tag{1.1}$$

where the system's interaction energy is U, its temperature T and its entropy S. Colloidal particles under the influence of random Brownian motion are mobile enough to explore different positions and come into contact with the other surrounding particles. In this way the colloidal dispersion can explore different configurations and eventually find the minimum of free energy. In order for a system to reach such a state it has to be able to efficiently explore the free energy landscape and in principle seek through all the possible configurations of the system or efficient pathways such as 'folding funnels' have to exist. This is also known as the ergodic hypothesis in statistical mechanics which states that time averages over the single trajectory are equivalent to ensemble averages, and forms the foundation of the theory

of statistical mechanics. From (1.1) we see that temperature serves as a weighting factor for contributions of entropy S and internal energy U to the the free energy F. Self-assembly can thus be driven by either energy or by entropy, or at appropriate temperature, by a combination of both. An example of a system where self-assembly is driven by entropy alone is the formation of colloidal crystals composed of particles interacting through only hard core interactions. These so called entropy-driven phase transitions were first predicted by Lars Onsager for a system of hard rods where under compression rods align and form a nematic phase as a consequence of the increase of their translational entropy [18]. Nevertheless, when the first computer simulations reported that hard-spheres form crystal lattices upon freezing they were met with large scepticism in the scientific community where many established scientists were convinced that attractions are necessary for crystal ordering [19]. After solid experimental evidence for crystallisation in nearly hard-sphere PMMA colloidal spheres [20] the idea of entropy-driven phase transitions is nowadays widely accepted and has even become a rule for designing sophisticated ordered phases in systems with hard particles of various shapes [21].

1.1.2 Nanocrystal self-assembly

Nanocrystals are composed of inorganic cores which are fragments of metal, semiconductor or dielectric crystals and protected by organic ligand layers that are bound to the core's surface. A schematic example is shown in Figure 1.1. In recent decades a constant development

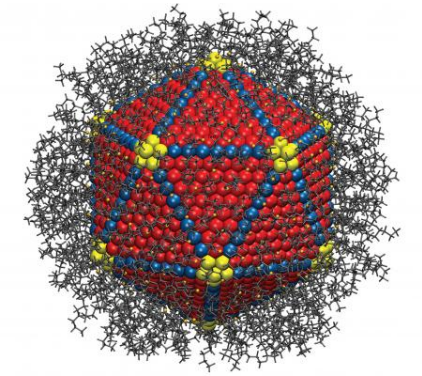

Figure 1.1: An illustration of how one of the leading scientist in the field of the chemical synthesis of inorganic nanostructures imagines a representative colloidal nanocrystal. Taken from the website of The Dmitri Talapin Group, The University of Chicago, 2017.

in nanoparticle chemistry [22] has made accessible new methods for preparing nanocrystals of uniform sizes with a range of inorganic cores of various shapes such as spheres, polyhedra, rods, plates and branched shapes with tunable surface chemistries [23]. Individual colloidal nanocrystals are Brownian objects which can form ordered arrays known as superlattices that self-assemble under appropriate conditions without external direction. Different synthesis strategies can be employed to encourage nanocrystal self-assembly (Figure 1.2).

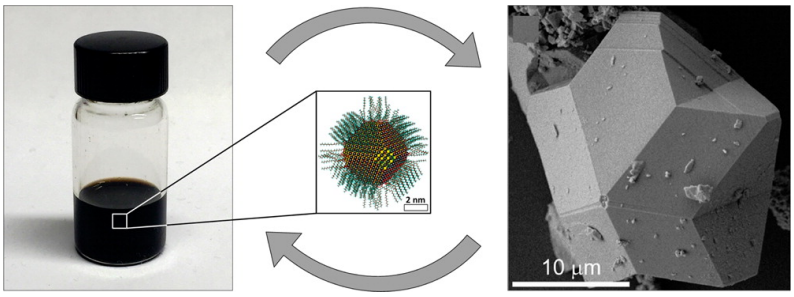

Figure 1.2: In a typical nanocrystal self-assembly experiment individual colloidal particles arrange into close-packed superlattices during the process of solvent evaporation which increases their packing fraction. As the particle interactions are weak this procedure can be reversed by reintroducing the solvent [23].

In solvent evaporation based techniques superlattices form as the dispersion of particles becomes more concentrated and their volume fraction increases. This can be achieved, for example, in droplets of nanocrystal solution deposited on flat, solid supports where particles are trapped at the air-liquid interface [24], on lithographically patterned surface templates [25] or by confinement in emulsion droplets [26]. Another approach includes solvent destabilisation where effective attractive interactions appear as the capping ligand is made less compatible with the solvent e.g. by increasing the polarity of the solvent for nanocrystals with hydrocarbon-based ligands [27] or by slowly introducing hydrophobic ligands on nanocrystals dispersed in water [28]. Ordering can also appear from gravitational sedimentation where large enough particles accumulate on the bottom of the solution under the influence of gravity when their gravitational energy is comparable with their internal energy due to thermal fluctuations (thermal energy). Aggregation of nanocrystals is induced by other means such as by cooling the solution, desorption and cross-linking with capping ligands [23].

Aggregation of nanocrystals is determined by their assembly environment and by the inter-particle interactions. Among them an important role is played by the relatively weak van der Waals interactions whose energy is typically comparable to the thermal energy at room temperature. As they do not repress the thermal motion of particles and their reconfigurations during self-assembly they are more suitable than much stronger ionic interactions and covalent or metallic bonds [3]. Van der Waals interactions are a consequence of fluctuations in electron distributions of atoms and molecules that usually lead to isotropic attractive forces between nanocrystal cores. They are a combined effect of London dispersion interactions between the induced dipoles which are produced by spontaneous fluctuations in the electron clouds, Keesom interactions between freely rotating permanent dipoles and Debye interactions between permanent and induced dipoles [29]. Treating van der Waals interactions at the nanoscale is a nontrivial problem [30] but calculations become more feasible when assuming pair-additive interaction with an effective coarse grained potential between two atoms

of the form $\Phi(r) \sim r^{-6}$ which can be derived for London forces by quantum-mechanical perturbation theory [31]. An analytic expression for two spherical particles of radii R_1 and R_2 in this approximation was derived by Hamaker [32] by integrating over spheres' volumes

$$U_{\mathrm{vdW}} = -\int_{V_1} \mathrm{d}V_1 \int_{V_2} \mathrm{d}V_2 \frac{C\rho_1\rho_2}{r^6} = -\frac{A}{3}\left[\frac{R_1R_2}{r^2-(R_1+R_2)^2} + \frac{R_1R_2}{r^2-(R_1-R_2)^2} + \frac{1}{2}\ln\left(\frac{r^2-(R_1+R_2)^2}{r^2-(R_1-R_2)^2}\right)\right], \quad (1.2)$$

where ρ_1, ρ_2 are number densities of atoms for each sphere, C is the pair interaction coefficient and $A = \pi^2 C\rho_1\rho_2$ is the Hamaker constant. At very small surface distances, $d = r - R_1 - R_2 \ll R_1, R_2$, this expression slowly decreases as $1/d$ leading to a large attraction while for large distances, $r \gg R_1, R_2$, it reproduces $1/r^6$ behaviour. At smaller distances the particles start to feel a steep repulsive potential due to the Pauli exclusion principle of the overlapping electron clouds which can be well described by an exponential function [33] but is for mathematical convenience often approximated by inverse power laws of high orders such as $1/r^{12}$ which leads to the phenomenological Lennard-Jones 12-6 potential that describes the interaction between small, neutral atoms and molecules

$$\Phi^{\mathrm{LJ}}(r) = 4\epsilon\left[\left(\frac{\sigma}{r}\right)^{12} - \left(\frac{\sigma}{r}\right)^{6}\right], \quad (1.3)$$

where σ measures the size of the particles and ϵ the strength of van der Waals interactions. Interactions between charged-stabilised particles can be approximately described by the DLVO theory attributed to Derjaguin, Landau, Verwey and Overbeek [34] where hard-core, van der Waals and Coulomb interactions are combined

$$\Phi_{\mathrm{DLVO}}(r) = \Phi_{\mathrm{hc}}(r) + \Phi_{\mathrm{vdW}}(r) + \Phi_{\mathrm{C}}(r). \quad (1.4)$$

However, the interaction between two nanocrystals is in reality much more complex because of the presence of the flexible polymer shells that consist of grafted hydrocarbons or DNA [35]. For colloidal nanocrystal solutions to remain well dispersed at low concentrations in the presence of attractive van der Waals interactions their surfaces need to be either sterically stabilised with e.g. hydrocarbon ligands such as alkanes [36] or electrostatically stabilised with charges [37]. This provides an effective repulsive pair potential even for particles with metallic cores that have large Hamaker constants. In the case of steric stabilisation with grafted ligands the repulsive interactions depend on the curvature of grafting surfaces and originate from osmotic repulsion as a consequence of the removal of solvent molecules as the ligands begin to overlap and from elastic contributions of compressed ligand layers at smaller separations [34].

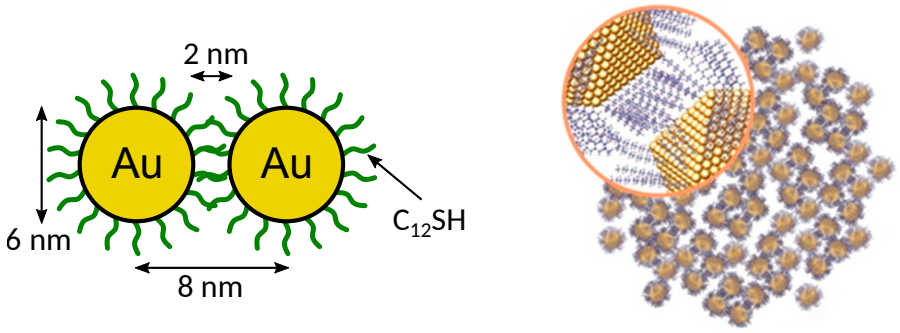

Figure 1.3: Interaction potentials between two nanocrystals with metallic cores and hydrocarbon capping ligand shells are complex and sensitive to many factors such as core shape and size, grafting surface curvature and bond strength, shell thickness, solvent, temperature [42]. Left: typical diameters, ligand lengths and centre separations in a superlattice of gold nanocrystals are shown. Right: interdigitation of grafted ligands upon removal of the solvent (reproduced with permission from [43]).

The resulting total steric interaction energy between polymer-grafted particles is a complex combination of individual ligand contributions that depend sensitively on the properties of particle faceting, polymer brush coverage, solvent molecules and temperature [38, 39]. Currently no established coarse-grained models exist as mode ling of such surface interactions remains an actively researched area, especially for the case when thickness of ligand layers is comparable to the particle diameters [40–42].

When particles are forced together at high packing fractions during self-assembly by solvent evaporation or when no good solvent is present the surface covering polymer chains are no longer interacting with solvent molecules and instead as a consequence of van der Waals attractions form close-packed crystalline domains [43]. The interdigitation of ligands in nanocrystal superlattices could play an important role in promoting the formation of different structures which have been estimated for binary mixtures using simple geometric overlap models [44], soft inverse power law potentials [45] and even treating the deformability capping ligands on the surface of spheres as a set of topological defects [46].

Self-assembly of nanocrystals into superlattices depends on multiple factors such as interparticle interactions, assembly environment and possibly pre-programmed ordering instruction that can be included in nanocrystals coated with DNA based surface ligands [47, 48] This leads to a variety of ordered nanocrystal solids that can be formed and new opportunities in bottom-up self assembly of nanomaterials with specific properties for optical [49], electronic [50], catalytic [51] and mechanical [52] applications. Controllable and tunable assembly of such materials is one of the main goals in nanoscience [53]. As nanocrystals are relatively simple systems with mostly two types of building blocks that can form ordered structures their diversity in structures and size is important in providing a variety for functional materials in nanotechnological applications. If the nanoparticles themselves are composed of several

materials or have internal structure, they offer broader structural and compositional complexity than homogeneous particles, which makes them particularly interesting for material science [54, 55]. Useful internal structures are e.g. core-shell architectures, but also nonspherical symmetries, the directional functionality of which is especially important when the particles are used as building blocks in directed self-assembly [56]. For example structured bimetallic clusters on the surface of optically transparent media provide transformed transmission spectrum, modified plasmonic resonance regimes [57–59].

1.2 Molecular simulations

Molecular simulations are computational methods that can be employed to predict the thermodynamic, structural and dynamical properties in classical many-body systems composed of particles such as atoms and molecules [60–62]. There are two distinct classic approaches for molecular simulations. The first are Monte Carlo simulations which are based on repeated random sampling where usually static configurations of a system are generated. The second are molecular dynamics simulations where deterministic Newton's equations of motions with added stochastic contributions are solved to determine the motion of particles. The average of a function of coordinates and momenta $A(\mathbf{r}^N, \mathbf{p}^N)$ of a many-particle system is computed in two distinct ways, either by time averaging over a phase trajectory (molecular dynamics, denoted as $\bar{A}$) or by averaging over an ensemble of systems (Monte Carlo, denoted as $\langle A \rangle$). If we assume the ergodic hypothesis the two averages should give the same result:

$$\bar{A} = \lim_{\tau \to \infty} \frac{1}{\tau} \int_0^\tau A\left[\mathbf{r}^N(t), \mathbf{p}^N(t)\right] \, \mathrm{d}t \tag{1.5}$$

$$= \iint A(\mathbf{r}^N, \mathbf{p}^N) f_0^{[N]}(\mathbf{r}^N, \mathbf{p}^N) \, \mathrm{d}\mathbf{r}^N \, \mathrm{d}\mathbf{p}^N = \langle A \rangle \,, \tag{1.6}$$

where $f_0^{[N]}(\mathbf{r}^N, \mathbf{p}^N)$ is the equilibrium probability density of the phase space. We should, however, be aware that many systems, such as glasses and metastable phases, are not ergodic and the above averages are not the same. Originally these algorithms were designed in the 1950s and 1960s in the US government laboratories and afterwards they have been continuously developed by the scientific community into many different variants. They have been applied extensively in studies of liquid matter to find exact solutions in systems described by chosen potential models. This was possible because the properties of macroscopic systems could often be described using only a few hundred particles. With computer power becoming more accessible evermore complex and detailed systems can be studied using molecular simulations. In the following the principles on which both approaches operate are going to be presented in more detail.

Treatment of physical systems using computer simulation lies in-between experiments and more traditional analytic theoretical methods [63]. In the physics community this approach is sometimes described as quasi-experimental and the simulations are referred to as computer experiments. It is often employed where the measurement data is rare because experimental treatment is out of reach and when analytic calculations are not feasible. In studies of colloidal systems both reasons are often present, for example when studying crystallisation mechanism in a system of binary nanoparticle mixtures we need to consider a complex collection of equations of motion which is analytically unfeasible and colloid dynamics is difficult to be captured by experimental image tracking methods as well.

1.2.1 Monte Carlo

Monte Carlo methods [64] are a class of stochastic computational algorithms that rely on repeated random sampling to compute their results. Their essential idea is to use randomness to solve problems that might be deterministic in principle. A typical Monte Carlo method follows a particular pattern: at first it defines the domain of all possible configurations and then it generates configurations randomly from a probability distribution over this domain. The third part is to perform a deterministic computation on the configurations and finally aggregate the results. The name of the method was coined in 1947 when Stanislaw Ulam suggested to John von Neumann that the newly developed ENIAC computer would give them the means to carry out calculations based on statistical sampling. Their coworker Nicholas Metropolis dubbed the numerical technique the Monte Carlo method partly inspired by Ulam's gambling uncle who 'just had to go to Monte Carlo'.

A simple example of a Monte Carlo method is integration using direct sampling, e.g. a calculation of the area of a circle by generating random, uniformly distributed trial points inside the circumscribed square. In this case we are sampling the uniform probability distribution $\pi(\mathbf{x})$. The area of the circle is then determined by the ratio of the number of trial points inside the circle and the number of all trials, multiplied by the area of the square. To evaluate the observable $O(\mathbf{x})$ which has in this example value 1 inside the circle and 0 elsewhere we calculate its average value

$$\frac{N_{\text{hits}}}{\text{trials}} = \frac{1}{N}\sum_{i=1}^{N} O_i \approx \langle O \rangle = \frac{\int_{-1}^{1} \mathrm{d}x \int_{-1}^{1} \mathrm{d}y \; \pi(x,y) O(x,y)}{\int_{-1}^{1} \mathrm{d}x \int_{-1}^{1} \mathrm{d}y \; \pi(x,y)} \,. \tag{1.7}$$

We notice that on the left side of the equation for the statistical average of observable $\langle O \rangle$ the integrals and the probability distribution $\pi(x,y)$ are not present. However, we have to be able to generate random samples according to the desired probability distribution $\pi(\mathbf{x})$. Using the Monte Carlo method we can thus evaluate in general very complex higher dimensional

integrals that we usually meet in statistical mechanics but in a much more convenient way.

Direct sampling approach can be very inefficient, especially when we are sampling a probability distribution in a higher dimensional phase space which is not a uniform function but is wildly varying. This is usually the case when we sample the Boltzmann distribution for a typical intermolecular potential. In the case of a dense liquid the probability distribution is also vanishingly small for the overwhelming majority of configurations, therefore a better way of sampling is needed. In such cases the efficiency can be improved by using importance sampling where an integrable function is constructed with a similar shape to the distribution function so that we sample many points in the regions where probability distribution is large and fewer elsewhere. However, the importance sampling method requires one to know the rough shape of the probability distribution function *a priori*, which can be difficult to estimate and is often not realistic with large configuration space, as for example in the case of the Ising model. In general it is more practical to construct *Markov chain Monte Carlo* algorithms (MCMC) for which the equilibrium distributions are the desired non-uniform high dimensional distributions whose efficient sampling is provided.

The basic idea of the MCMC method is to sample random configurations from a target probability distribution $\pi(\mathbf{x})$. This is achieved by constructing a Markov chain of configurations ν_i with a stationary distribution equal to $\pi(\mathbf{x})$. To make sure that MCMC converges to the equilibrium distribution we have to design a proper transition matrix $p(\nu \to \nu')$. The obvious condition for equilibrium distribution is that transition matrix elements do not destroy it once it is reached, i.e. the probability to leave state a should be equal to the probability of coming to state a from all the other states. But it is often more convenient to impose a much stronger condition that the probability to move from a to any other state is the same as the reverse probability. This stronger condition, called the *detailed balance*, renders our Monte Carlo algorithm consistent with the prescribed probability distribution.

In general we want to draw samples from a given probability distribution $\pi(\mathbf{x})$ which we achieve by constructing a Markov chain with the appropriate equilibrium distribution. One way to do this is using the *Metropolis-Hastings* algorithm which accepts a proposed move from configuration a to b with the probability [65]

$$p(a \to b) = \min\left[1, \frac{\pi(b)}{\pi(a)}\right] . \tag{1.8}$$

To follow the target distribution in such a chain the detailed balanced condition, $\pi(a)p(a \to b) = \pi(b)p(b \to a)$, has to be satisfied. We can check this by considering the acceptance probabilities $p(a \to b)$ and $p(b \to a)$ from where it follows that in both cases, when $\pi(a) > \pi(b)$ and $\pi(b) > \pi(a)$, the detailed balance condition is satisfied.

Usually the transition $a \to b$ is separated into two steps: at first, we propose a state b given

a with an *a priori* probability $\mathcal{A}(a \to b)$, and then we decide whether to accept this move with acceptance probability $p(a \to b)$. Thus, the total probability for the transition of $a \to b$ is

$$\mathcal{P}(a \to b) = \mathcal{A}(a \to b) \cdot p(a \to b) \ . \tag{1.9}$$

According to the detailed balance condition the probabilities of moving from a to b and vice versa are equal, $\pi(a)\mathcal{P}(a \to b) = \pi(b)\mathcal{P}(b \to a)$, so the acceptance probability should obey

$$\frac{p(a \to b)}{p(b \to a)} = \frac{\pi(b)}{\mathcal{A}(a \to b)} \frac{\mathcal{A}(b \to a)}{\pi(a)} \ . \tag{1.10}$$

Comparing the above equation with equation (1.8) we immediately obtain the acceptance probability of the generalised Metropolis algorithm [66]

$$p(a \to b) = \min \left[1, \frac{\pi(b)}{\mathcal{A}(a \to b)} \frac{\mathcal{A}(b \to a)}{\pi(a)} \right] . \tag{1.11}$$

For a sample of independent variables, $\{\xi_1,\ldots,\xi_N\}$, the error of the sample average is estimated according to the central limit theorem as

$$\text{error} = \frac{1}{\sqrt{N}} \sqrt{\frac{1}{N} \sum_i \xi_i^2 - \left(\frac{1}{N} \sum_i \xi_i \right)^2} . \tag{1.12}$$

As the values in a sample generated by a Markov chain can be correlated, the sample size N should be replaced by the effective number of independent variables in a sample. The error in MCMC methods therefore decreases only as $1/\sqrt{N}$ and is not linearly correlated with the available computer power.

The MCMC method is useful for fast computation of complex integrals in diverse problems but there are also limitations and traps that have to be taken into account. If a simulation is supposed to describe properties of macroscopic systems then we can expect some deviation from results when only a finite number of particles is used. In this case periodic boundaries are typically applied which means that unphysical spatial and time correlations may appear in the system. This can be avoided using larger systems and an application of finite size effects analysis. Another difficulty is the quasi-ergodic problem where the system is trapped in a subspace of the phase space. Millions of samples generated in a MCMC simulation could correspond to only a handful of independent configurations and in the worst case, there are no independent samples are created in the limit of infinite computing time. This is the case for nonergodic algorithms where the configuration space gets divided into sectors that are symmetry protected and not captured in the update scheme. Another problem appears when rare configurations exist which contribute to the averages in an important way.

In the canonical ensemble we can apply this approach to calculate ensemble averages of static observables $O(\mathbf{r}^N)$ that do not depend on the momenta of particles by calculating

$$\langle O \rangle = \frac{\int \mathrm{d}\mathbf{r}^N O(\mathbf{r}^N) \exp\left[-\beta U(\mathbf{r}^N)\right]}{\int \mathrm{d}\mathbf{r}^N \exp\left[-\beta U(\mathbf{r}^N)\right]} \ . \tag{1.13}$$

Here $U(\mathbf{r}^N)$ is the potential energy in system where number of particles N, volume V and temperature T are constant. $\mathbf{r}^N$ and $\mathbf{p}^N$ are the positions and momenta of particles with mass m whose dynamics is described by the Hamiltonian of the system

$$H(\mathbf{r}^N, \mathbf{p}^N) = \sum_{i=1}^{N} \frac{\mathbf{p}_i^2}{2m} + U(\mathbf{r}^N) \ . \tag{1.14}$$

We apply the principle of MCMC method demonstrated in Equation (1.7) to calculate this complex, high-dimensional integrals efficiently. The system is advanced from an old state $\mathbf{r}^N_{\mathrm{old}}$ to a new state $\mathbf{r}^N_{\mathrm{new}}$ by generating trial moves which usually consist of random displacements and rotations for nonspherical particles. Trial moves can be accepted or rejected according to the Metropolis-Hastings rule from Equation (1.8) which gives in this case

$$\mathrm{acc}\left(\mathbf{r}^N_{\mathrm{old}} \to \mathbf{r}^N_{\mathrm{new}}\right) = \min\left\{1, \exp\left(-\beta\left[U(\mathbf{r}^N_{\mathrm{new}}) - U(\mathbf{r}^N_{\mathrm{old}})\right]\right)\right\} \ . \tag{1.15}$$

To sample configurations in different ensembles new trial moves are introduced with different acceptance probabilities. For the NPT ensemble, where pressure P is constant, a trial move is introduced that attempts to change the volume of the simulation box from V_{old} to V_{new} with the probability

$$\mathrm{acc}\left(V_{\mathrm{old}} \to V_{\mathrm{new}}\right) = \min\Big\{1, \exp\Big(-\beta\Big[U(\mathbf{r}^N_{\mathrm{new}}) - U(\mathbf{r}^N_{\mathrm{old}}) + P(V_{\mathrm{new}} - V_{\mathrm{old}})\Big] - N\log(V_{\mathrm{new}}/V_{\mathrm{old}})\Big)\Big\} \ . \tag{1.16}$$

This normally includes changing the three dimensions of the simulation box independently but it can as well include varying the angles of the box. This leads to a parallelepiped of changing shape during the simulation that releases stresses related to nonorthogonal unit cells when simulating crystal phases [67]. In a similar fashion the grand canonical ensemble μVT with a constant chemical potential μ can be simulated by introducing moves that attempt inserting and removing new particles to the simulation box [61].

1.2.2 Molecular dynamics

In classical molecular dynamics methods [68] special techniques are used to numerically integrate Newton's equations of motion for a system of interacting particles. Molecular dynamics methods are in principle completely deterministic and have to be distinguished in this aspect from the stochastic methods used in the Monte Carlo approach. As dynamical evolution of particle positions and velocities is available these methods are typically more suitable for studying transport properties of classical many-body systems. It is also inherently parallel as forces on each atom can be computed simultaneously and positions and velocities can be updated simultaneously as well. Therefore they can be implemented as parallel calculations on a large number of computing units enabling inspection of larger system sizes and longer time evolutions.

After initial positions and velocities have been assigned to all the particles, and the boundary conditions defined, the forces on particles are calculated from the gradient of their interaction energies with all the neighbouring particles inside a local region

$$m_i \ddot{\mathbf{r}}_i = \mathbf{F}_i = -\nabla_{\mathbf{r}_i} V \,, \tag{1.17}$$

where m_i is mass of the particle i, $\mathbf{F}_i$ the total force acting on it and V the potential energy in a system. For N particle this gives a set of $3N$ coupled differential equations of the second order. The calculation of forces acting on each particle is the most time consuming part of the simulation. When model systems contain only pairwise interactions which act on a short range we only have to consider interactions between a particle and its nearest neighbours figures. In such cases efficient techniques exist to speed up the calculation of forces so that the time needed for their evaluation scales linearly with system size N. The interactions are cut off at a suitable range and then a list of neighbours which are within a slightly larger radius is made. At further times only forces with the particles from these neighbours lists need to be computed. These are essentially bookkeeping techniques that maintain the neighbour and cell lists and can also be used in Monte Carlo methods for fast calculation of energies [61].

The set of equations (1.17) can be solved numerically using finite difference approximations for the derivatives where positions and velocities are calculated at incremented timesteps. There are several discretisation schemes available but one that is particularly useful is the velocity Verelet algorithm

$$\mathbf{r}_i(t + \Delta t) = \mathbf{r}_i(t) + \mathbf{v}_i(t)\,\Delta t + \frac{1}{2}\,\mathbf{a}_i(t)\Delta t^2 \tag{1.18}$$

$$\mathbf{v}_i(t + \Delta t) = \mathbf{v}_i(t) + \frac{\mathbf{a}_i(t) + \mathbf{a}_i(t + \Delta t)}{2}\Delta t \,, \tag{1.19}$$

where $\mathbf{v}_i$ and $\mathbf{a}_i$ are velocity and acceleration of particle i. This simple method is still a stand-

ard integration technique nowadays because it provides good numerical stability and time-reversibility but only requires low computational cost. The error for positions and velocities are of orders $(\Delta t)^4$ and $(\Delta t)^2$, therefore small timesteps are required to maintain sufficient precision. We also have to apply a different approach in case when simulating a system of hard particles. The trajectories between collisions of such particles are straight lines and new velocities are calculated from energy and momentum conservation's at elastic collisions. Instead of time stepping the collision events become important and the simulations are called event-driven molecular dynamics. At relatively low densities systems of larger numbers of hard particles can be simulated in this way.

So far we described an algorithm that simulates a system in the microcanonical ensemble, that is when the number of particles N, the system volume V and the system energy E are all held constant (NVE ensemble). To describe a different set of constraints, for example a system at fixed temperature T (canonical or NVT ensemble) we need to use a different method. The most common approach is to use a Nosé-Hoover thermostat where an additional degree of freedom is added to the system and plays a role of the reservoir [69, 70]. When the time integration is carried out with this imaginary particle the energy is extracted from the heat bath or inserted into it in such a way that system maintains a constant temperature. Time integration is performed on the extended system using equations

$$\ddot{\mathbf{r}}_i = \mathbf{F}_i/ms^2 - 2\dot{s}\dot{\mathbf{r}}_i/s\,, \tag{1.20}$$

$$Q\ddot{s} = \sum_i m_i\dot{r}_i^2 s - (f+1)k_BT/s\,, \tag{1.21}$$

where s is the new degree of freedom, f is the number of degrees of freedom, T is desired temperature. Q is an imaginary mass that represents the size of thermal 'ballast' and determines how rapidly the temperature is relaxed. It should be chosen carefully to tune the thermal lag and prevent wild thermal fluctuations, usually a good choice for many models is around 100 timesteps when scaled in timesteps.

1.3 Scope of this thesis

One route to the synthesis of nanoparticles with well-defined structures is the assembly of smaller building-blocks into supraparticles within emulsion droplets from which the solvent is then evaporated as depicted in Figure 1.4. A possible pathway to supraparticles with more complex internal structures is to mix two types of metallic nanoparticles in emulsion droplets. The resulting highly structured and symmetric colloidal nanocrystals may be technologically interesting as they could be used as building blocks in the design of novel functional materials. In this thesis we study different aspects in the self-assembly of spherical and quasi-spherical

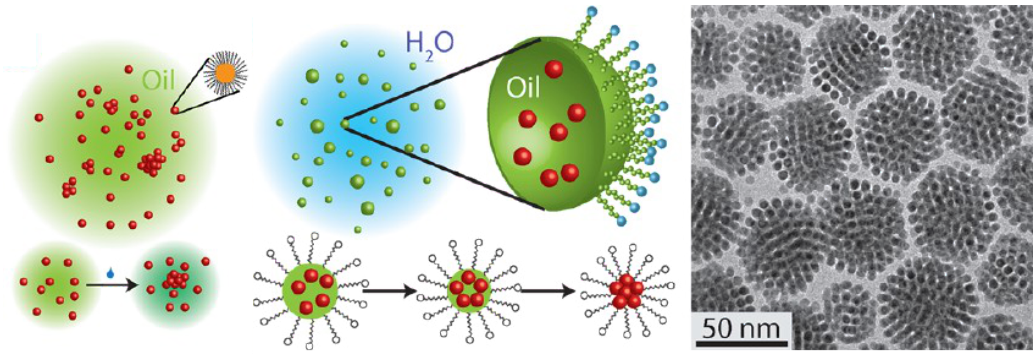

Figure 1.4: Synthesis of ordered clusters by self-assembly inside evaporating emulsion droplets. Left: gold nanoparticles covered with hydrocarbon capping ligands are dispersed inside oil droplets in a surfactant stabilised oil-water emulsion. During the evaporation of oil phase the dispersed nanoparticles are forced together by the shrinking droplets. Right: this process leads to structured clusters or supraparticles as shown here in a TEM image of gold nanoparticles with diameters around 6 nm. Reprinted with permission from [26]. Copyright 2012 American Chemical Society.

colloidal particles in such assembly protocols. We explore multiple ways of extending the simplest case of the crystallisation in a system of monodisperse and spherical hard-sphere colloidal particles to bimodal mixtures with a less steep potential and quasi-spherical particle shape. Different scenarios are possible during the self-assembly in e.g. a mixtures of particles of two different sizes as shown in Figure 1.5. Our goal is to predict what structures the supraparticles will assume and to understand the mechanism of their formation. As a first extensions we consider a binary mixture of particles with different attractions from the perspective of energy minimisation in chapter 2. In chapter 3 we study the second generalisation to a binary mixture of particles with different sizes and a softer potential at finite temperatures in a spherical confinement. At last we inspect the equilibrium phase behaviour of a mixture of Mackay icosahedra composed of the spheres with a WCA potential in chapter 4. Our studies are concerned with exploring novel equilibrium structures in such unimodal and bimodal colloidal suspensions, studying the formation mechanisms of complex binary lattices and the effects of the environment. This is achieved by studying systems of particles with a simple and general pre-defined inter-particle potentials using established methods of molecular simulations as well as more recent extensions to the basin-hopping algorithm.

In chapter 2 we consider the structures in a binary Lennard-Jones mixture of spherical particles with heterogeneous attractions from a global energy minimisation approach. The use of basin-hopping Monte Carlo method enables us to locate the global minima in a transformed potential energy landscape and then analyse the corresponding structures. The structure diagrams for a broad range of cluster sizes, compositions and interaction energies are analysed and results are collected in a large database of minimal energy structures. Scanning the structural phase diagram for clusters composed of two particle species enables us

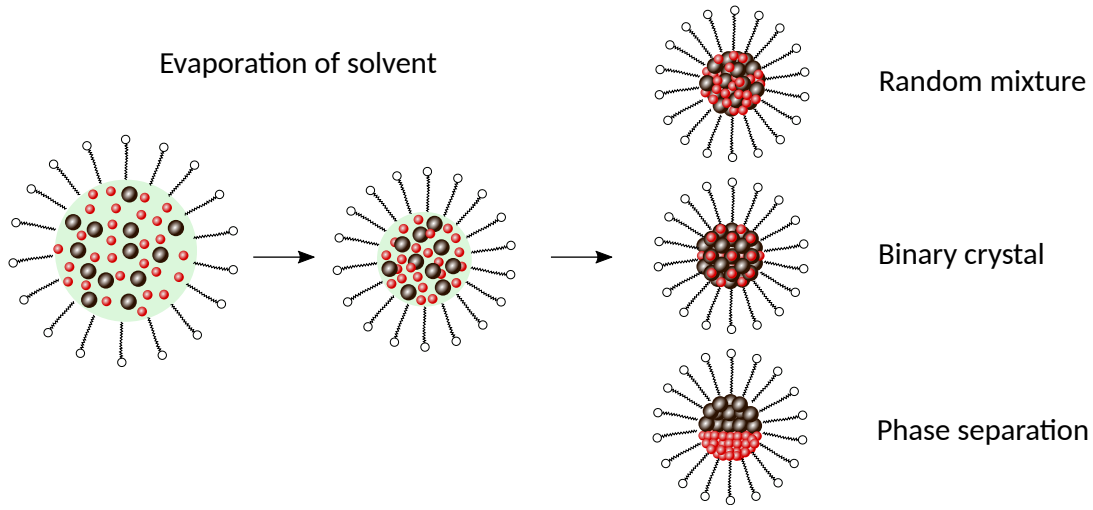

Figure 1.5: Agglomeration of binary mixtures of colloidal particles in shrinking emulsion droplets could results in a random mixture, a binary crystal or in phase separated supraparticles. This are a few simple possible scenarios while in reality the effects of environment and agglomeration dynamics can render the situation much more complex.

to predict parameters for which the ground state has symmetries that are interesting in the context of colloidal molecules and crystals. We determine the factors that influence the formation of clusters with specific properties and find a variety of structures such as core-shell clusters, Janus clusters, and clusters in which the minority species is located at the vertices of icosahedra. In the future experiments with nanocrystals made of different metallic cores and self-assembled inside emulsion droplets such clusters could be synthesised and if suitably functionalised they could be used as building blocks in colloidal molecules or crystals.

In chapter 3 we consider self-assembly in a binary mixture of nanoparticles with two different diameters where experiments have shown that distinct regular superlattices can form depending on the surfactant used when creating oil-in-water emulsion or by moderate differences in the atmospheric pressure. The formation mechanism explaining this behaviour is presented where pressure changes the inter-particle potentials and drives the formation of different structures during self-assembly in a confining droplet. We conduct molecular dynamics simulations of spherical particles confined in spherical confinement using a bimodal size distribution and interaction potentials based on a combination of WCA and Lennard-Jones potentials. Different interaction potentials corresponding to different pressure regimes are shown to lead to the formation of crystalline superlattices, Janus particles, and core-shell particle arrangements. Optical spectrometry, small-angle X-ray scattering and electron microscopy are used to compare experiments and simulations and confirm that the onset of self-assembly depends on particle size and pressure.

In chapter 4 we test the equilibrium phase behaviour for a Mackay icosahedron that results from energy minimisation of the Lennard-Jones clusters and is a common nanocrystal shape

(Figure 1.1). Icosahedra are modelled as nonlinear polyatomic molecules composed of a set of Lennard-Jones subparticles arranged on a surface of the Mackay icosahedron and studied using Monte Carlo simulations in isothermal-isobaric ensemble with periodic boundary conditions and a variable simulation box shape. Initially ordered or disordered states equilibrate into either a fluid phase, a crystal phase or a rotator phase where different degrees of rotational correlations are present. The densest lattice packing for hard icosahedra is stable at specific parameters. The correlations in equilibrated states are studied by the positional and orientational pair correlation functions. At large enough temperatures Mackay icosahedra exhibit similar behaviour as systems of hard icosahedra in which the densest lattice packing and the rotator crystal phase have been reported before. Here we confirm that both of these phases can form at finite temperatures as well. New behaviour is observed at low temperatures where energetic interactions result in preferred face to face alignment forming rotator crystal or presumably unidentifiable complex crystal arrangements. This leads to the re-entrant behaviour with increasing temperature where first a transition to the densest lattice crystal occurs and then the rotator phase is formed at higher temperatures due to the prevailing excluded volume effects.

Chapter 2

Structure diagrams of minimal energy binary Lennard-Jones clusters

Agglomeration experiments in emulsion droplets with monodisperse gold nanoparticles have shown that the structures of the resulting clusters correspond to the minimal energy Lennard-Jones structures. Here we study an extension to binary mixtures of nanoparticles with different attractions and employ a global optimisation approach to compute the structure diagrams for binary clusters of Lennard-Jones particles. We analyse a large range of cluster sizes, compositions and interaction energies and present a database of 180,000 minimal energy structures which is publicly accessible at `http://softmattertheory.lu/clusters.html`. A variety of structures has been identified among which the core-shell clusters, Janus clusters and clusters in which the minority species is located at the vertices of icosahedra are the most interesting. As such clusters can be synthesised from nanoparticles in agglomeration experiments they could be used as building blocks for colloidal molecules or crystals. We present the basin-hopping Monte Carlo method that was used to find the global minima and discuss the factors that determine the formation of clusters with specific structures.

2.1 Introduction

Structured particles are small, regular arrangements of two or more dissimilar components. Such particles have been created, for example, by condensing the vapours of two metals into binary clusters [71]. These clusters had diameters in the nanometer range and uniform structures that minimised their energy [72]. Colloidal particles can also be assembled into structured clusters, so-called 'supraparticles' that have diameters between nanometers and micrometers. Recently developed self-assembly protocols yield macroscopic quantities of structured supraparticles that are interesting building blocks for materials [54, 55, 73]. Core-shell or Janus particles with anisotropic interactions and valences spontaneously arrange into materials with defined microstructures [74] or act as surfactants [75, 76]. It is conceivable that such combinations can also lead to interesting plasmonic and catalytic behaviour.

In the case of colloids, the minimal energy configuration is not necessarily always reached. Some assemblies are kinetically trapped and depend on the history of supraparticle formation. This effect can be exploited to tailor certain supraparticle structures [77–80]. However, there are several protocols of colloidal assembly that are dominated by energy minimisation. Gold nanoparticles in suitably stabilised hexane droplets assemble into clusters with structures that are strikingly similar to the global minima of Lennard-Jones clusters [26]. Also van Blaaderen and co-workers report large, regular nanoparticle clusters formed inside droplets [81].

So far, no structure diagram has been available to predict which arrangements different particles will assume to minimise their energy. Nanoparticles come with very different sizes and interactions, but existing diagrams are limited to very small subsets. The aim of our work is to produce a large data base of minimal energy structures for clusters composed of two particle species, and to scan this structure diagram in order to predict parameters for which the ground state has symmetries that are interesting in the context of colloidal molecules and crystals.

2.2 Model

2.2.1 Nanocrystal interactions

Nanoparticles used in agglomeration experiments inside emulsion droplets consist of semiconductor, metallic or magnetic crystal cores which are separated by ligand monolayers to distances where attractive forces between the cores become small enough and their energy comparable to the characteristic thermal energy of the system (k_BT). Tethering long hydrocarbon surfactants to nanoparticle surfaces thus renders them stable against flocculation and enables them to function as a balanced colloidal suspension in non-polar solvents such as hexane [82]. The pair potential between nanoparticles which is predominantly repulsive in a

dilute state gradually becomes attractive during the process of self-assembly where the nanoparticles are slowly brought closer together and eventually into contact with one another by the process of the removal of solvent. At the end of this process the solvent is mostly dried out and the nanoparticles are firmly linked together into a superlattice by the interpenetrating surface ligands whose mutual van der Waals attractions provide a deep potential well that greatly exceeds system's thermal energy. The assembly that proceeds at near equilibrium conditions provides sufficiently long times during which the attractive pair interactions are comparable to thermal energy which allows the nanoparticles to sample the possible configurations before settling irreversibly and therefore facilitates the formation of equilibrated superlattices [83].

Organic surfactant molecules tend to lower the free energies of organic-inorganic interfaces and thus get absorbed to the surfaces of metallic nanoscale objects where they form self-assembled monolayers similar to those in the well-known system of alkanethiols on gold [84]. As self-assembled monolayers are easy to prepare and form on objects of all sizes and shapes they have become an essential part of nanotechnological systems where they are commonly used for stabilisation and to add new functions by providing a number of parameters for tuning the interaction of surfaces with the environment. For example, self-assembled alkanethiol and organo-silicon monolayers have been used to greatly enhance the performance of organic field-effect transistors used in organic electronics and biosensing devices [85].

Around half a century ago polymer scientists elucidated the mechanisms by which non-ionic polymer chains provide stability to colloidal particles [86]. When two such sterically stabilised colloidal particles, dispersed in a good solvent, are brought at the distance where their ligand coronas start to interact they begin to exhibit a repulsive force. Due to the negative free energy of ligand-solvent mixing, the exclusion of solvent molecules from the interaction zone results in the osmotic repulsion between the ligand chains. This is essentially a solvent effect where chemical potential of solvent in the interaction region is smaller than that in the external bulk phase which causes solvent molecules to flow from the bulk phase into the interaction zone and thus force particles apart. At smaller particle separations the compression of ligand chains results in a large elastic contribution to the potential energy which is often not very important when considering Brownian collisions.

The steric stabilisation of nanocrystals has proven to be a more complex phenomenon, also because these objects are much smaller and the thickness of their ligand monolayers is comparable to the diameters of crystal cores. The interaction of two polymer molecules in solution, as treated by the Flory-Krigbaum theory [87], depends on the volume available to the ligands and therefore on the grafting surface curvature. It is often assumed that surface ligands cover the central particle in a uniform shell, but on the nanocrystal cores with a varying curvature and faceting of the grafting surface this is not the case and can lead to a strong anisotropic behaviour of steric repulsion between nanoparticles [88]. The formation of chain-chain bundles

of ligands are considered an important contribution to the melting enthalpy which imparts the solution processability of nanocrystals [89]. Another important aspect is the crystallisation of the ligand chains after the removal of solvent molecules from the interaction zones in the late stage of nanocrystal self-assembly which is due to the van der Waals attractions between the monomers of the hydrocarbon chains. Different packing of hydrocarbon chains result in different interparticle separations and could raise constrains on the resulting nanocrystal superlattices. Multiple models have been proposed that treat the interdigitating hydrocarbon coronas with simple geometric space-filling approach or as topological defects and a good agreement has been reached by predicting the relative stability of candidate binary superlattices (e.g. the AB_{13} crystal lattice) while some models indicate the importance of many-body interactions [45, 46, 90].

However, a precise calculation of the total interaction potential energy between two nanocrystals which is the sum of the individual ligand-ligand interactions has not been established. Molecular dynamics simulations with all-atom and coarse-grained force fields have been employed to estimate effective ligand-mediated interparticle potentials and concluded a number of contributing factors, from the size, faceting and surface curvature of the core, to the ligand length, grafting density, bonding strength, their mobility and collective behaviour, as well as solvent properties and temperature [38, 40, 44]. We are thus dealing with a rather complex system of nano-objects interacting through a combination of various contributions that in practice all compete, whose relative importance remains unknown, that evolve during the self-assembly process and exhibit nonlinear and non-additive coupling [91]. In reality, a system contains an inhomogeneous collection of nanocrystals, nonuniform environment and finite-size solvent molecules that would all have to be considered in an accurate description.

A rigorous characterisation of the effective interaction potential between nanoparticles is desired for the theoretical and simulations treatment but has proven to be a difficult task which remains a subject of intense active research, a more in-depth discussion of which is given in several reviews [23, 92, 93]. Subsequently there seems to be a strong focus on systems with more controllable ligand interactions such as on DNA-functionalised nanoparticles where complementarity of DNA strands is used to guide the assembly of superlattices [47, 48]. Another approach with larger colloidal particles is to produce directional attractions through depletion interaction by varying the surface roughness of the particles [94, 95]. To enable the treatment of systems of nanocrystal-ligand objects severe simplifications on the nanocrystal shapes and interactions have to be made. Individual studies have found that nanoparticles in such systems behave as hard spherical colloids or that their morphology is driven by a generic pair potential, which often turns out to dominate during the ordering transition and to correctly predict the formation of superlattices. For example, hard spheres in spherical confinement have been shown to form icosahedral or rhomboicosidodecahedral clusters and FCC

lattices [81], while homogeneous minimal energy Lennard-Jones clusters have been used to explain superlattices of gold nanocrystals [26]. Here we follow a similar approach and assume a simplifying coarse-grained potential at the disorder-order transition and spherical nanocrystal shapes.

2.2.2 Energy driven agglomeration

Experiments by Lacava, Born and Kraus with a homogeneous dispersion of ligand-passivated gold nanoparticles with core diameters of 6 nm have demonstrated that the self-assembly by evaporation of solvent from emulsion droplets leads to structures that closely resemble the geometries of the minimal energy Lennard-Jones clusters [26]. In this case, the oil-in-water emulsion was created using Triton X-100 surfactant while the nearly monodisperse nanoparticle cores were stabilised with dodecanethiol monolayers leading to effective diameters of 8.92 nm (after interdigitation). A slow evaporation that took typically 240 min which is much longer than the diffusional equilibration time of the nanoparticles created a quasi-static, near-equilibrium situation at the increasing concentrations [96]. A comparison of the transmission electron microscopy figures of ten supraparticles of different sizes and the corresponding projections of numerically calculated global minima of Lennard-Jones clusters is shown in Figure 2.1.

Good matching is observed in a broad range of numbers of confined nanoparticles, from a very small cluster of only a few ten nanoparticles to much larger clusters containing more than a thousand nanoparticles. Various different cluster morphologies are observed which are similar to those of rare gases and metals [97], such as clusters based on a central icosahedron with a Mackay overlayer (FCC growth) or an anti-Mackay overlayer (HCP growth), complete Marks decahedron, and an icosahedron core with a Mackay overlayer and a central vacancy. Although numbers of encapsulated nanoparticles in the inspected supraparticles are small enough that the icosahedral structural motif is energetically the most stable ones [98], the details of predicted cluster structures depend sensitively on the form of the interaction potential and the precise number of constituent particles [72, 99, 100]. Therefore it is unlikely that these observations distinguishing detailed structures such as clusters with Mackay and anti-Mackay overlayers in supraparticles of different sizes could be explained by ordering merely due to entropic reasons as found more recently in analogous experiments [81]. However, systematic experiments with a more precise characterisation of the structures of small and intermediate-sized clusters, possibly enabling three-dimensional comparison, would be necessary to make more elaborate conclusions on the relative importance of the energetic contributions in agglomerated structures.

The observations of minimal energy clusters also indicate that the total energy of a system of confined nanoparticles can be described by a sum of all the pair interactions between

them. Conversely, many-body effects can become important when nanoparticles with passivating ligand layers on their surfaces are closely packed [101]. Nevertheless, as concluded in Ref. [26], in evaporating emulsion droplets particles are mobile enough "to find their energetically optimal position in the increasingly dense, non-agglomerated mobile precursor state *before* they are finally quenched when their ligand shells interdigitate". If there are also no important contributions to the surface energy of clusters by encapsulating emulsion droplets, as for example in the case of microparticles confined to the liquid-liquid interface [78], we conclude that the interactions between the nanoparticles in this type of experiment can be modelled by effective Lennard-Jones interactions and that the interactions are strong in comparison to the thermal energy, such that the ground state is formed at room temperature.

This simple description of colloidal particles in spherical confinement as pairwise interacting Lennard-Jones particles in free space where the confinement is provided by the energy minimisation principle enables us to explore and study the features of the extended cases of more general colloidal systems such as heterogeneous clusters. In this work we will focus on modelling binary colloidal clusters assembled from metallic nanoparticles of the same diameter and different van der Waals attractions. Such clusters could be assembled in similar experiments of agglomeration inside emulsion droplets from a mixture of two metallic nanoparticles or quantum dots that exhibit effective differences in their dispersion attractions.

2.2.3 Binary Lennard-Jones clusters

To describe the pair interaction in a suspension of colloidal nanoparticles in spherical confinement at low temperatures we use the Lennard-Jones potential [102]. This simple and generic potential describes colloidal particles with dispersion interactions and short range repulsion in the form of inverse power laws with scaling exponents of 6 and 12, respectively. We use this interaction potential because of the experimental conclusions described in the previous section and because it describes generic features of interactions in simple liquids [3] although we are aware that this form of the dispersion attraction is precise for molecules or atoms of simple neutral gases such as argon [103] and that better models exist to describe colloidal interactions, such as the DLVO theory [104]. .

For the heterogeneous Lennard-Jones clusters, where particles can have different sizes and interactions strengths, the total energy is

$$E_{\mathrm{tot}}^{\mathrm{BLJ}}(\mathbf{R}) = 4\epsilon_{\alpha\beta} \sum_{i=1}^{N-1} \sum_{j=i+1}^{N} \left[\left(\frac{\sigma_{\alpha\beta}}{r_{ij}} \right)^{12} - \left(\frac{\sigma_{\alpha\beta}}{r_{ij}} \right)^{6} \right] . \tag{2.1}$$

Here the summation is done over all the pairs of particles in the cluster and thus the total energy is a function of the coordinates of all N particles in a cluster, $\mathbf{R} = \{\mathbf{r}_1, \mathbf{r}_2, \ldots, \mathbf{r}_N\}$. The

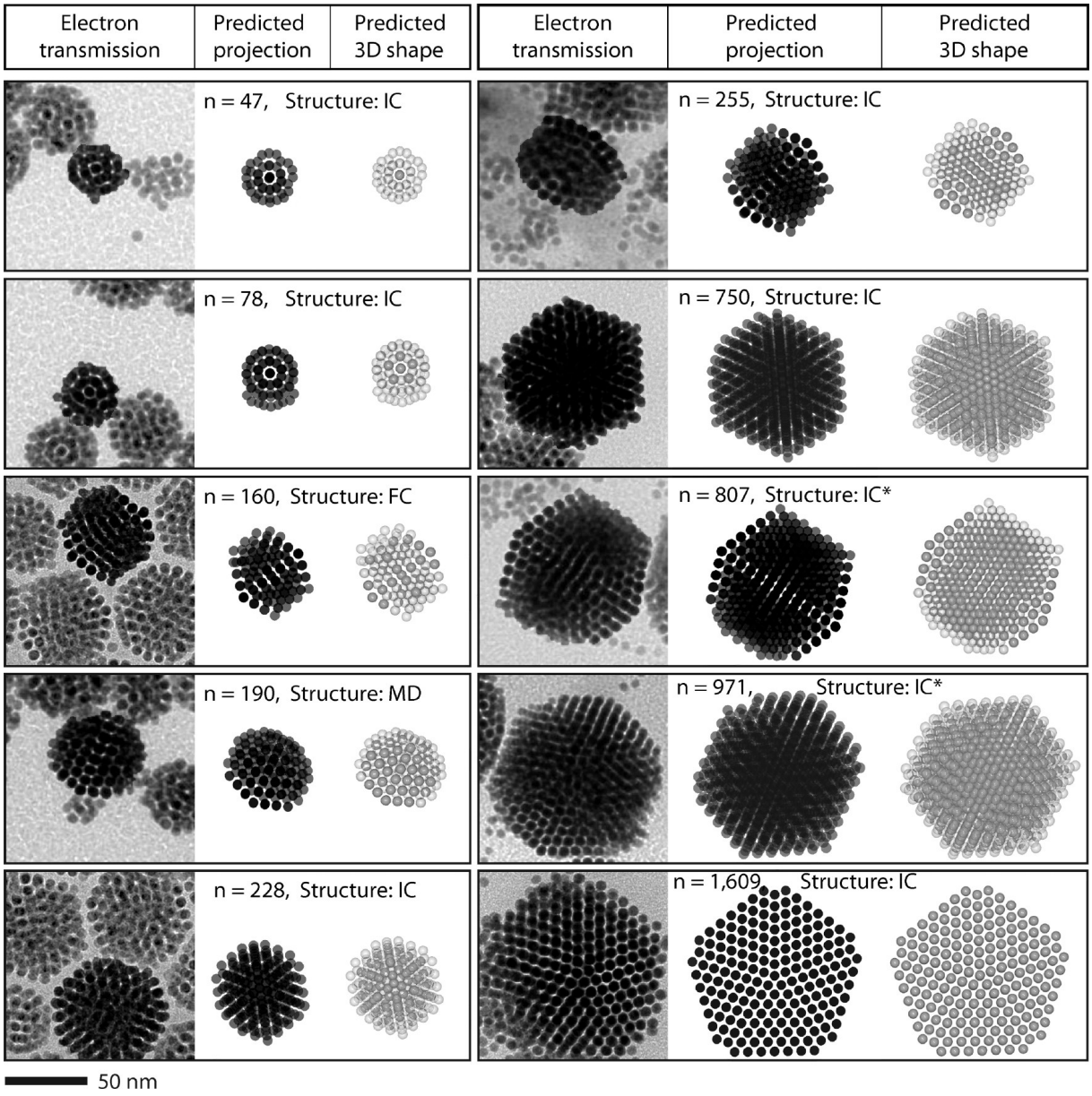

Figure 2.1: Experimental observations of supraparticles consisting from different numbers of confined gold nanoparticles in comparison to projections of homogeneous minimal energy Lennard-Jones clusters. Transmission electron micrographs show arrangements of nanoparticles after the self-assembly process driven by the evaporation of solvent from a suspensions of nanoparticles with grafted hydrocarbon ligands inside emulsion droplets. Structures of clusters are based on central icosahedron with a Mackay overlayer (IC), anti-Mackay overlayer (FC), Mackay overlayer and a central vacancy (IC*) and Marks decahedron (MD). This striking resemblance led to our study of a generalised heterogeneous supraparticles. Reprinted with permission from [26]. Copyright 2012 American Chemical Society.

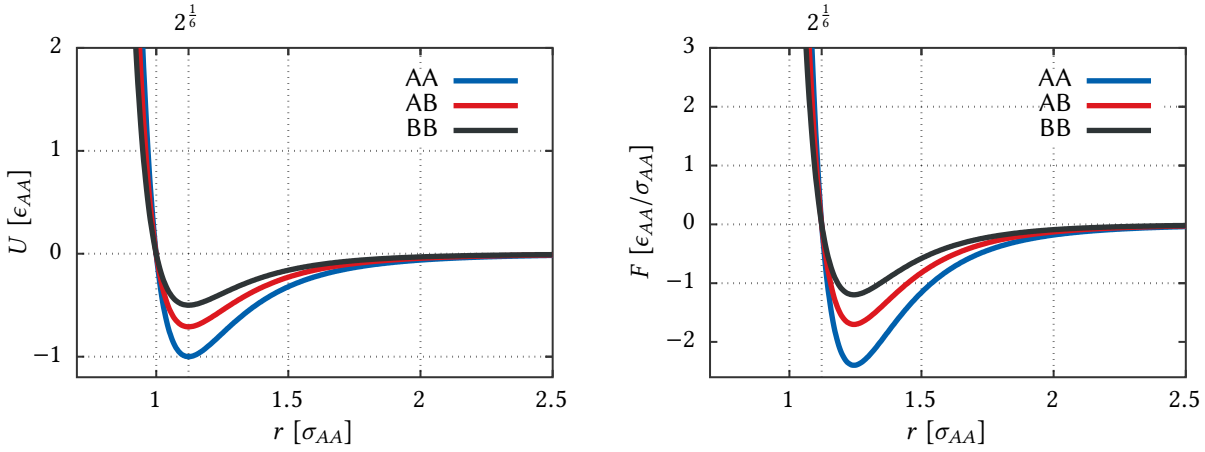

Figure 2.2: The binary Lennard-Jones pair potential and the corresponding force magnitudes as used to model a mixture of spherical particles whose attractions differ by a ratio of one half. The energetic parameters are $\epsilon_{BB} = 0.50$ and $\epsilon_{AB} = 0.71$ whereas the sizes of both nanoparticle types are the same, $\sigma_{AA} = \sigma_{BB} = \sigma_{AB}$.

range and the attraction magnitudes of the particle interactions are given by parameters $\sigma_{\alpha\beta}$ and $\epsilon_{\alpha\beta}$. The force acting on the particle i in the cluster is then expressed as a derivative of the potential energy

$$\mathbf{F}_i(\mathbf{R}) = -\nabla_{\mathbf{r}_i} E_{\text{tot}}^{\text{BLJ}} = 24\epsilon_{\alpha\beta} \sum_{i=1}^{N-1} \sum_{j=i+1}^{N} \left[2\left(\frac{\sigma_{\alpha\beta}}{r_{ij}}\right)^{12} - \left(\frac{\sigma_{\alpha\beta}}{r_{ij}}\right)^{6} \right] \frac{\mathbf{r}_{ij}}{r_{ij}^2} \,. \tag{2.2}$$

In the case of a binary cluster the system is composed of two different types of particles and the Lennard-Jones model is described by parameters ϵ_{AA}, σ_{AA}, ϵ_{BB}, σ_{BB}, ϵ_{AB}, σ_{AB}. To set the energy and length scales we can choose $\epsilon_{AA} = \sigma_{AA} = 1$ and the remaining parameters are the numbers of particles, N_A and N_B, which specify the size and the composition of a cluster with the total number of particles $N = N_A + N_B$. The binary Lennard-Jones model is therefore completely determined by a set of six parameters $\{N, N_B, \epsilon_{AB}, \sigma_{AB}, \epsilon_{BB}, \sigma_{BB}\}$. An example of the potential and the corresponding force in a binary cluster made of particles with the same size but different attractions is shown in Figure 2.2.

In this model there are no additional energy terms included and no extra constraints imposed thus we are calculating the structures of free clusters. More elaborate models should take into account further details of experimental situation, for example the interactions of colloidal particles with the surfactants forming confining emulsion droplets which could select among different types of particles in heterogeneous clusters.

2.3 Methods

Binary Lennard-Jones clusters have been used as a benchmarking system for global optimisation algorithms due to the mathematical complexity they pose to state of the art computational resources [105]. A common approach to solving this problem is the basin-hopping algorithm which is a Monte Carlo based method that produces an unbiased walk through a transformed potential energy surface, where in a specified number of Monte Carlo steps one hopes to reach the lowest minimum. The potential energy landscape is transformed into basins of attraction computed by a deterministic local optimisation method [100]. Such an algorithm performs well for homogeneous particle clusters but for multi-component systems additional combinatorial local minimisation steps are required to relax cluster configurations with respect to particle types. For this we apply another deterministic scheme similar to a graph partitioning approach which is then used to find the local biminima and consequently outperforms basic basin-hopping algorithm for binary clusters [105, 106].

To minimise the energy of binary clusters we use the implementation of basin-hopping global minimisation algorithms with positional and combinatorial local optimisation as provided by the GMIN program [107]. Here, we present a scan of the entire composition diagram of minimal energy binary Lennard-Jones clusters, i.e. a minimal energy structure for each possible choice of composition, for up to 200 particles for multiple sets of interaction parameters. In total, we have computed the global minima for 180,000 different energy landscapes.

2.3.1 Global optimisation in heterogeneous systems

To find the global energetic minimum of a many-particle system is a difficult mathematical problem. As the energy is a function of a large number of continuous variables which display many local minima, optimisation requires the use of advanced numerical methods [108–113]. Minimising energies of heteroparticle systems is even more complicated due to the large number of combinatorial arrangements [114, 115]. In addition, the less similar the particles are, the more difficult it is to find the global minimum as there are increasingly high energy barriers in the potential energy landscape [116, 117]. However, the total number of particles in the system remains the most important factor determining the computational effort.

For systems made of just one component the problem has been solved for up to hundreds of particles using unbiased optimisation algorithms. In contrast, for multi-component systems specificities of each system (e.g. the functional form of the interaction potential and the number of components) need to be taken into account when choosing the optimisation strategy. For the binary Lennard-Jones (BLJ) system, compositional minima for clusters of up to 100 particles with diameter ratios up to 1.3 and one fixed choice of interaction parameters have been computed [118, 119]. ‘Compositional’ means that not only the particle positions but also

the identities of the particles were varied in order to obtain minimal energies.

The problem of finding the global optimum in a system with multiple degrees of freedom appears in several fields of science and technology. In prediction of the crystalline structure of solid materials from their ab-initio total energy models the stable structure corresponds to the global minimum in the multidimensional free energy surface [120]. In the structural optimisation of nanoalloys the lowest energy structures in heterogeneous clusters of particles modelled with complex many-body potentials have to be identified [121]. In protein folding where the native structure has to be predicted from the amino acid sequences [122]. The problem of finding the ground state configurations of spin glasses reduces to the minimisation of a complex multidimensional hypersurface [123]. The problem is also encountered in microprocessor design and several other travelling salesman-type problems. Thus new algorithms leading to improved solutions in global optimisation have important implications for applications in catalysis, biotechnology, crystallography and elsewhere [108].

The aforementioned problems are usually best understood by studying the underlying potential energy landscapes [108]. These are multidimensional hypersurfaces which results from all the possible conformations of the system components. Energy landscapes become complex and nontrivial to globally optimise already for systems with a few tens degrees of freedom. The principal cause of difficulty arises from the large number of minima on the hypersurface. For example, in homogeneous Lennard-Jones clusters the number of minima has been shown by extrapolation to increase exponentially with the number of particles [124]. But the size of the system is not the only factor determining the problem difficulty. High energy barriers that prevent the algorithm to escape from local minima are present. Especially challenging are energy landscapes with several funnels in which the minimisation algorithm can get trapped and which require more effort than the larger systems with only one efficient funnel [125, 126].

Optimisation algorithms performing the exhaustive search on the energy surface are of limited usefulness due to the vast number of local minima and inability to overcome high energy barriers in the case of energy landscapes with a complex topography. Several methods, among those molecular dynamics, Monte Carlo, simulated annealing and parallel tempering, have not been able to locate global minima for Lennard-Jones clusters already at small sizes. Computational evolution of the system at finite temperature or simulated annealing will not succeed additionally due to the dissociation of global free energy and energy minima at very low temperatures where barriers are high [100]. This has led to introduction of several new computational and physical approaches in the algorithms for global optimisation.

Two classes of algorithms that are able to efficiently locate global minima in the homogeneous Lennard-Jones clusters prevail in the literature. The first are genetic algorithms [112, 113, 127, 128] that use evolutionary techniques and the other are the hypersurface transformation methods which perform a search on a transformed energy landscape [109, 129]. It is

characteristic for both of them to use local minimisation algorithms in order to produce new configurations and simplify the search space. In the case of global optimisation of nanoalloys their performance is comparable and none of them show significant disadvantages over the other [121]. In this work we choose to apply the method from the second class which is an unbiased algorithm that can be well adapted for optimisation of multi-component systems.

2.3.2 Basin-hopping algorithm

The energy of a cluster for a chosen set of parameters $\epsilon_{\alpha\beta}$ and $\sigma_{\alpha\beta}$ can be written as

$$E = f(\mathbf{r}_1, \mathbf{r}_2, \ldots, \mathbf{r}_N) \,, \tag{2.3}$$

where N is a number of particles in a cluster. Thus we have to find a global minimum $\mathbf{R}^*$ of a scalar function of $3N$ independent variables

$$\mathbf{R}^* = \{\mathbf{r}_1^*, \mathbf{r}_2^*, \ldots, \mathbf{r}_N^*\} \quad \text{where} \quad E = \min \,. \tag{2.4}$$

Global optimisation of a multidimensional scalar function poses a difficult mathematical problem that can only be successfully addressed by advanced numerical methods. One efficient approach to this problem is *basin-hopping* where a local energy minimisation algorithm is used to transform the original energy landscape into plateaus or catchment basins or basins of attraction [100, 109]. The energy transformation can be written as

$$\tilde{E}(\mathbf{R}) = \min\{E(\mathbf{R})\} \tag{2.5}$$

where the dependency on $\mathbf{R}$ in the notation indicates that the local energy minimisation starts out in the configuration point $\mathbf{R}$. The idea is to reduce the complexity of energy landscape by transforming nontrivial features of the potential into a collection of steps by a deterministic local optimisation method which does not change the relative energies of minima and leaves the global minimum intact. This is shown for the case of a one dimensional energy function in Figure 2.3. A search strategy based on Monte Carlo sampling is then used to explore the plateaus of a transformed energy landscape in an unbiased walk where in a specified number of Monte Carlo steps one expects to visit the lowest minimum. If the proposed Monte Carlo step has been accepted after the local minimisation the structure is reset to that of the current local minimum. This has been found to be more effective than allowing it to vary continuously [100, 129].

Metropolis scheme (as defined in Equation (1.8)) is applied in the search strategy as it drives the system towards configurations that are energetically more favourable while still allowing the acceptance of higher energy states. The acceptance rate of these steps that help

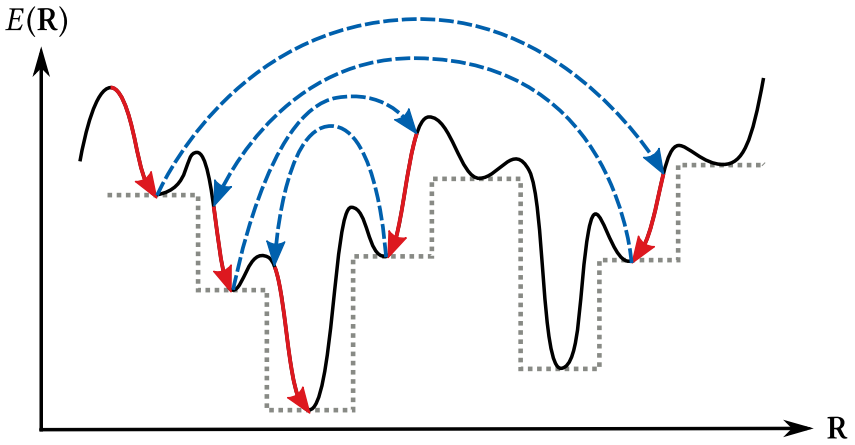

Figure 2.3: Schematic representation of the principle of basin-hopping Monte Carlo method. The grey dashed line represents the basins of a transformed potential energy surface. Red lines show how the local minimisation along a single dimension transforms initial configuration points into such steps. The blue dashed lines outlines one possible exploration of configuration space by Monte Carlo steps hopping between the catchment basins.

to overcome the barriers in the energy landscape is tuned by the temperature parameter as well as by the magnitude of the trial steps which have to generate all the possible conformations of the system. The described algorithm performs well for homogeneous Lennard-Jones clusters of up to several hundreds of particles [130].

In a binary cluster, composed of particles of two different species A and B, there are $N!/(N_A! \times N_B!)$ possible permutational isomers or *homotops* with the same positional configuration and different identity arrangements. This large combinatorial factor of distinct homotops greatly complicates the problem of finding the global minimum using stochastic search schemes. Basic basin-hopping approach combined with uniform or exponentially weighted random identity exchanges does not yield a significant performance increase for optimisation of binary clusters [105]. A more efficient approach is to use the second deterministic scheme as an identity counterpart to the local minimisation of particle positions and combine it with basin-hopping to transform initial energy landscape to the so called *biminima* - local minima in both coordinate and permutation space of heterogeneous systems. An efficient way to relax cluster configurations with respect to particle identities is based on Kernighan and Lin's graph partitioning heuristic [131]. In this greedy algorithm [132] a sequence of locally most favourable identity swaps is carried out, where swaps can be chosen in multiple ways. This identity optimisation is performed after each local minimisation of the particle positions (known as a *quench*). Such a scheme largely outperforms basic basin-hopping for binary clusters [106].

In the following, several aspects and details of the chosen numerical scheme are discussed and the chosen parameters are specified.

Temperature parameter The Monte Carlo algorithm runs at a fixed temperature T where the moves are accepted according to the standard canonical sampling using Boltzmann weights. The size of moves changes in order to achieve a desired acceptance ratio. Optimal temperature parameter depends on the potential parameters and the composition of clusters. We determine it by varying T and gathering statistics for several random starting configurations. The optimal value is at the shortest mean time for a given acceptance ratio and in general increases slightly with the cluster size. Here we used fixed temperature for the whole range of parameters and compositions used.

Initial condition and reseeding Initially we randomly generate N uniformly distributed points inside the unit cube. This is passed as an input to the program which transforms the initial configuration and energy by running the local minimisation algorithm in the positions space described in more detail below. Initial conditions can be used to seed the runs with previously optimised configurations of smaller clusters or clusters with different compositions. We did not use seeding in our calculations but rather chose a completely unbiased approach. However, Monte Carlo runs are reseeded with random configurations if the energy does not decrease in a specified number of steps.

Interaction potential We specify the potential function by setting the values of ϵ_{AB}, σ_{AB}, ϵ_{BB}, σ_{BB}, the size of a cluster N and the number of B type particles N_B. We do not use the cutoff distance in the calculation of the potential because we explore clusters made of only up to few hundred particles.

Spherical container and centring Before the move is attempted we check if all the particles are inside a defined container radius, otherwise we put them back in at the opposite end of a diameter by rescaling. A restriction to a spherical container is also taken into account in the local minimisation routine where particles are translated in such a way that a centre of mass lies at the origin. After the move is accepted we check again if the particles are out of the container otherwise we put them back by displacing them by a vector of length equal to the container diameter and pointing towards the origin.

Monte Carlo moves In a single Monte Carlo step we attempt to randomly displace each particle and after each attempt we make a local minimisation according to the positions and the identities of particles. We also perform angular steps where a particle is randomly placed on the sphere with a radius of the most distant particle from the centre of mass of the cluster. Angular steps are taken on particles whose binding energies are lower than that of the most tightly bound particle in a cluster multiplied by a proportionality constant which specifies a threshold for angular steps. We set the initial values of the magnitude of random displacements

and the angular threshold to 1.3 and 0.5 and then adjust their values during sampling in order to achieve the desired acceptance rate of 0.5. In the Monte Carlo method we use the search strategy where after a successfully accepted step the structure is reset to that of the current local minimum and not allowed to vary continuously.

Geometry relaxation (local minimisation in positions space) Local minimisation is performed by the limited memory Broyden-Fletcher-Goldfarb-Shanno (L-BFGS) minimisation algorithm of Liu and Nocedal [133, 134]. Local minimisation algorithm finds stationary points which are a set of variables where the function's first derivatives are zero. Newton's method identifies the stationary points by iteratively estimating displacement vectors for the function's first derivative using the Hessian matrix of the second derivatives. In the case of quasi-Newton methods the Hessian matrix of second derivatives does not have to be computed directly but it is instead approximated by the algorithm that updates it at every step using the information from successive gradient vectors [135]. Thus we only have to specify the Jacobian matrix of the first derivatives of our potential and the BFGS algorithm then uses a specific formula for the estimation of the Hessian matrix. While approaches based on the Newton's method converge well for functions with a quadratic Taylor expansion close to extrema, the BFGS method which uses only the first derivative is practical and effective even for optimisation of non-smooth functions [136]. The commonly used L-BFGS method is a limited-memory version of the BFGS method which is particularly suited to problems with very large numbers of variables (e.g., > 1000), while the L-BFGS-B variant can handle simple box constraints [137].

Combinatorial optimisation (local minimisation in identity space)

The optimal permutation of the current configuration is determined by an algorithm that is a variant of the Kernighan-Lin (KL) heuristic for graph partitioning [131]. It is performed after a Monte Carlo step is attempted and geometry optimisation has already been executed. In this algorithm we start with the current permutation and then identify the swap of the identities of two selected particles that is going to be executed next. We then execute this swap and remove the two affected particles from further consideration. Geometry is relaxed after each permutation to relieve the stresses in the cluster. We repeat this until there are no more particles left to swap or a different termination condition is met. The expensive part of the algorithm is determining the next swap of particles, which can be done in several ways [105].

In the exact KL scheme the next swap is chosen by calculating energy differences (swap gains) of all the possible identity swaps and then choosing the one with the largest energy gain. Although only swaps with positive energy gains are allowed, the evaluation of all combinatorial possibilities renders this approach computationally too expensive. One way to speed up combinatorial optimisation is the iterated local search (ILS) which is a greedy variant of the

KL algorithm where a permutation is executed as soon as we find the first swap that lowers the energy [138]. Additionally one can choose the next swap by estimation using only the knowledge of energy differences for changes of single particle identities (flip gains). This reduced the computational cost since only N flip gains have to be calculated instead of $N_A \times N_B$ swap gain energies. The swap particles are then chosen from the two lowest flip gains or in a more approximate way. In our calculations we are using the ILS scheme where the next swap is determined by the lowest flip gain estimated from a sequence of approximate flip gains calculated before the geometry relaxation step [106] and where the combinatorial optimisation procedure is stopped as soon as a swap that doesn't lower the energy is encountered.

In summary, we perform basin-hopping Monte Carlo runs of $3 \cdot 10^5$ accepted steps at the temperature fixed at $T = 0.1$. In the Monte Carlo moves we limit the maximum change of any Cartesian coordinate and impose a tolerance on the binding energy of individual atoms below which an angular step is taken for that atom. If the energy does not decrease within a certain number of steps we reseed the run. The local optimisations or quenches in the coordinate space are done with the L-BFGS algorithm where the maximum number of iterations allowed is $2 \cdot 10^3$ for the 'sloppy' quenches of the basin-hopping run and $2 \cdot 10^6$ for the final quenches that are used to produce the output. The convergence criterion for the root mean square (RMS) force in the basin-hopping quenches was set to $5 \cdot 10^{-4}$. Quench minima are only considered to be different if their energies differ by at least 10^{-5}. The tolerance for the RMS force in the final set of quenches that are used to produce the output is 10^{-7}. We calculate the energy of the binary Lennard-Jones clusters without using a distance cutoff. The system is translated so that the centre-of-mass lies at the origin after every quench. We use the container that prevents particles evaporating during quenches. Algorithm also performs homotop refinement for a binary system using the ILS scheme. The refinement happens every basin-hopping step, after the coordinates have been perturbed and quenched. It involves exchanging the coordinates of two unlike atoms until a termination condition is met. All quantities are give in the Lennard-Jones units [61] of σ_{AA} and ϵ_{AA}.

The performance of the algorithm was tested by comparing with the energies and coordinates of the homogeneous and binary minimal energy Lennard-Jones clusters published in The Cambridge Cluster Database [118] as well as in the other sources [119, 139]. We found the agreement to the available precision of the data and continued to use the same algorithm for scanning a larger parameter range.

2.3.3 Classification scheme

To analyse the crystalline structure of clusters we use the Steinhardt bond-orientational order parameters [140] which are based on spherical harmonics and are commonly used to distinguish structures formed during the crystallisation of undercooled or compressed liquids [141].

The method of bond order parameters analyses the symmetries in the orientations of bonds around particles where a bond is defined as a vector connecting a pair of neighbouring particles. The cutoff radius is used to identify neighbouring particles, we set its value to the radius between the first and the second peak of the pair correlation function although its precise value should not affect the values of bond order parameters.

For a bond $\mathbf{r}_{ij}$ between particles i and j the local order parameters are defined as

$$Q_{lm}(\mathbf{r}_{ij}) = Y_{lm}(\theta(\mathbf{r}_{ij}), \phi(\mathbf{r}_{ij})) \ , \tag{2.6}$$

where $Y_{lm}(\theta, \phi)$ are the spherical harmonics while $\theta(\mathbf{r}_{ij})$ and $\phi(\mathbf{r}_{ij})$ are the polar and azimuthal angles of the bond $\mathbf{r}_{ij}$ with respect to any arbitrary and fixed reference frame. Only bond parameters Q_{lm} with even l are of interest because they are centrally symmetric and therefore invariant to bond inversions between particles i and j, i.e. their value does not change if a bond is depicted by $\mathbf{r}_{ij}$ or $\mathbf{r}_{ji} = -\mathbf{r}_{ij}$. To characterise the overall symmetry of a cluster we calculate the global bond order parameter $\overline{Q}_{lm}$ by summing over all nearest neighbour bonds between the particles in a cluster

$$\overline{Q}_{lm} = \frac{1}{N_b} \sum_{\text{bonds}} Q_{lm}(\mathbf{r}_{ij}) \ , \tag{2.7}$$

where N_b denotes the number of bonds. To make the order parameters invariant with respect to the rotations of the coordinate system Steinhardt introduced two additional rotationally invariant combinations of $\overline{Q}_{lm}$, the second order invariants

$$q_l = \sqrt{\frac{4\pi}{2l+1} \sum_{m=-l}^{l} |\overline{Q}_{lm}|^2} \tag{2.8}$$

and the normalised third-order invariants

$$w_l(i) = \frac{\sum\limits_{m_1+m_2+m_3=0} \begin{pmatrix} l & l & l \\ m_1 & m_2 & m_3 \end{pmatrix} \overline{Q}_{lm_1} \overline{Q}_{lm_2} \overline{Q}_{lm_3}}{\left(\sum\limits_{m=-l}^{l} |\overline{Q}_{lm}|^2 \right)^{3/2}} \ . \tag{2.9}$$

The integers m_1, m_2 and m_3 run from $-l$ to l while only the combinations with $m_1 + m_2 + m_3 = 0$ are allowed and the term in brackets is the Wigner 3-j symbol [142].

A set of bond order parameters holds the information on the crystalline structure and can be used to identify different crystal symmetries, depending on the choice of l. In practice, the four parameters q_4, q_6, w_4 and w_6 are often sufficient to distinguish between crystal structures, when compared to the values of the ideal periodic lattices although at higher temperatures their distributions can get smeared out due to thermal fluctuations. In our case the resulting

	q_4	q_6	w_4	w_6
FCC	0.19094	0.57452	−0.15932	−0.01316
HCP	0.09722	0.48476	0.13410	−0.01244
SC	0.76376	0.35355	0.15932	0.01316
BCC	0.08202	0.50083	0.15932	0.01316
liquid	0	0	0	0
Ih bulk	0	0.19961	−0.15932	−0.16975
Ih surface	0	0.20729	0.15932	0.16975

Table 2.1: Bond-orientational order parameters with $l = 4$ and $l = 6$ for ideal periodic lattices with face-centred-cubic (FCC), hexagonal close-packed (HCP), simple cubic (SC), body-centred-cubic (BCC) symmetries, bulk and surface values for complete Mackay icosahedra (Ih) and a disordered liquid [143].

four values attached to each cluster were compared to the values of four ideal lattices (SC, BCC, FCC, HCP), to a liquid configuration and to values of complete Mackay icosahedra [143]. The clusters were classified according to the closest matching of their bond parameters to the reference values shown in Table 2.1.

2.4 Binary clusters of nanoparticles with heterogeneous attractions

To facilitate the exploration of possible outcomes in the self-assembly experiments inside emulsion droplets with heterogeneous mixtures of nanoparticles we employ a simplifying model where we represent nanocrystals close to the ordering transition as spherical particles interacting through generic isotropic coarse-grained potentials. Our model describes the self-assembly of a mixture of two different types of spherical particles (A and B) whose attractions differ by a given ratio. Spheres of identical diameter interact via a Lennard-Jones potential as described by Equation (2.1) where the total energy of a cluster of spheres is obtained by summing the contributions from all pairs of particles. In the following, we use ϵ_{AA} as unit of energy and σ_{AA} as unit of length. The free parameters are ϵ_{BB}, σ_{BB}, ϵ_{AB}, σ_{AB}, while N and N_B determine the composition of a cluster.

Particles in the cluster are of the same diameter but have different interaction strengths. We choose different ratios of the interaction constants to describe material combinations of different dissimilarities, $\epsilon_{BB}/\epsilon_{AA} = 0.90, 0.50$ and 0.01. These values correspond to the ratios of dispersion interactions of gold nanoparticles with those of less strongly interacting materials like silver, copper and polymers, respectively, across a hexane medium [144]. The remaining parameter, ϵ_{AB} was calculated as a geometric mean approximation, $\epsilon_{AB} = (\epsilon_{AA}\epsilon_{BB})^{1/2}$. This

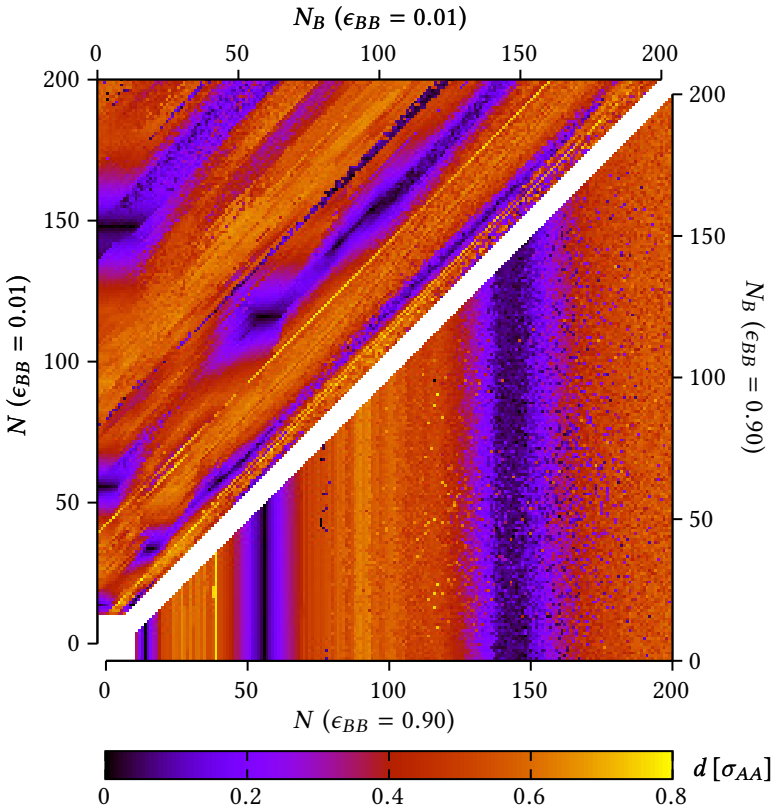

Figure 2.4: Distance of the innermost particle from the centre of mass of the cluster as a function of cluster composition and size for two different material combinations.

is also known as the Berthelot combining rule [145], a widely used choice for describing the dispersion interactions between two dissimilar materials which describes well the properties in simple mixtures of Lennard-Jones fluids [146]. To explore the effect of the combining rule we additionally studied three different values for the inter-species interaction strength at a fixed ϵ_{BB}.

Although we set the parameters to model specific combinations of materials, the results we present are rather general. We tested the stability of several structures against the variation of the interaction parameters and found them to be stable over a relatively large range (see Figure 2.9). Thus e.g. a mixture of metallic and polymeric nanoparticles, as they are commonly used in experiments on colloidal suspensions, would yield the same structures for many different choices of metal.

We analysed the structure diagram as a function of the cluster size and composition, i.e. of the number of all particles N and the number of B particles N_B. In contrast to the work of Doye [119] we are not interested in the compositional global minima where the numbers of different particles in the cluster are subject to optimisation, but in the lowest minima at given compositions. We thus aim to determine the structural behaviour that is to be expected for mixtures of spheres with dissimilar attractions in e.g. confined agglomeration experiments with bimetallic nanoparticles where the composition inside confinement is well defined.

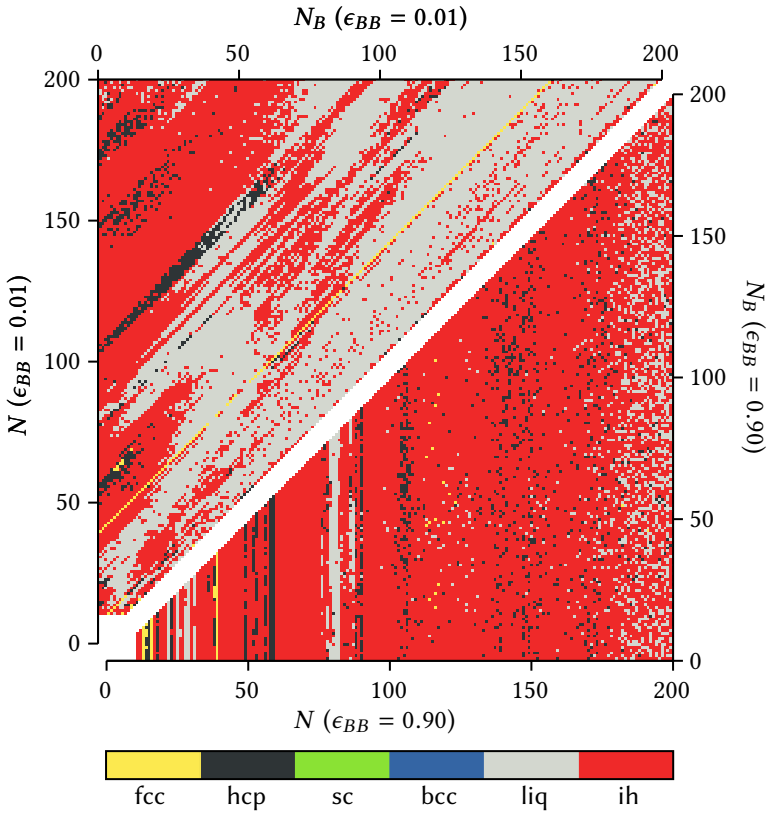

Figure 2.5: Classification of clusters with different sizes and compositions according to the bond-orientational order parameters q_4, q_6, w_4 and w_6 averaged over all the particles in the cluster for two different material combinations.

In Figures 2.4, 2.5 and 2.7 we present diagrams of several observables that characterise the structure of the putative minimal energy clusters for two different material dissimilarities. Data for i.e. $\epsilon_{BB} = 0.90$, $\epsilon_{AB} = 0.95$ is shown in the lower triangle and $\epsilon_{BB} = 0.01$, $\epsilon_{AB} = 0.10$ in the upper triangle. Every single speck in the diagram corresponds to one basin-hopping calculation of the global energy minimum. For all cluster sizes N and compositions N_B we find a core-shell separated structure with B particles on the outside. This is expected as the A particles attract each other more strongly than the B particles and are therefore not placed on the boundary where the number of neighbours is smaller. Clusters with directional symmetries can thus only occur for large number ratios between A and B particles, where the A particles form a core that is covered by a suitable, smaller number of less strongly bound B particles which are distributed in a structure that optimises their energetic interactions. We also present additional observables and parameter choices for varying mixing attractions of different particle species in a database that contains more than 180,000 minimal energy configurations of the resulting clusters which can be visualised and downloaded using our web application [147].

Figure 2.4 shows the minimal distance of any particle in the cluster from the geometric centre of the cluster, $d_{\min} = \min \|\boldsymbol{r}_i - \boldsymbol{r}_c\|$. At certain numbers, there are clusters with one

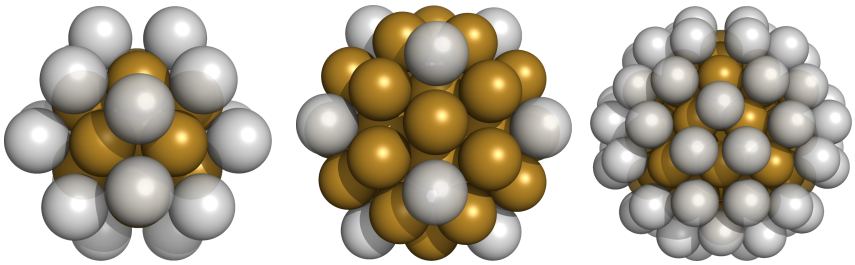

Figure 2.6: Three examples of orientationally symmetric minimal energy clusters of Lennard-Jones particles with the same diameter and with attraction ratio $\epsilon_{BB} = 0.50\epsilon_{AA}$. Left: The ideal icosahedron of A particles in the core is surrounded by 20 B particles at the centres of its triangular surfaces in the minimal energy solution for $N = 33$ and $N_B = 20$. Middle: The ideal icosahedron with valency 12 is a minimal energy solution for $N = 55$ and $N_B = 12$. Right: Minimal energy solution for $N = 115$ and $N_B = 60$ where B nanoparticles are arranged in 20 triangles lying on top of triangular faces of the central Mackay icosahedron.

particle in the centre (dark spots), a feature that is characteristic for Mackay icosahedra and thus enables us to identify them. We can clearly see this feature around the clusters with sizes 13, 55 and 147. These numbers, also sometimes called the magic numbers, are the numbers of particles in the first three complete Mackay icosahedra. In general, the number of particles in a Mackay icosahedron with L complete layers around the central particle is $N = \frac{10}{3}L^3 + 5L^2 + \frac{11}{3}L + 1$ [148]. The diagram shows that for large ϵ_{BB} the Mackay structure is nearly independent of composition (vertical dark stripes) while for small ϵ_{BB} it is stable for constant N_A (diagonal dark stripes). In addition, there are some other isolated regions in the structure diagram with a central particle. Here, typically an ideal icosahedral core is covered with a shell of particles of the other species. These structures are particularly interesting as they offer valence with specific symmetries as can be seen in example snapshots in Figure 2.6. The particles on the corners could be functionalised to produce building blocks of colloidal molecules.

We analyse the crystalline structure in terms of Steinhardt bond-orientational order parameters q_4, q_6, w_4 and w_6 [140]. By comparing their values averaged over all the particles in the cluster to the values obtained for several known crystals and complete icosahedra we classify clusters according to the closest matching and observe that icosahedral features largely prevail [143], which is also confirmed by visually inspecting the resulting clusters. An interesting feature are the vertical stripes in the lower triangle of Figure 2.5 which imply structural features that are independent of composition, i.e. close packing in space is more important than the optimisation of energetic bonds.

In Figure 2.7 we show the dipole moments of the clusters, where we assigned charge +1 to particles of type A and charge −1 to particles of type B. The values are mostly close to zero, but there are also certain regions with larger dipole moments. A large dipole moment corresponds to Janus-like phase separation. While we do not observe large dipole moments due to core shell structure, there are some regions with non-zero dipole moments where the A particles

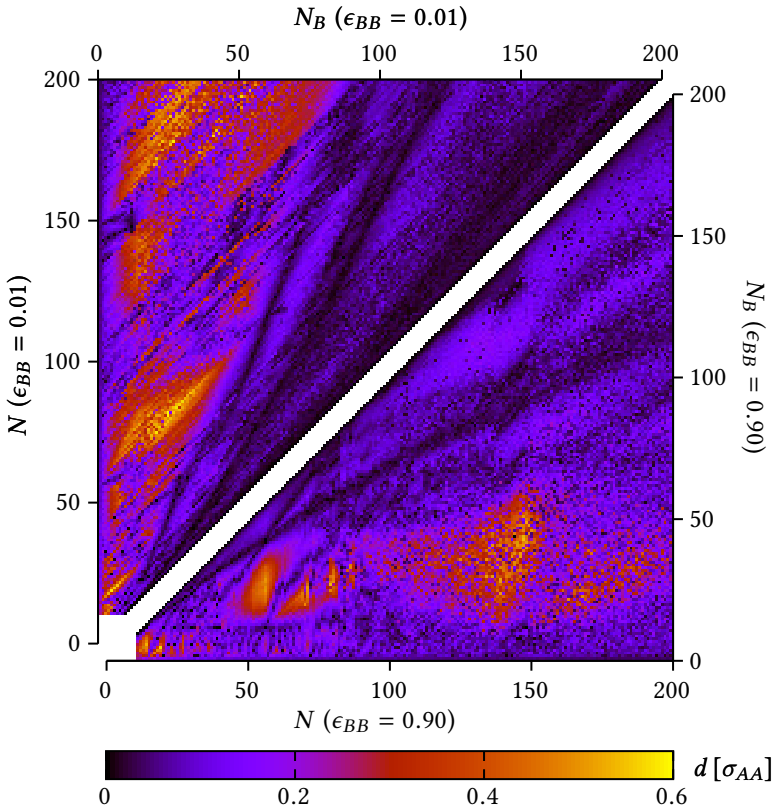

Figure 2.7: Magnitude of the dipole moment normalised to the number of particles as a function of cluster composition and size for two different material combinations. When computing the dipole moment we assigned charge +1 to particles of type A and charge −1 to particles of type B.

occupy one side of the outer shell. (See e.g. figure 2.9 middle row right column.) Clusters with a large dipole moment that are internally phase separated are observed for mixtures of two dissimilar and less compatible particle types as presented in Figures 2.15 and 2.16. Such a model describes the case of disfavoured mixing, for example when two less cross compatible ligands are attached to different nanoparticle types.

2.5 Additional parameters and observables

Additional minimal energy structures of binary Lennard-Jones clusters were calculated for multiple combinations of van der Waals attractions between B species and between A and B species of particles. A summary of model parameters used in these studies is shown in Table 2.2. In the first three models the ratio of the intra-species attraction parameter ϵ_{BB} is varied to describe materials with various degrees of dissimilarity while the inter-species attraction parameter, i.e. the mixing parameter ϵ_{AB}, was calculated according to the Berthelot combining rule which is commonly used to approximate cross interactions in simple binary mixtures.

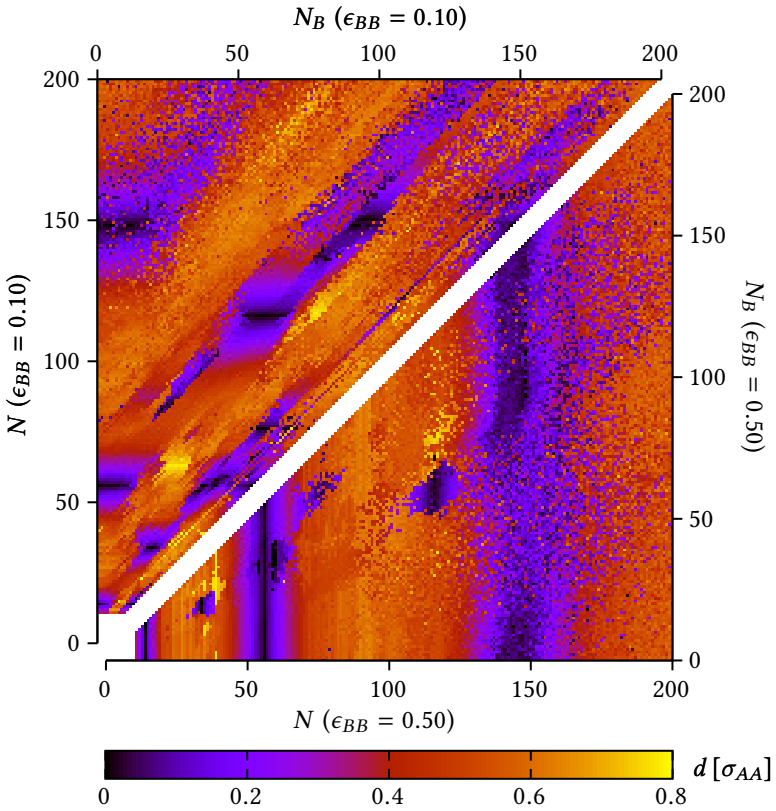

Figure 2.8: Distance of the innermost particle from the centre of mass of the cluster as a function of cluster composition and size for two different material combinations with $\epsilon = 0.10$ and $\epsilon = 0.50$.

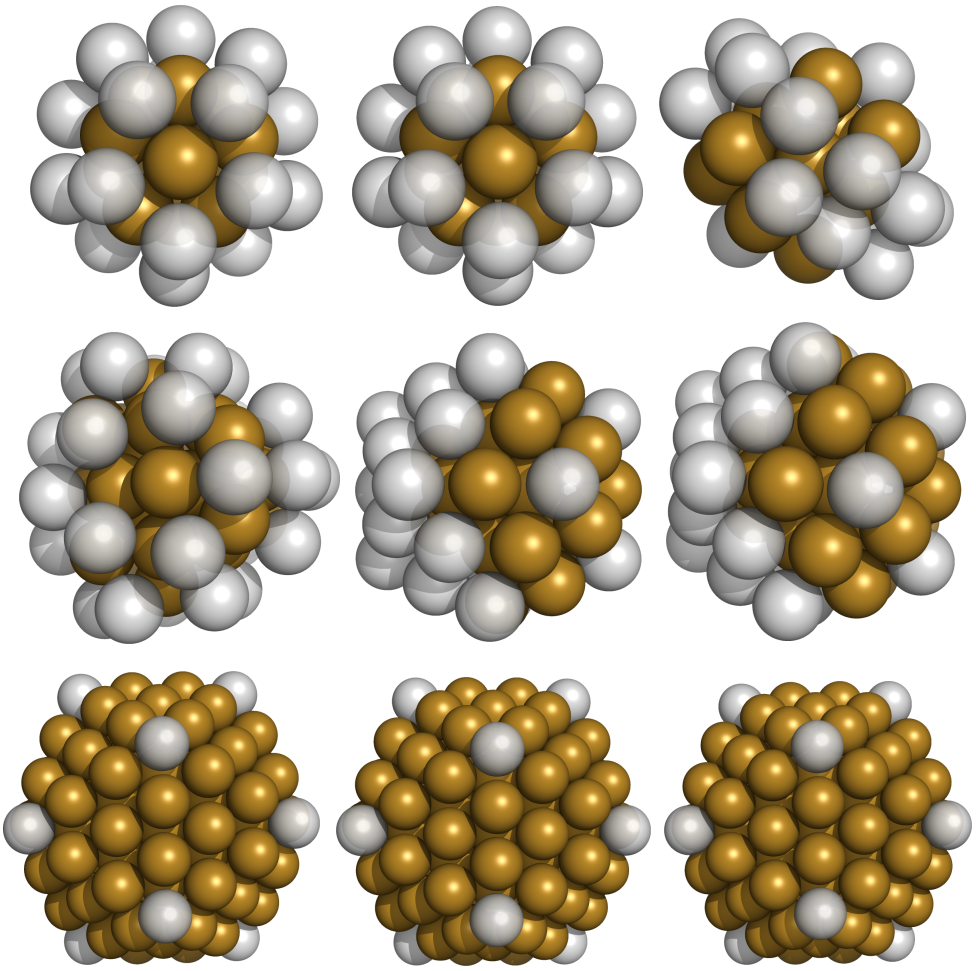

Figure 2.9: Examples of symmetric clusters that show little or no sensitivity to changing the relative attraction strength ϵ_{BB} of species B particles. From left to right: $\epsilon_{BB} = 0.01,\ 0.5,\ 0.9$. From top to bottom: $N = 33,\ 55,\ 147$ and $N_B = 20,\ 28,\ 12$.

	ϵ_{AA}	ϵ_{BB}	ϵ_{AB}	σ_{AA}	σ_{BB}	σ_{AB}
model 1	1	0.01	0.10	1	1	1
model 2	1	0.50	0.71	1	1	1
model 3	1	0.90	0.95	1	1	1
model 4	1	0.62	0.31	1	1	1
model 5	1	0.62	0.62	1	1	1
model 6	1	0.62	0.79	1	1	1

Table 2.2: Parameters used in the study of different models of the binary Lennard-Jones mixture of spherical particles with equal diameters (σ). Models 1 to 3 describe binary mixtures with different attraction dissimilarities where the inter-species attractions are approximated by a geometric mean (Berthelot rule) while models 4 to 6 describe mixtures with the same attraction dissimilarity but different levels of inter-species attraction.

In model 2 type B particles are two times less attractive than type A particles, which presents a less extreme choice of attraction ratios than the already discussed cases of $\epsilon_{BB} = 0.01$ and $\epsilon_{BB} = 0.90$ from models 1 and 3. To explore the effect of the choice of the mixing attraction on the structure of clusters different values of the mixing parameter were used in the last three models, i.e. $\epsilon_{AB} = \epsilon_{BB}/2$ (model 4), $\epsilon_{AB} = \epsilon_{BB}$ (model 5) and a geometric mean (model 6). Model 4 describes the case of disfavoured mixing which is relevant when two less cross-compatible ligands are attached to nanoparticles. This causes the formation of distinct Janus-type phase separated clusters instead of the core-shell structures observed for other models. Such ligand-induced phase-separation has been observed in the fabrication of solid films from dispersions of binary polymer-tethered nanoparticle blends where ligand interactions were modified with distinct types of polymer chains [149].

Diagrams of various observables that characterise the structures of the resulting minimal energy clusters are shown in Figures 2.10, 2.11, 2.12, 2.13 and 2.14. Alongside with the distance of the innermost particle from the centre of mass of the cluster in Figure 2.10, the classification of clusters according to the bond-orientational order parameters q_4, q_6, w_4 and w_6 in Figure 2.11 and the magnitude of the dipole moment in Figure 2.14 we also analyse two additional observables, the bond-orientational order parameter w_4 and the difference Δr_{BA}. The latter is calculated between the average distances of type B and type A particles from the centre of mass of the cluster,

$$\Delta r_{BA} = \left[\frac{1}{N_B} \sum_{i=1}^{N_B} r_i^B - \frac{1}{N_A} \sum_{i=1}^{N_A} r_i^A \right] / \left[\frac{1}{N_A + N_B} \sum_{i=1}^{N_A+N_B} r_i \right], \tag{2.10}$$

and normalised by the average distance of all particles from the centre of mass of the cluster. Here r_i^A and r_i^B are the distances of i-th particle of type A or B from centre of mass of the cluster

whereas N_A and N_B are the numbers of type A and type B particles in the cluster. Examples of the resulting minimal energy binary clusters are shown in Figures 2.15 and 2.16.

From Figure 2.10 we can distinguish the regions with icosahedral features and conclude some general trends. At first, we again see that for very large attraction dissimilarities (model 1) we obtained dark diagonal lines indicating that it is the number of type A particles that determine the structure irrespective of the number of type B particles whose energetic contributions are negligible. For other models we observe the vertical dark lines at magic numbers of complete Mackay icosahedra which indicate that it is the total number of particles in the cluster determining its structure irrespective of the composition ratio.

This trend is, however, not uniform, but gets modified variably for models 2, 4 and 6. In models 2 and 6 isolated regions with icosahedral structure appear outside of magic cluster sizes and correspond to structures with symmetric patterns of type B particles forming as a part or on top of icosahedra of type A particles as shown in Figure 2.6. This is due to the fact that the energetic contributions from type B particles are at certain compositions large enough to disrupt or stabilise icosahedral packing. This tendency to disrupt the otherwise composition independent icosahedral features becomes even stronger for disfavoured mixing of different particle species. As we can see for model 4 the icosahedral features remain at magic cluster sizes only close to homogeneous cluster compositions but otherwise completely disappear. The new isolated icosahedral regions appear that corresponds to clusters composed of two separated homogeneous icosahedra composed of only type A or type B particles sharing a common face with each other as shown by the two examples in Figures 2.15 and 2.16.

Similar information about structural features depending on the number of type A particles (model 1) and on the cluster size (model 2–6) is obtained from the classification of crystal structure of clusters according to bond-orientational order parameters q_4, q_6, w_4 and w_6 shown in Figure 2.11 and the order parameter w_4 shown in Figure 2.12. Additionally we see that in certain regions disordered or HCP overall cluster structures prevail over otherwise predominantly icosahedral features.

The difference Δr_{BA} which is an indication of the core-shell structure of the clusters is shown in Figure 2.13. For models 1–3 and 6 we see that Δr_{BA} is always positive and therefore the structures of all clusters, irrespective of their size and composition, are core-shell with less attractive type B particles lying on the outer shell where they have a smaller number of energetic bonds to their nearest neighbours. In the model 5 where the mixing attractions are the same as the attractions between type B particles the situation changes only in the case of a very small number of type A particles in a cluster when optimal packing of a large number of less attractive type B particles prevails and the type A particles are moved to the outer shell. A contrasting situation is observed for model 4 where Δr_{BA} is zero for clusters of equal composition, $N_A = N_B$, but continuously rises with increasingly assymmetric composition,

either to positive or negative values. This indicates that either type A or type B particles can lie on the shell of the cluster depending on its composition despite the differences in their attractions.

From the magnitude of the dipole moments in Figure 2.14 we see that model 4 results in clusters with large dipole moments that are completely phase separated as a consequence of their small mixing attractions. Here, the minimisation of energy favours structures with a large number of contacts between particles of the same type and a a small interface between different particle types. This mostly results in two clusters with icosahedral features, each composed of either type A or type B particles, that are connected by a common face with a low energy contribution. Two examples of such phase separated clusters are shown in Figures 2.15 and 2.16. For symmetric compositions, $N_A = N_B$, the corresponding phase separated clusters are ideally balanced on each side of the cluster's centre of mass and are characterized by Δr_{BA} close to zero. Many clusters with larger dipole moments are observed also in model 5 where particles often form core-shell clusters with asymmetric shells. In models 1–3 and 6 the inter-species attractions are large enough to promote mixing of type A and type B particles in icosahedral clusters which causes small dipole moments except in multiple isolated regions where they can become considerably larger. These larger dipole moments are produced from an asymmetric distribution of less attractive particles on the outer shell of otherwise icosahedral clusters which seems to be a consequence of particular packing optimisations at specific cluster sizes and compositions.

2.6 Conclusions

Fabrication of advanced materials and devices through the 'bottom-up' approach requires inorganic nanocrystals with specific morphologies which can then further self-assemble into hierarchical structures [56]. Numerous such assemblies were produced from organically stabilised metallic nanoparticles that provided useful properties in the fields of catalysis, optics, electronics and rheology [93]. For example, mixing of polymers and nanoparticles with tailored sizes and coatings has enabled regulated spatial distribution of nanoparticles in the polymer matrix and construction of hierarchically structured flexible composites with advantageous mechanical properties such as self-healing and self-corralling [150]. Nanocrystals with patchy interactions, Janus character or core-shell structure have been broadly applied and shown to form superlattices with desirable properties such as an optical bandgap [151] or synthetic bilayers and rings for drug-delivery [152].

In the presented work we focused on the structures of nanocrystals that can be formed in isolated, energy-driven assembly protocols from binary mixtures of spherical particles with dissimilar attractions. Using the basin-hopping global minimisation technique with an ad-

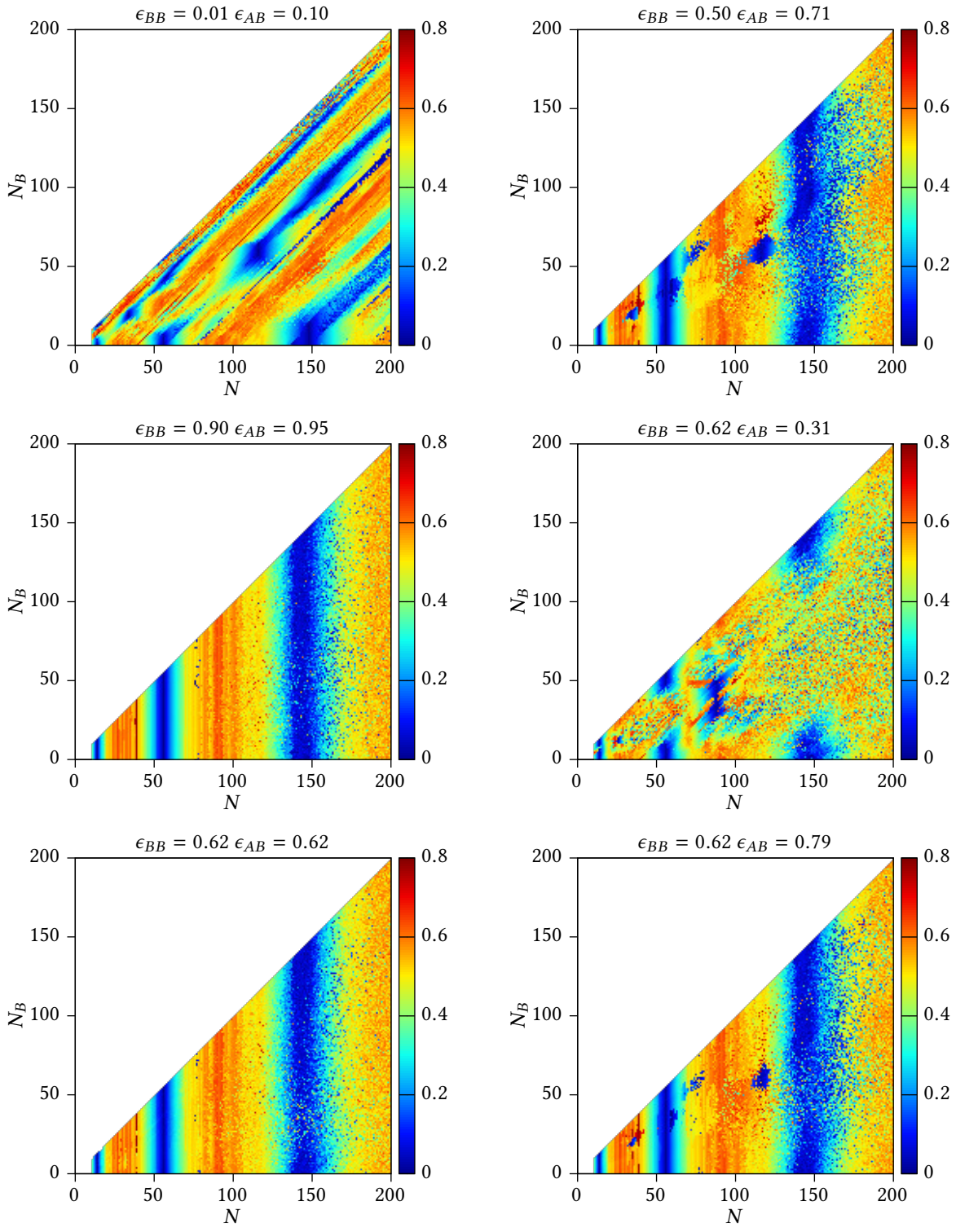

Figure 2.10: Distance (in units of σ_{AA}) of the innermost particle from the centre of mass of the cluster as a function of cluster composition and size.

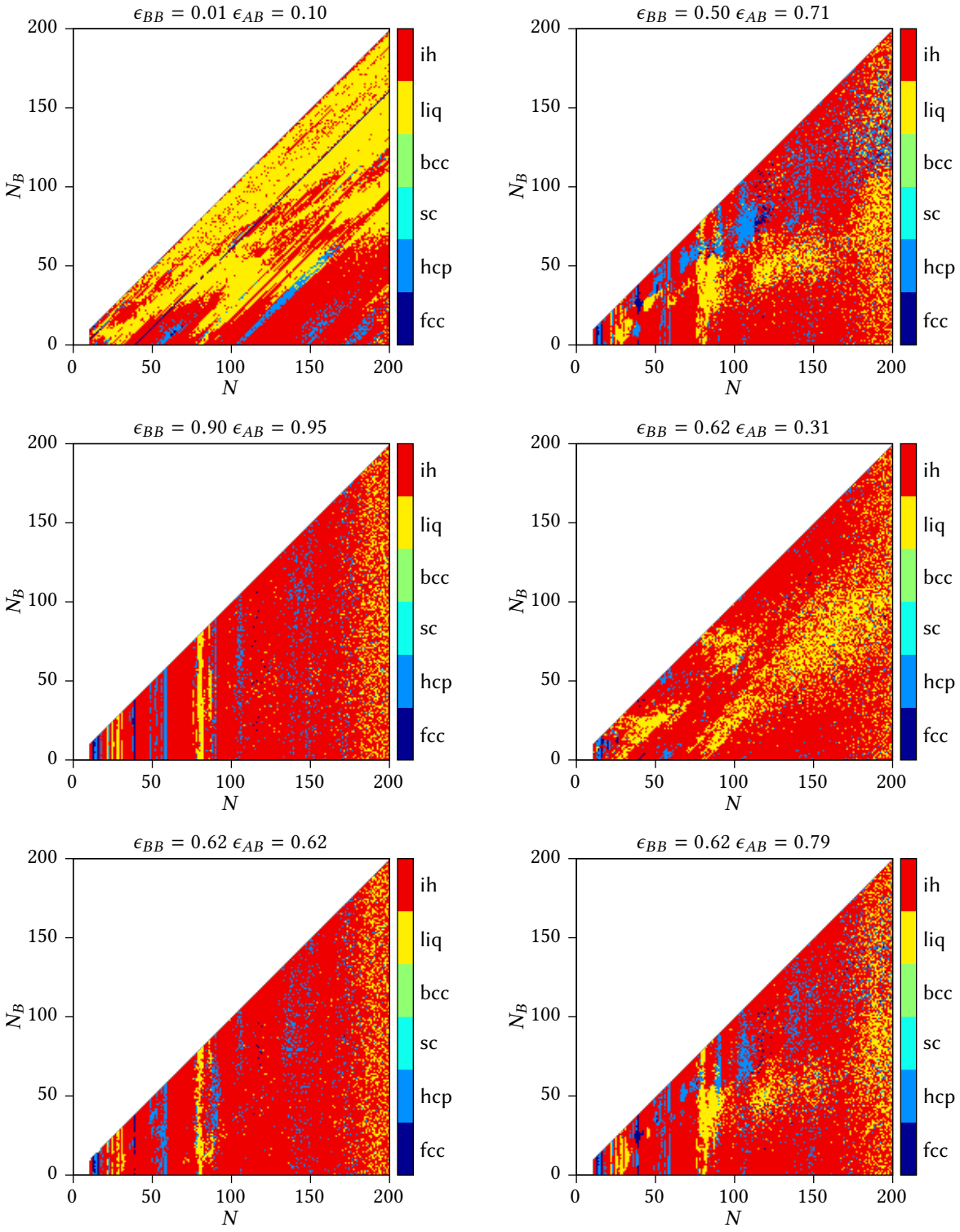

Figure 2.11: Classification of clusters with different sizes and compositions according to the bond-orientational order parameters q_4, q_6, w_4 and w_6 averaged over all the particles in the cluster.

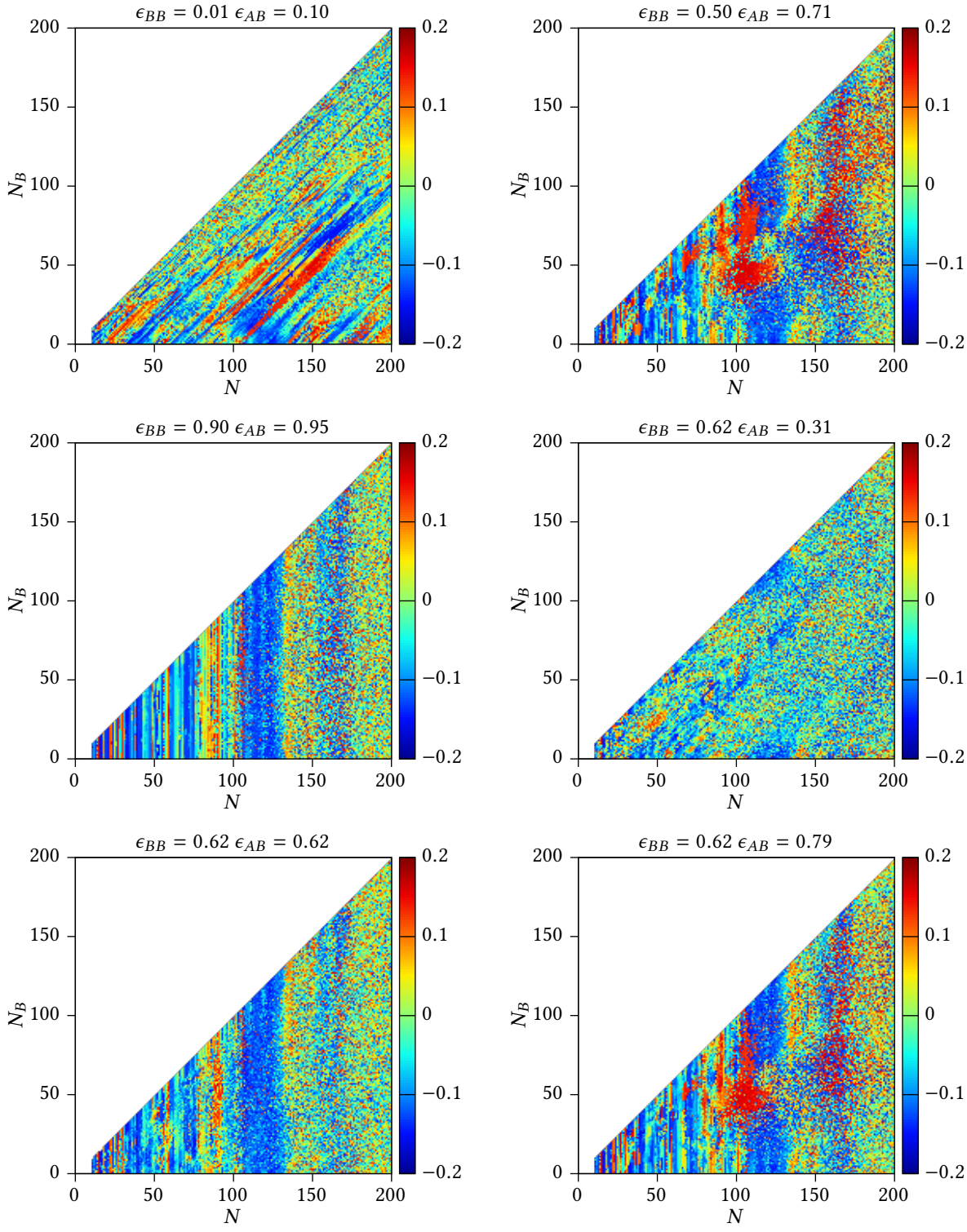

Figure 2.12: Bond-orientational order parameter w_4 as a function of cluster composition and size.

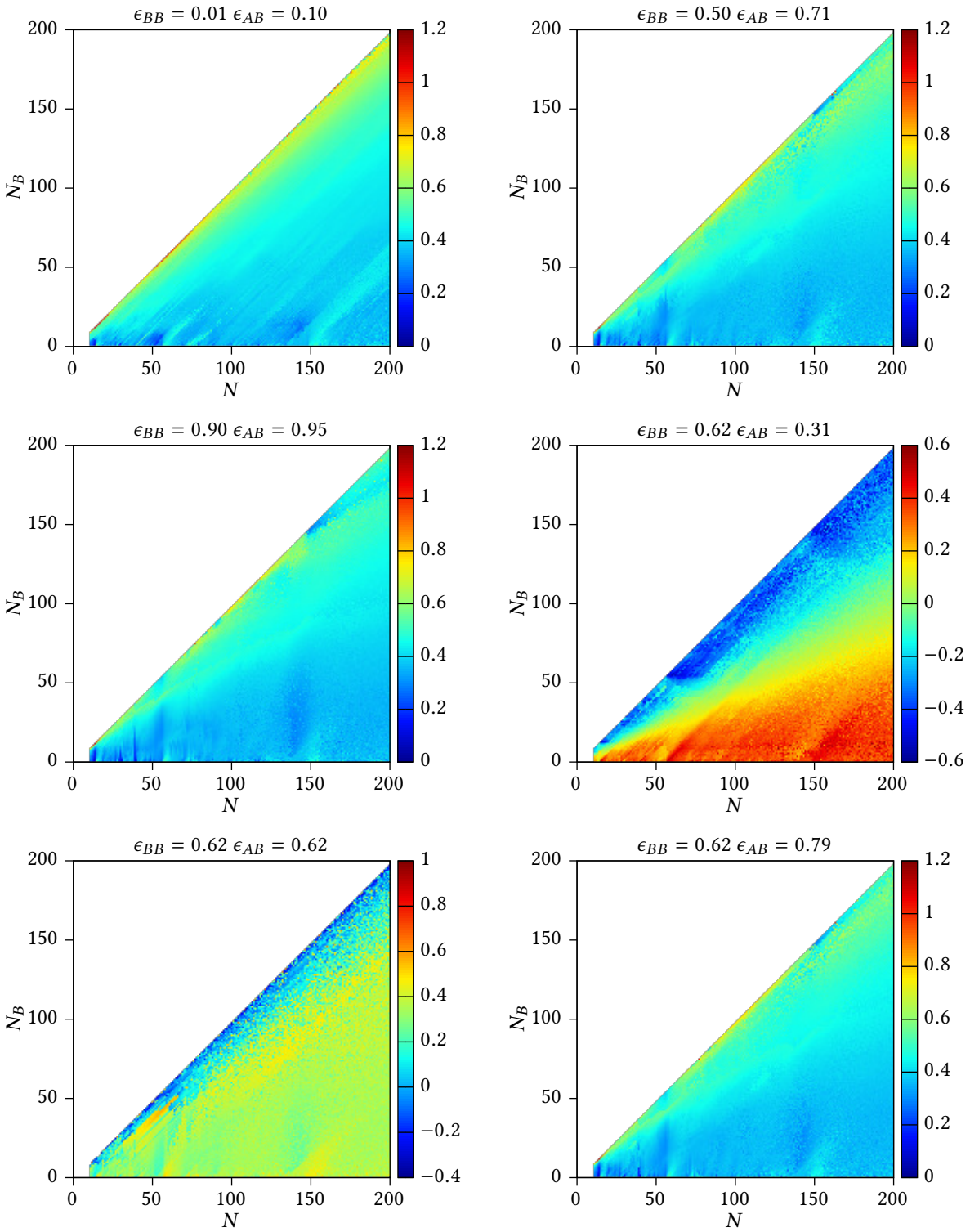

Figure 2.13: Difference between the average distances of type B and type A particles from the centre of mass of the cluster as a function of cluster composition and size.

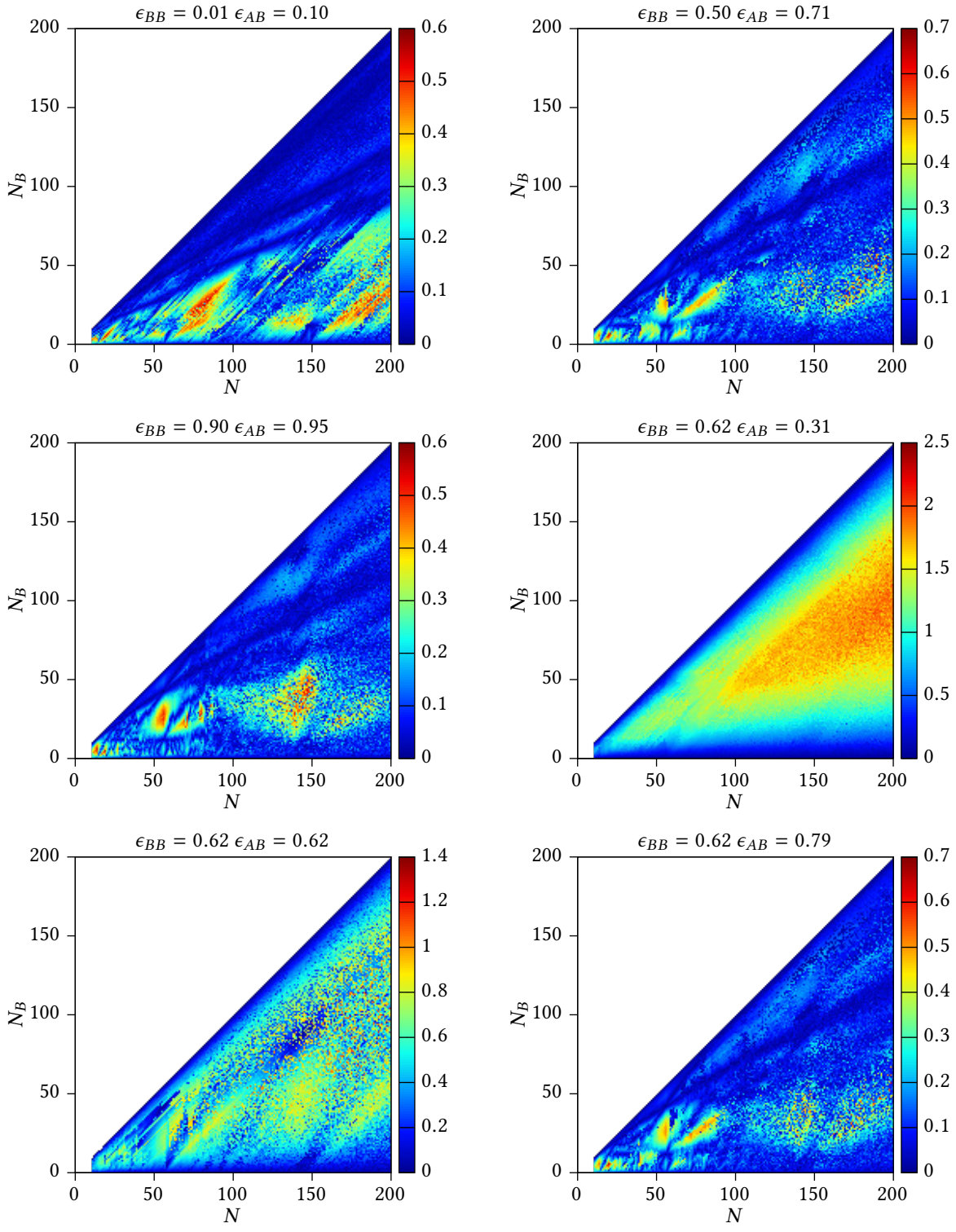

Figure 2.14: Magnitude of the dipole moment normalised to the number of particles as a function of cluster composition and size. When computing the dipole moment we assigned charge +1 to particles of type A and charge −1 to particles of type B.

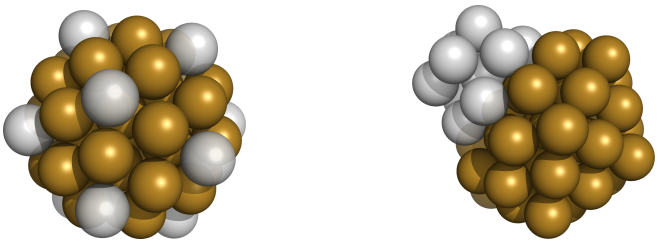

Figure 2.15: The ideal icosahedron with valency 12 is a minimal energy solution for model 6 for $N = 55$ and $N_B = 12$ (left). The corresponding minimal energy solution for model 4 shows a complete separation of both particle types (right).

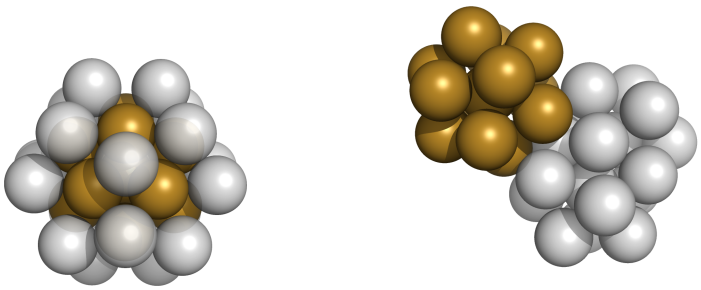

Figure 2.16: The ideal icosahedron in the core is surrounded by 20 particles of B type at the centres of its 20 triangles in the minimal energy solution for model 6 for $N = 33$ and $N_B = 20$ (left). The corresponding minimal energy solution for model 4 shows a full separation of both particle types where particles of A type form a complete icosahedron (right).

ditional hypersurface transformation in the identity space we have computed the putative minimal energy configurations of the binary Lennard-Jones clusters of up to 200 particles. Our model describes binary clusters that are expected to form in the self-assembly protocols driven by energetic interactions such as in the agglomeration of binary mixtures of spherical nanoparticle with the same diameters but different attractions at low temperatures. The interaction parameters were set to mimic a combination of gold, silver and polymeric nanoparticles in hexane, but the main results hold more generally for mixtures of particles with different van der Waals interactions and varying inter-species mixing propensities.

We predict, in particular, which cluster sizes and compositions lead to the core-shell clusters, Janus clusters and clusters with icosahedral symmetry in which the minority species is located at the vertices. To build such structures an assembly protocol is required that can produce clusters through a process dominated by energy minimisation. Even small differences in attraction would then lead to structured clusters with interesting symmetries. If functionalised suitably, these clusters could be promising building blocks for colloidal molecules and crystals. For example, they could be used as patchy particles with site-specific attractions on particle surfaces [153, 154] which are desired in colloidal self-assembly targeting compact crystalline structures, such as the diamond crystalline lattice, that have a bandgap in visible region and are promising for photonic applications [151].

Chapter 3

Pressure-controlled formation of AB_{13}, Janus, and core-shell supraparticles

In this chapter we consider a different extension of the process of nanoparticle agglomeration inside emulsion droplets to a situation where a mixture of nanoparticles of two different sizes is used. Experiments have confirmed that a binary mixture of gold nanoparticles with diameters 4 nm and 8 nm confined in slowly shrinking spheres can form regular supraparticles. Unexpectedly, supraparticles with different structures were observed to self-assemble from the same dispersion of nanoparticles. Binary crystalline superlattices, Janus and core-shell supraparticles were produced when the emulsion of water and oil was made using different surfactants that set different Laplace pressure differences inside emulsion droplets. The same effect was obtained also by moderate changes in the atmospheric pressure on the order of 100 kPa. We present an interpretation of this behaviour by proposing a formation mechanism where pressure changes the inter-particle potentials and determines the self-assembly direction of the confined particle mixture. Molecular dynamics simulations are used to study a decreased solubility model which confirms the formation mechanism. Experimental measurements of optical spectrometry, small-angle X-ray scattering and electron microscopy are compared to simulations and demonstrate that agglomeration concentration indeed depends on the pressure and the size of particles.

3.1 Introduction

Confinement of uniform mixtures of nanoparticles can produce regular superlattices where the restrained particles arrange at liquid-liquid interfaces [155], liquid-air interfaces [156] or inside droplets [26]. Formation of such superlattices is attributed to the entropy maximisation by optimising particle space-filling and to the minimisation of the inter-particle potentials. The relative importance of each of them depends on several factors that influence the system among which the most dominant are as particles core, ligand shell, solvent and the parameters of the self-assembly process. When confining binary dispersions of nanoparticles the parameter space becomes even larger and leads to a remarkable diversity of the observed superlattice structures in these seemingly simple systems [156, 157].

Studies of the confined mixtures of nanoparticles are most intense for a system of particle films which are especially interesting for the applications in devices with semiconductor layers [53, 158]. On the other hand, confinement in droplets has been less highlighted although it has been demonstrated that highly regular clusters or supraparticles can be formed in emulsion droplets [26, 81, 159] or by drying droplets on superamphiphobic surfaces [159]. In fact, heterogeneous mixtures of nanoparticles have not yet been assembled inside emulsion droplets.

Here we study structures of binary supraparticles that can form by confining nanoparticles of different sizes inside shrinking droplets as a result of the evaporation of oil from the oil-in-water emulsions. The same mixture of nanoparticles leads to the formation of different structures, as can be seen in Figure 3.1, which are intriguing for further applications. For example, the resulting crystalline superlattices with AB_{13} structure could potentially serve as patchy colloidal particles for self-assembled of soft materials [56]. The phase separated Janus particles [160] can be used to form highly robust Pickering emulsions [161] while metal-oxide particles are used to enhance homogeneous photocatalysis [162].

In contrast to highly dynamic evaporation of particle films the assembly in emulsion droplets is driven by very slow evaporation that creates quasi-equilibrium conditions at increasing particle concentrations. For simulations this means that equilibrium statistical mechanics approaches can be used to approximately describe the situation in such systems while for experiments it enables in situ observation to be performed alongside inspection via spectrometry. Our molecular dynamics simulations indicate that pressure differences inside droplets change inter-particle potentials which affects nucleation and results in different assembly mechanisms leading to distinct supraparticle structures. This is confirmed by experiments using scattering and transmission methods to study the formation pathways of diverse superlattices.

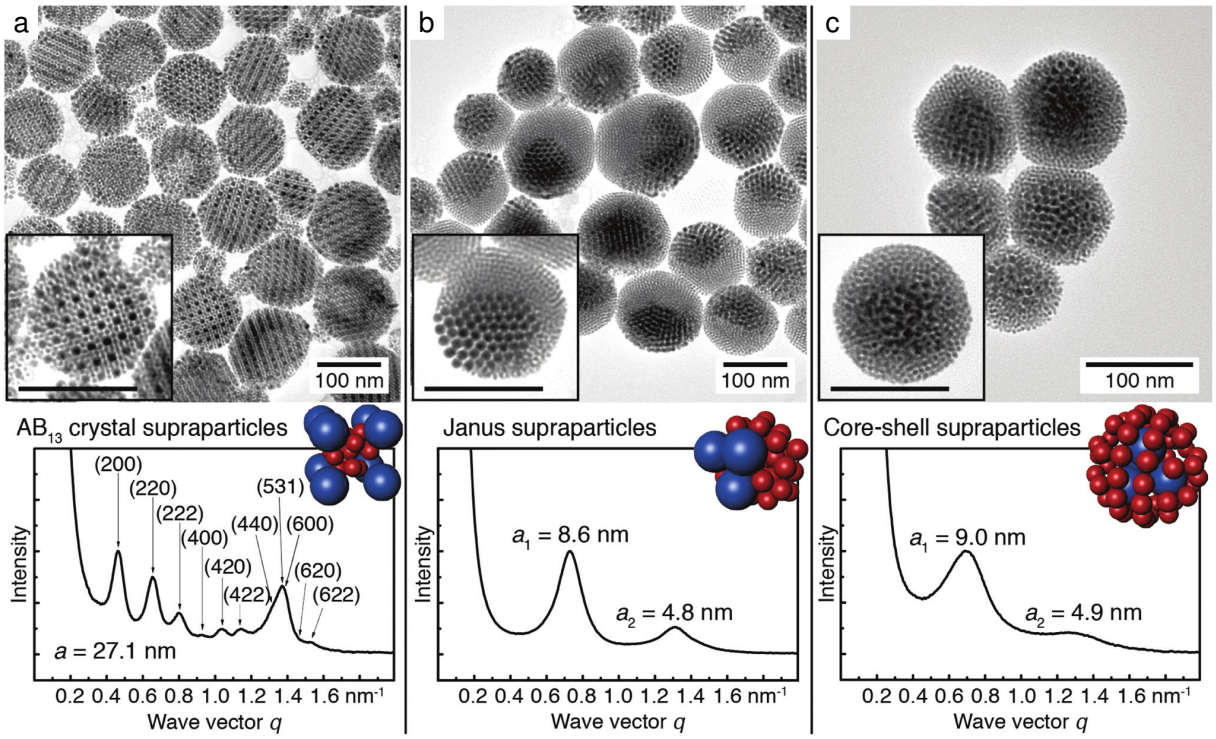

Figure 3.1: Experiments with hexadecanethiol-coated gold nanoparticles of diameters 4 nm and 8 nm in a mixture with the concentration ratio of small and big particles set to 13:1 resulted in supraparticles with radii of around 47 nm. Here the upper row shows micrographs obtained by transmission electron microscopy (TEM) while the lower row shows small-angle X-ray scattering (SAXS) intensities. Three different structures are observed for distinct choices of surfactants used to form a hexane-in-water emulsion. (a) Triton X-100 surfactant produces AB_{13} superlattice which is confirmed by a good matching in the scattering peaks [163]. (b) Triton X-102 and X-165 produce Janus supraparticles where two separate crystalline parts form which can be seen by distinct peaks in scattering intensity. (c) Triton X-705 produces core-shell supraparticles where a dense, disordered shell of small particles surrounds the core of large particles and causes a more broad and shifted peak of small particles in SAXS. [164] - Reproduced by permission of The Royal Society of Chemistry

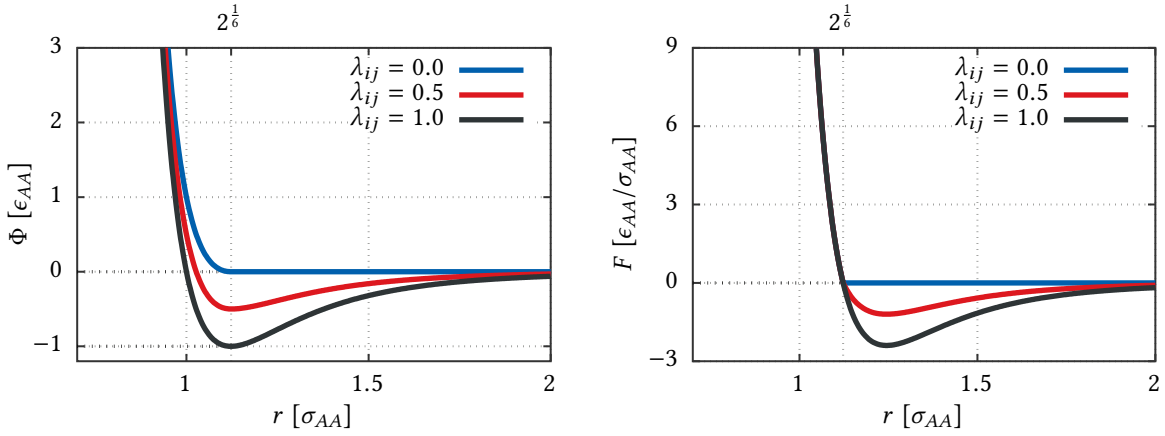

Figure 3.2: The pair potential and the corresponding force magnitudes as used to model the varying solubility in a mixture of spherical particles of two different diameters. Only the potential and force between the big particles are shown here for three different values of the solubility parameter. Larger values of λ_{ij} add more attraction and lead to decreased solubility of particles.

3.2 Methods

3.2.1 Molecular dynamics simulations

To simulate a mixture of nanoparticles confined inside a shrinking spherical container we performed molecular dynamics simulations using LAMMPS [165]. We describe spheres that interact via a purely repulsive but finite force by the Weeks-Chandler-Andersen (WCA) pair potential [166] which is defined as

$$\Phi^{\mathrm{WCA}}(r) = \begin{cases} \Phi^{\mathrm{LJ}}(r) + \epsilon & \text{if } r < 2^{1/6}\sigma \\ 0 & \text{if } r \geq 2^{1/6}\sigma \end{cases} , \tag{3.1}$$

where $\Phi_{\mathrm{LJ}}(r)$ is the standard Lennard-Jones potential defined in Equation (1.3). To model the decreased solubility of specific particle species we include attractions together with the repulsive cores of the particles by adding the Lennard-Jones potential. The total potential between particle types i and j ($i, j \in \{A, B\}$) is calculated as a linear combination

$$\Phi_{ij}(r, \lambda_{ij}) = (1 - \lambda_{ij})\Phi_{ij}^{\mathrm{WCA}}(r) + \lambda_{ij}\Phi_{ij}^{\mathrm{LJ}}(r) , \tag{3.2}$$

where the parameters λ_{ij} increase the attraction between the particles and interpolate between WCA ($\lambda_{ij} = 0$) and LJ ($\lambda_{ij} = 1$) potentials. This form enables us to always have the same repulsive part of the combined potential regardless of the solubility parameters λ_{ij} that change the only the attractive tails. The potential with the corresponding force are shown for three different parameters in Figure 3.2.

We study an additive binary mixture of nanoparticles, $\sigma_{AB} = (\sigma_{AA} + \sigma_{BB})/2$, with the diameter ratio $\sigma_{BB}/\sigma_{AA} = 0.55 - 0.58$ where the icosahedral AB_{13} lattice isostructural with intermetallic phase $NaZn_13$ has been shown to form entropically [163, 167]. The length and energy scales are set by $\sigma_{AA} = 1$ and $\epsilon_{AA} = \epsilon_{BB} = \epsilon_{AB} = 1$. All of these parameters are used both in the WCA and the Lennard-Jones potential. The properties of the mixture are finally specified by choosing the parameters λ_{AA}, λ_{BB} and λ_{AB}.

The mixture is initially prepared in a disordered fluid state with the number ratio of large and small particles fixed to 1:13. Overlaps in the initially random positions of particles are removed by a constant energy run where a limit is imposed on the maximum distance that an atom can travel in one step. The interaction of particles with the wall of the spherical container is also specified by the WCA potential with parameters $\epsilon_{WA} = \epsilon_{WB} = \sigma_{AW} = 1$ while $\sigma_{WB} =$ accounts for the different diameter of the small particles. We found that the details of the interaction with the container wall did not change the results of our simulations, we tried attractive Lennard-Jones potentials and inverse power law potentials with a less steep repulsion.

The confinement by a spherical container is implemented in two different ways. In the first case we simulated the system at a fixed density and in the second we increased the density linearly during the simulation. In all cases we simulated a system at fixed temperature, number of particles and volume (NVT ensemble). The temperature in the system is controlled by adding dynamic variables which are coupled to the particle velocities as defined by the Nose-Hoover thermostat method [69, 69, 168] while the time integration is carried out by a Verlet integration technique [169]. The simulation leading to the AB_{13} crystal needed approximately 3 days to finish at the constant density for 1750 particles while the algorithm was run in parallel on the 12 cores of two Intel Xeon L5640 2,26 GHz CPUs. As nucleation is a rare event for this case it is impossible to simulate the time-dependent confinement where each stage of shrinking would demand the same simulation time on our computing resources. The shrinking confinement is used for simulating core-shell and Janus structures because the relaxation times are much smaller in those cases.

The AB_{13} crystal formed at the temperature $T = 0.6$ and packing fraction $\rho = 0.8$ where the packing fraction is estimated using the effective radius of the particles, $r_{\text{eff}} = 2^{1/6}\sigma/2$. We used stepsize 0.004 and a number of steps up to 10^9 which is usually enough to observe the crystallisation. The crystallisation event is identified by the drop in the potential energy and a decrease in the slope of the average mean square displacement (MSD) of particles as shown in Figure 3.3 for a system with periodic boundary conditions. From the mean displacement it appears that small and big particles crystallise simultaneously while we would expect smaller particles to order first because they have to convey the correlations between larger particles which can not feel the presence of other large particles directly when organised on a cubic

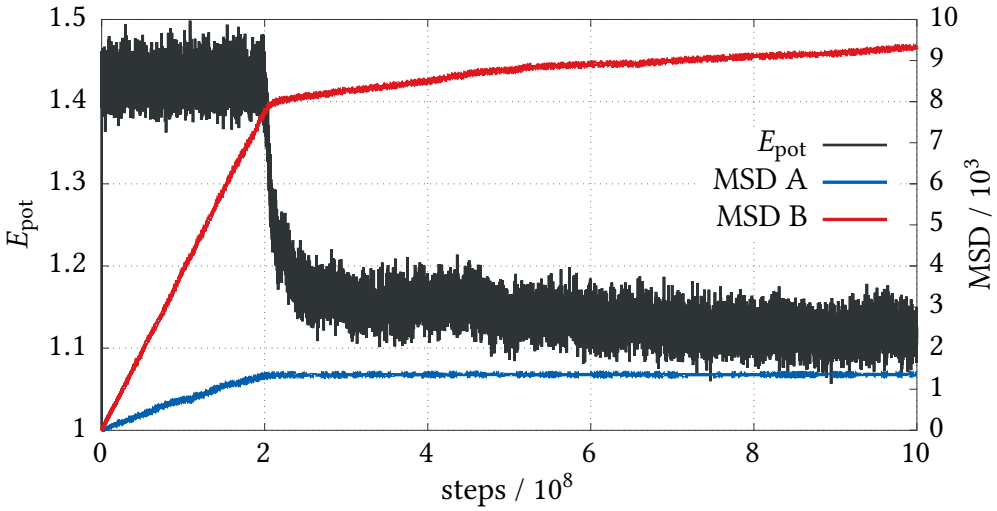

Figure 3.3: Total potential energy and mean squared displacements for particle types A and B as a function of the number of integration steps during a molecular dynamics simulation of 1750 particles in a box with periodic boundaries. Temperature was set to $T = 0.60$, effective packing fraction was $\rho = 0.80$ and timestep was 0.004. All quantities are specified in Lennard-Jones units. The crystallisation to AB_{13} lattice is triggered after $2 \cdot 10^8$ timesteps and is accompanied by a steep decrease in energy while MSD for small and large particles appears to decrease simultaneously.

lattice of AB_{13} structure. We used the same temperature and end density for the simulations using the spherical container where the AB_{13} crystal in the centre is covered by a thin disordered shell of both types of particles as shown in Figure 3.4. The unit cell consists of eight cells with mutually rotated icosahedra one of which is shown in Figure 3.5.

Table 3.1 shows the results for changing structures by adding attractions between particles. The final structure is determined by entropic effects and the interplay of interfacial energies between particle A - particle B boundary, and wall - particle boundaries. Supraparticles with AB_{13}, core-shell and Janus structures are the only final states observed besides the disordered mixture that results for most parameter combinations that lead to mixing.

3.2.2 Small angle scattering calculation

The SAXS scattering intensity is calculated using the Debye's formula approach [170]

$$I(Q) = \sum_i |f_i(Q)|^2 + \sum_{i \neq j} f_i(Q) f_j^*(Q) \frac{\sin Q r_{ij}}{Q r_{ij}} , \tag{3.3}$$

where $f_i(Q)$ are the scattering form factors of the spherical nanoparticles which represent scattering from an isolated sphere and can be computed analytically. The form factor of a

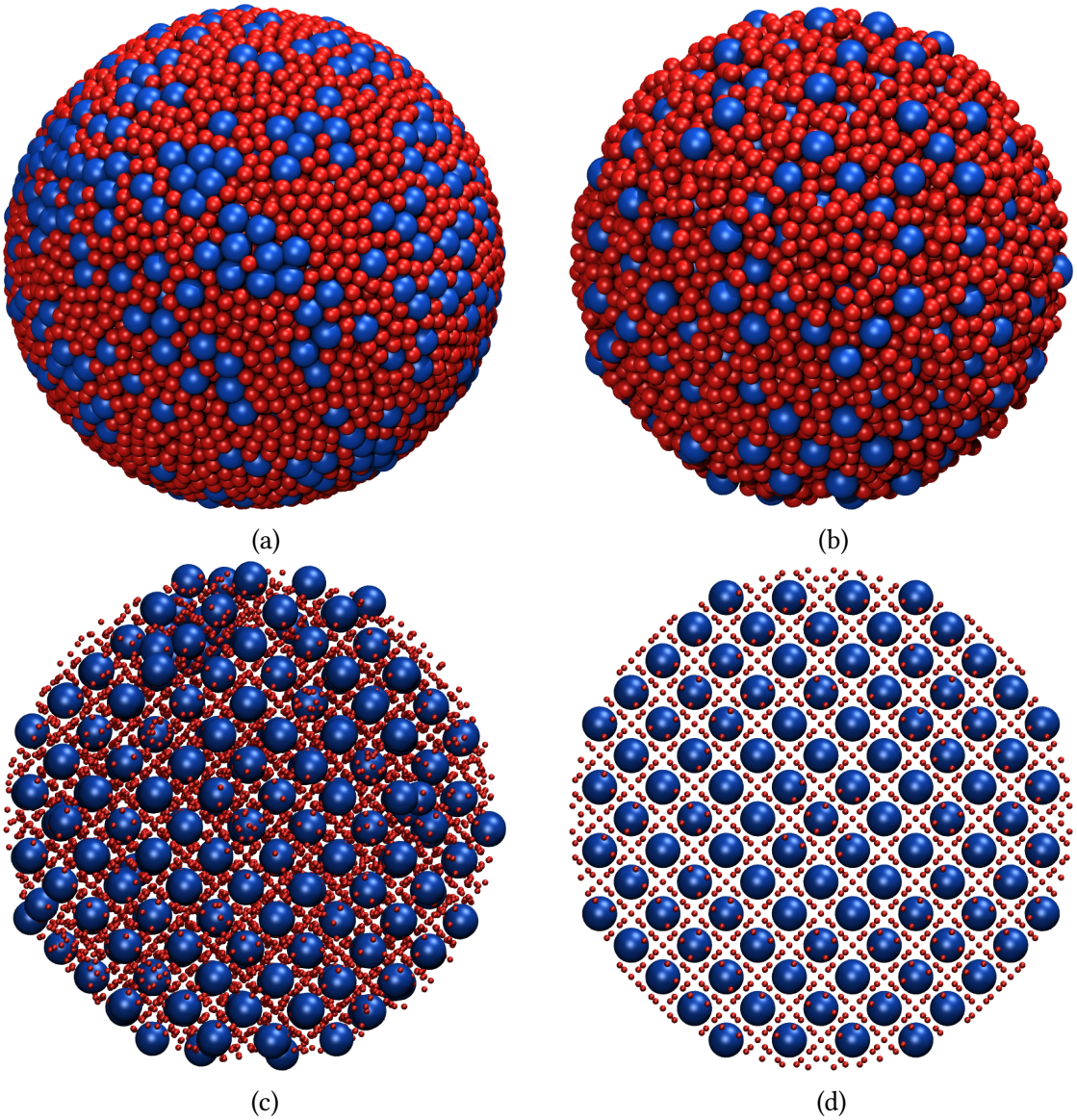

Figure 3.4: Supraparticle with the AB_{13} crystal structure which resulted from the simulation of a binary mixture of 14000 nanoparticles with a size ratio of 0.55 in a fixed spherical container at $T = 0.6$ and $\rho = 0.8$. (a) Complete supraparticle including the disordered shell. (b) The crystalline core of supraparticle without the disordered shell. (c) The size of small particles is decreased for improved visualisation. (d) Model of a supraparticle with AB_{13} crystal structure without defects.

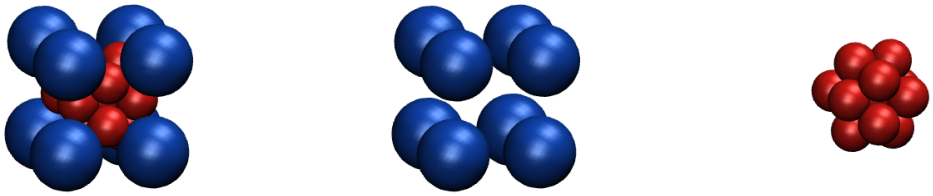

Figure 3.5: Example of a one-eighth of an AB_{13} unit cell (left) taken from the simulation snapshot of the binary mixture in spherical confinement. Big particles form a cubic cell (middle), in the centre of which an icosahedron made of 13 small particles is located (right).

λ_{AA}	λ_{BB}	λ_{AB}	structure
0	0	0	AB_{13}
1	0	0.1	core-shell
1	0.01	0.1	core-shell
≥ 0.8	0	0	Janus
1	≥ 0.1	0.1	Janus
1	1	1	AB_{13}

Table 3.1: Summary of the observed structures in molecular dynamics simulations after a large number of integration steps (up to 10^9) in the NVT ensemble for different combinations of solvation parameters λ_{ij}. The number ratio of small and large particles was always set to 1:13 while a total of up to 14000 particles were used in the simulations. Simulations were performed in a slowly shrinking spherical container with repulsive boundaries, but also in a fixed spherical container and in bulk.

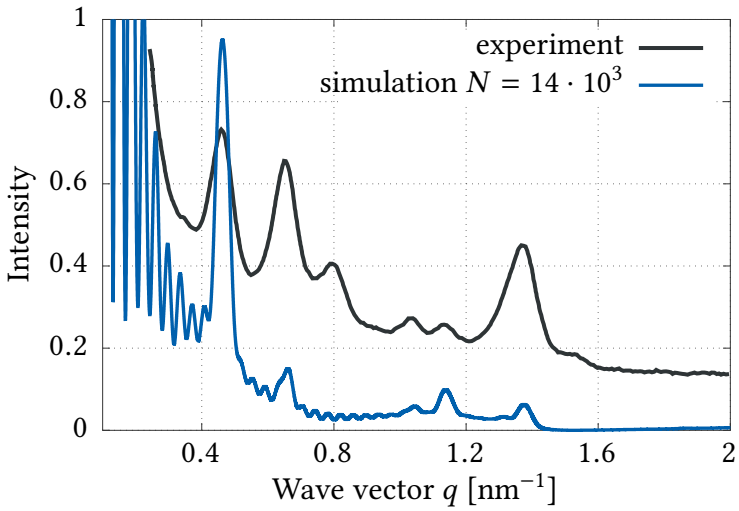

Figure 3.6: A comparison of the calculated SAXS scattering intensity as obtained using the Debye formula and the simulated AB_{13} crystalline snapshot of 14000 nanoparticles in a spherical container with the measured scattering intensity.

solid, homogeneous sphere is [171]

$$A(Q) = \frac{4}{3}\pi R^3 \frac{3\left[\sin(QR) - QR\cos(QR)\right]}{(QR)^3} \,. \tag{3.4}$$

Using a single snapshot of the equilibrated AB13 crystalline supraparticle that we obtained in the simulations we calculated the total scattering intensity normalised by the number of particles and compared it to the experimental measurements in Figure 3.6 Qualitative agreement is obtained, but the fact that certain peaks are missing in the simulated snapshots could be a consequence of lattice distortions (which can be seen in Figure 3.4) and a small number of particles used for calculating the intensity.

3.2.3 Experiments

Here we provide a brief description of experiments that were conducted by Thomas Kister at the Leibniz Institute for New Materials in Saarbrücken, further details can be found elsewhere [164].

Gold nanoparticles with different sizes were synthesised by a modification of the method where a reduction of chloroauric acid by an amine-borane complex proceeds in the presence of ligands in organic solvent [172]. Benzene was used as a solvent to create 8 nm nanoparticles while pentane was used to produce 4 nm nanoparticles which were afterwards characterised by the analysis of their transmission electron microscopy micrographs.

The nanoparticles were stabilised against agglomeration with an exchange of the ligands by heating and stirring at 80 °C where the old ligands were removed and the hexadecanethiol was

Table 3.2: Concentration of different Triton surfactants used to create hexane-in-water emulsions and their critical micelle concentrations (CMC).

Surfactant	Concentration [$g\,L^{-1}$]	CMC [$g\,L^{-1}$]
X-100	9.45	0.189
X-102	13.4	0.267
X-165	28.5	0.570
X-305	19.2	1.92
X-405	24.4	2.44
X-705	35.9	3.59

added. Afterwards the particles were purified, removed by centrifugation and resuspended in hexane.

Supraparticles were synthesised using a mixture of water, surfactants and hexane where the gold nanoparticles stabilised with hexadecanethiol ligands were dispersed. The mixture was stirred using a shear emulsifier which resulted in hexane-in-water emulsion. Heating to 50 °C for 12 h caused the evaporation of hexane from emulsion droplets and ordering of nanoparticles. Multiple nonionic Triton surfactants that differ by the length of their hydrophilic chains [173] were used to stabilise the emulsion, their critical micelle concentrations and the concentrations used in experiments are listed in Table 3.2.

Supraparticle structures were analysed using TEM and small angle X-ray scattering after being washed by centrifugation. Their size and dispersity was measured by dynamic light scattering and their interfacial tension was determined using pendant drop tensiometry where the equilibrated drop shape was recorded by a digital camera and fitted to the Young-Laplace equation. Pressure dependent experiments were conducted inside a pressure chamber where supraparticles were produced and where *in situ* SAXS analysis was conducted.

3.3 Structured supraparticles and pressure dependent formation mechanism

Confinement of a heterogeneous particle mixture made of gold nanoparticles with core diameters of 4 nm and 8 nm in hexane-in-water emulsion droplets using different surfactants resulted in the formation of structured supraparticles that are shown in Figure 3.1. Structure of supraparticles varied depending on the surfactants which were used to prepare hexane-in-water emulsions and whose hydrophilic tails had varying molecular weights in the aqueous phase. The shortest hydrophilic tails of Triton X-100 led to the formation of AB_{13} superlattices shown in Figure 3.1a. This structure is known already for 80 years from the intermetallic compounds such as $NaZn_{13}$, KZn_{13} and KCd_{13} [174, 175] and from colloidal crystals [176–179].

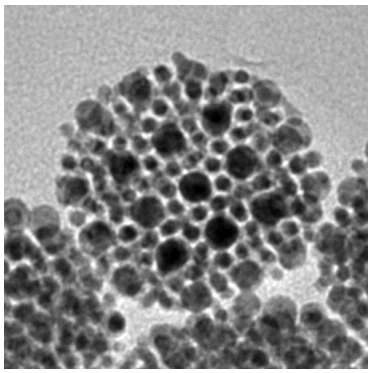

Figure 3.7: TEM micrograph showing an example of AB_{13} superlattice formed in emulsion droplet with a small number of encapsulated nanoparticles. Surprisingly the structure of supraparticle remains that of a bulk crystal even for very small numbers of confined nanoparticles. This is in contrast to the previous studies where it was found that structures depend on the number of confined nanoparticles and that for small numbers lower-symmetry geometries analogous to atomic clusters are stabilised [26, 81]. Image courtesy of Thomas Kister

It has also been observed in three-dimensional superlattices of magnetic nanocrystals and semiconductor quantum dots [180] and for binary nanoparticle superlattices by solvent evaporation in thin films [156] or in bulk [181]. AB_{13} supraparticles formed for a range of droplet sizes, including in very small droplets as shown for one example in Figure 3.7. This is in contrast to a previous study where supraparticle formed structures that are appreciably different from bulk lattices and also varied with the number of confined nanoparticles [26, 81]. Increasing the length of hydrophilic tails in surfactants has produced either Janus-type or core-shell phase separated supraparticles. Specifically Triton X-102 and X-165 led to Janus structures shown in Figure 3.1b, while Triton X-305, X-405, and X-705 led to core-shell supraparticles with randomly packed shell of small particles and crystalline cores of big particles shown in Figure 3.1c. In all cases gold nanoparticle cores with narrow size distributions were covered by hexadecanethiol monolayers and suspended in hexane in a concentration proportion of 1:13 for big and small particles. The slow evaporation of hexane from emulsion droplets decreased their diameters from around 2 μm to 150 nm on average which led to higher particle concentrations and subsequent ordering.

The choice of surfactants for creating emulsion droplets could affect the formation of different supraparticles structures through various mechanisms among which Marangoni flows, trapping of particles at the liquid-liquid interface and nucleation effects are probably the most significant ones. Heating of the sessile drops in which a mixture of nanoparticles of different sizes is dispersed induces Marangoni flows that sort the nanoparticles [182]. These flows are a consequence of inhomogeneities of the interfacial tension caused by the increased temperature and can be quantified by a Marangoni number that depends on quantities such as temperature difference, droplet radius, viscosity, thermal diffusivity and temperature rate of

the interfacial tension. Comparing their values shows that the Marangoni number in the case of our system is one order of magnitude smaller then the threshold value needed for the onset of Marangoni flows [183] which therefore can not play a significant role [164]. Pickering-Ramsden emulsions [184] on the other hand can be used to trap nanoparticles at the liquid-liquid interfaces [78]. However, for gold nanoparticles stabilised with alkanethiol ligands no segregation to hexane-water interface is observed with Triton surfactants [96] therefore we can exclude this effect as well.

Nucleation can be used to explain the formation of distinct structures through a mechanism where surfactant controls how different particles order into dense structures at different critical concentrations. Such agglomeration can develop at different times during evaporation process. When particles are well dispersible inter-particle potentials are repulsive and agglomeration occurs at high concentrations at a late stage of evaporation process, while low dispersibility of particles when they interact through attractive potentials leads to earlier agglomeration at lower concentrations.

The effect of surfactant on the onset of agglomeration for large and small particles is demonstrated by analysing SAXS measurements shown in Figure 3.8. Scattering intensities are shown at different times after the start of evaporation of solvent from emulsion droplets stabilised by Triton X-100, Triton X-165 and Triton X-705 surfactants whose hydrophilic chains include 10, 16 and 55 ethoxylate units on average. The shortest surfactant chains produce an AB_{13} crystal structure that forms already after 180 min by seemingly simultaneous agglomeration of small and large particles (Figure 3.8a). This is in contrast to the situation in emulsions with longer surfactant chains where at first the large particles agglomerate and only after some time the small particle agglomerate as shown by the corresponding peaks in scattering intensities. Figure 3.8b shows the formation of Janus supraparticles using Triton X-165 where the large particles agglomerate after 240 min while the peak for small particles appears after 420 min. In Figure 3.8c Triton X-705 is used to produce core-shell supraparticles where large particles agglomerate after 270 min while the small ones form a close-packed shell around them after 660 min.

Two trends can be observed from these measurements. The first is that with the increasing surfactant lengths both particle types tend to agglomerate after a longer evaporation time. Their critical concentration for agglomeration increases with surfactant length and consequently they agglomerate at higher concentrations at larger evaporation times. The second observation is that small particles agglomerate after the large ones with a delay that is increasing with surfactant length. This can be understood by the increased van der Waals attractions among larger particles in comparison to the same interactions among smaller particles [29].

Molecular dynamics simulations [165] were carried out to test which interaction potentials between nanoparticles produce the supraparticle structures observed in the experiments. This

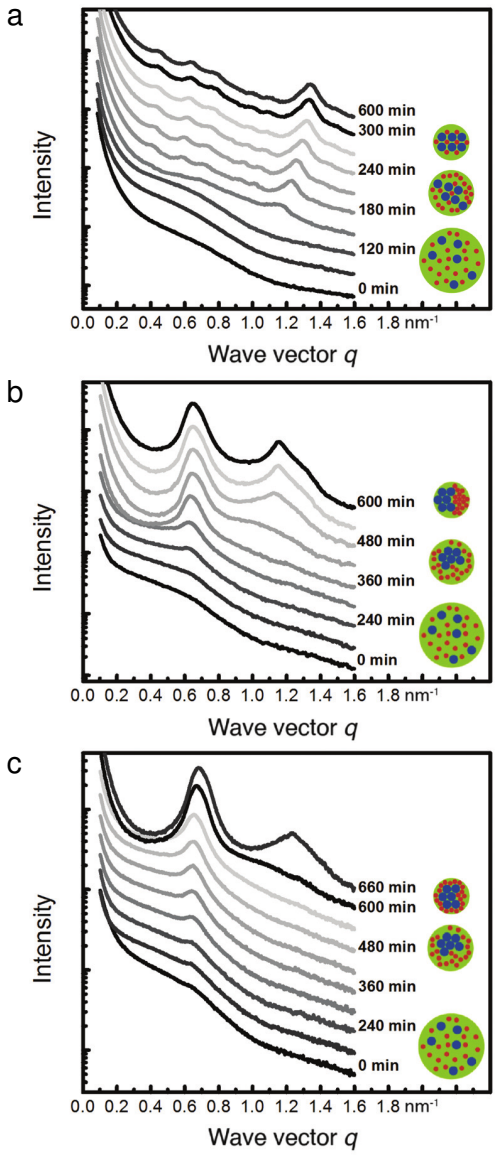

Figure 3.8: SAXS measurements at progressing times during the process of evaporation of solvent from emulsion droplets stabilised with different surfactants. (a) For Triton X-100 surfactant we can see that the AB_{13} superlattice forms after 180 min when the scattering peaks for both particles appear. (b) For Triton X-165 the scattering intensity shows first a peak for large particles after 240 min while the peak for small particles appears only after additional 200 min. (c) For Triton X-705 the large particles agglomerate after 270 min of evaporation while small particles remain dispersed a much longer time than in case (b) and suddenly agglomerate at the end. [164] - Reproduced by permission of The Royal Society of Chemistry

was achieved by the equilibration of an initially disordered binary mixture of particles confined to a spherical container. We used a total number of $7000-14000$ small and large particles with size ratios $0.55-0.58$ and number ratio of 13:1 that interacted through potentials ranging from a purely repulsive Weeks-Chandler-Andersen to a more attractive Lennard-Jones potentials [166] while the intermediate cases were modelled by linearly superimposing these two potentials.

Final configurations from simulations using different interaction potentials are shown in Figures 3.9a-c. Purely repulsive interaction potentials led to AB_{13} crystal structures of particles confined at high concentrations in a spherical container with a fixed volume. This is in agreement with previous studies which showed that AB_{13} is entropically the most stable lattice in a system of binary hard-spheres [163, 167]. When we added identical attraction to all particles regardless of their size the same AB_{13} crystal structure was obtained. We also observed that it formed at lower packing fractions, which is probably a consequence of a longer range of the inter-particle potential.

Simulations in a shrinking spherical container were performed to emulate the effect of droplet evaporation. In a system where attractive interactions are added only to the large particles of the mixture, the concentration increase during shrinking resulted in the core-shell supraparticles. This models cases where the van der Waals attractions between larger particles dominate agglomeration [29]. However, when attractive interactions are added to both particle types, Janus supraparticles are produced. One example of the stages during formation process for a Janus supraparticle are shown in Figure 3.9 where isolated agglomerates of the larger particles nucleated and merged, while the smaller particles remained disordered until they crystallised at a later stage. The results of simulations are therefore consistent with the assembly model and the SAXS measurements confirming that larger particles exhibit stronger attractive interactions than smaller particles with the same ligand monolayers.

A question that raises naturally from the discussion so far is how can the potentials between nanoparticles be affected by the surfactants that differ only by the length of their hydrophilic chains? We believe that this is not due to chemical interactions of particles with the liquid-liquid interface but because of different pressures induced inside emulsion droplets. Arguments are presented below to strengthen this but more detailed studies on the molecular scale would be required to determine the precise mechanism connecting pressure and inter-particle potentials where effects such as arrangement of ligand monolayers and solubility of water in oil would have to be considered.

The Laplace equation, $\Delta p_L = 2\gamma/r$ [185], determines the pressure difference between the interior and the surrounding of a sphere of radius r with γ specifying the interfacial tension. The interfacial tension of the liquid-liquid interface for emulsion droplets depends on the surfactant that is used to produce them. This has been confirmed by tensiometry experiments

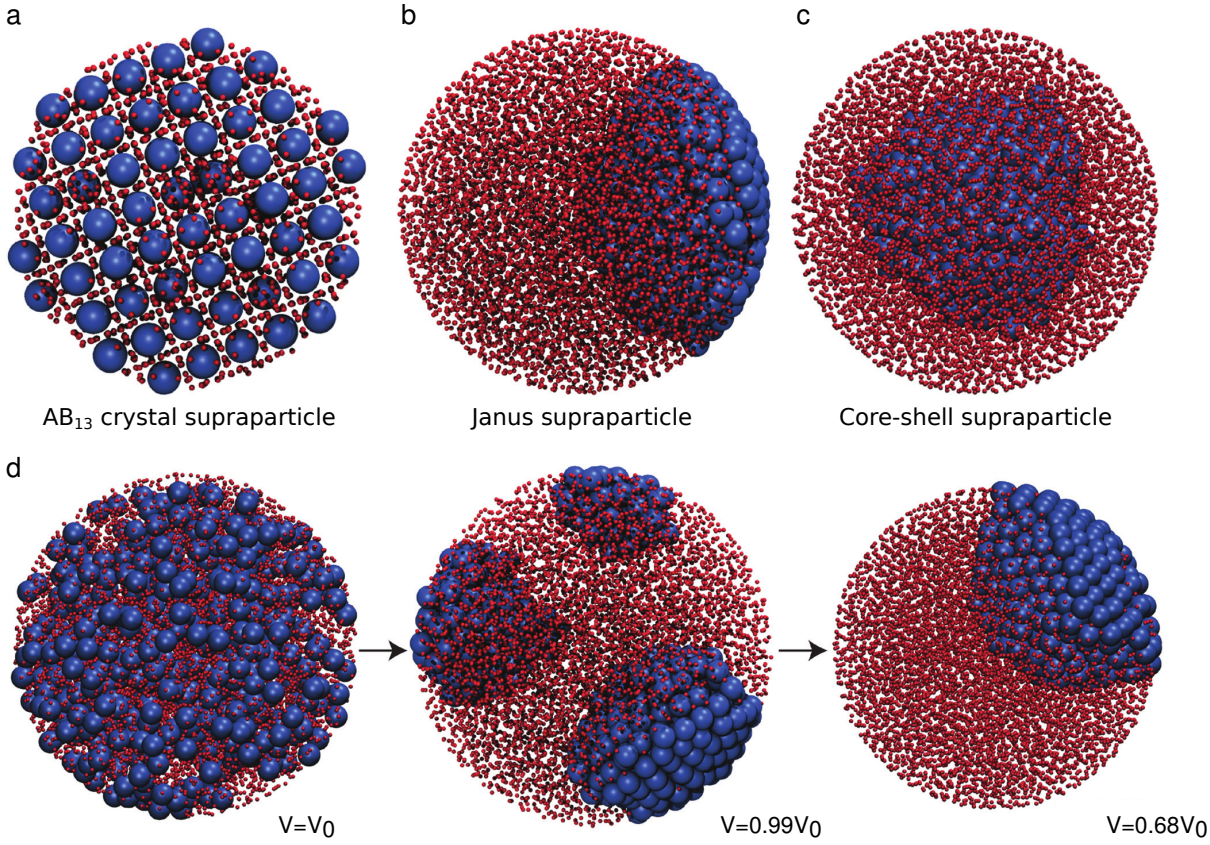

Figure 3.9: Snapshots of systems simulated by a molecular dynamics method where a mixture of small and large particles was constrained to a spherical container which was slowly shrinking during the process or held at the constant volume (only for the case (a)).
(a) A superlattice with AB_{13} crystal structure that is entropically stabilised forms for purely repulsive pair interactions which approximates the situation at the high pressure regime. Same lattice was also obtained when all particles interacted with the same attractions added to their repulsive cores which models the low pressure experiments. The intermediate pressure regimes are modelled by adding different attractions to large and small particles. (b) When the large particles are attracting each other but smaller ones are purely repulsive or have smaller amounts of attractions then core-shell structures are obtained. (c) A mixture with attractive large particles and with increased attractions between smaller nanoparticles led to Janus supraparticles. (d) Three snapshots showing the formation of a Janus supraparticle during a shrinkage of the spherical container. A fully dispersed initial state is shown on the left just before the agglomeration started. Larger particles then formed separate agglomerates that slowly merged among disordered smaller particles. In the end they combined into a single domain that is positioned on the side of the container while small particles crystallise on the other side of the container. Between the start of agglomeration and the end the volume of sphere decreased by around 30%. [164] - Reproduced by permission of The Royal Society of Chemistry

where γ was measured for the hexane-water interface of the macroscopic drops at concentrations above CMC. Results shown in Figure 3.10a indicate Laplace pressures between 10 kPa and 300 kPa for Triton X-100 and X-705 respectively, for droplets with diameter 150 nm. To test that the exact chemical nature of the surfactant does not affect the supraparticle structures, an anionic surfactant sodium dodecyl sulfate (SDS) was used instead of Triton X-165 to produce Janus-type supraparticles which confirms the importance of pressure on the inter-particle potentials.

The effect of pressure on dispersibility of nanoparticles was already investigated by Korgel and coworkers who demonstrated that the critical concentration for agglomeration of alkylthiol-stabilised gold nanoparticles in supercritical ethane increases with pressure [186]. In Figure 3.10b a similar effect is shown for nanoparticles in emulsion droplets where SAXS measurements indicate pressure-dependent dispersibility. A reversible transition between a state with agglomerated and dispersed large particles that happens on the order of seconds is achieved by changing the pressure. This indicates that pressure reduced attractions between large particles, while the small particles remained dispersed probably due to smaller attractions of size-dependent van der Waals forces.

The hypothesis that pressure determines supraparticle structures was tested in experiments with emulsion droplets that were stabilised by Triton X-100 and where varying external pressure was applied [164]. It was found that without the environmental pressure the self-assembly resulted in supraparticles with AB_{13} superlattices while with an isostatic external pressure applied different supraparticles structures could be produced. Janus structures formed at 100 kPa, core-shell supraparticles at 300 kPa, supraparticles with partially Janus-type and AB_{13} structures at 600 kPa and the AB_{13} superlattice were produced again at 1000 kPa. The pressure that caused "switching" between different structures was comparable to the Laplace pressures that caused the same supraparticle structures for different surfactants before.

Emulsion droplets that encapsulate varying numbers of nanoparticles have different sizes which cause different Laplace pressures for the same surfactant that also changes with time during the evaporation of solvent. This effect is stronger for larger surface tensions and is probably the cause of imperfections that were especially noticeable for core-shell structures formed with Triton X-705 surfactant. However, when pressure was applied core-shell structures were more regular as external pressure is independent of droplet size and thus causes less disturbances during crystallisation. Also when shorter dodecanethiol ligands were used instead of hexadecanethiol to stabilise the nanoparticles, larger pressures were required to form Janus and core-shell supraparticles. This can be understood by increased attractions between gold cores that needs to be balanced by larger pressures to restore conditions necessary for self-assembly [187].

At higher external pressure AB_{13} crystal structure surprisingly reappeared, at first only

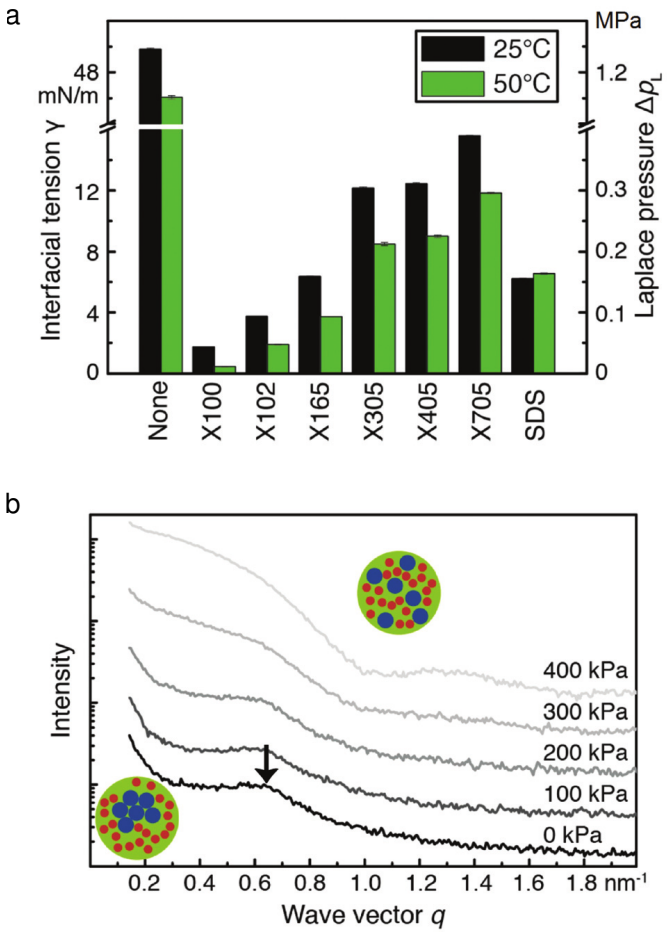

Figure 3.10: Experiments demonstrating that varying surfactants change the interfacial tension of emulsion droplets and that the pressure inside droplets modifies dispersibility of encapsulated nanoparticles. (a) Results of hanging droplet tensiometry measurements show the interfacial tension of the hexane-water interface at two different temperatures and the corresponding Laplace pressure differences inside a droplet of radius 80 nm. (b) SAXS experiments with a binary dispersion of nanoparticles in emulsion droplets using surfactant Triton X-165. Intensities are measured after 240 min of evaporation at 50 °C for different ambient pressures. The scattering intensity peak for large particles that is marked with an arrow can be seen at low pressures but disappears at higher pressures which indicates that particles become dispersed. [164] - Adapted by permission of The Royal Society of Chemistry

partially and then entirely filling the supraparticles. This was not observed before with different surfactants because none of them could cause a pressure increase as high as 1000 kPa. Intriguingly the AB_{13} structure had a low density with gold cores having a volume fraction of only 28% in comparison to above 40% for Janus and core-shell supraparticles. Space-filling arguments can therefore be excluded as an explanation for the pressure-dependent supraparticle structure which thus have to be a result of pressure-modified inter-particle potentials that affect the self-assembly by confinement in emulsion droplets.

Experiments and simulations of self-assembly in droplets can be explained by a formation mechanism based on agglomeration and confinement which is outlined in Figure 3.11 and is in part similar to processes described in the formation of Janus particles in flame spray pyrolysis where a mixed phase decomposes into a solid and a liquid that solidifies later [188]. We distinguish a low pressure regime where agglomeration happens early in the evaporation process leading to the formation of AB_{13} supraparticles and a high pressure regime where both particle types remain dispersed until the end of the evaporation process when confinement forces them to order, again to AB_{13} structure. At the intermediate pressures large particles agglomerate at higher concentrations where the lack of solvent inhibits their mobility and they are thus not able to form the complex AB_{13} lattice. Janus supraparticles then usually form as the smaller particles tend to agglomerate into separate single crystals. But in a limited range of pressures large particles agglomerate while the small ones remain dispersed almost until the end of the evaporation which leads to core-shell supraparticles where confinement forces small particles to arrange into a dense but disordered shell around the crystalline core of large particles.

3.4 Conclusions

Highly ordered binary supraparticles can be formed inside evaporating emulsion droplets with different structures that are controlled by the applied external pressure or the surfactant used to create emulsions. Such finite size binary superlattices are a promising class of materials as they combine organic ligands with inorganic cores that can have interesting magnetic, plasmonic, fluorescent and catalytic properties in contrast to e.g. diblock copolymer particles [189]. A mixture of cores with two different properties combined in regular arrangements could lead to new patchy building blocks that are desired in the self-assembly of colloidal materials with enhanced characteristics. Small changes in the pressure provide a simple way of control structures of particles at the nanoscale. This is a prototypical soft-matter effect where moderate changes of external conditions have large effects on the solubility and structure of self-assembled clusters. This effect could be also applied in a more commonly used protocol of nanoparticle assembly in thin films.

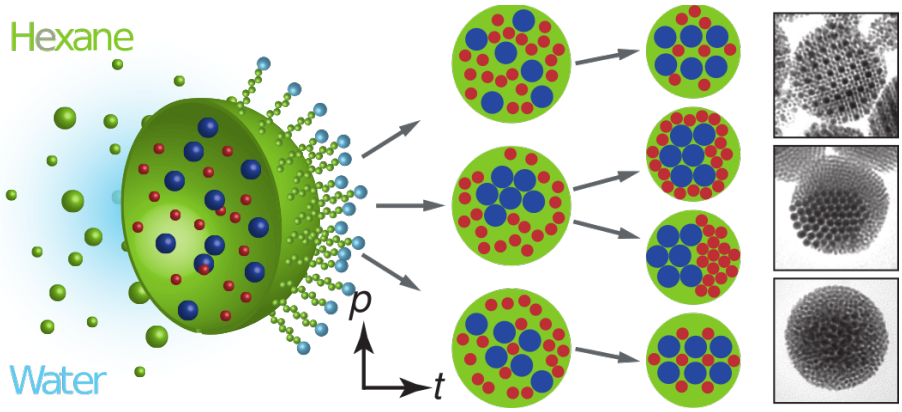

Figure 3.11: The suggested mechanism of formation of different supraparticle structures from the same binary dispersion inside the shrinking emulsion droplets. The increase of pressure leads from AB_{13} to Janus, to core-shell, and again to AB_{13} crystal structure due to the modification of inter-particle potentials by the pressure. At low pressures agglomeration occurs early by nucleation and growth, while at high pressures particles remain dispersed until high concentrations cause their agglomeration. At intermediate pressures varying dispersibilities of large and small nanoparticles lead to the formation of Janus or core-shell supraparticles. [164] - Adapted by permission of The Royal Society of Chemistry

The properties of ligand monolayers play a crucial role in the self-assembly of nanocrystals. Detailed studies of ligand shell stability and solvation properties at varying pressure could provide an explanation for pressure-dependent inter-particle potentials [186]. The same mechanism could therefore be expected for other nanocrystals coated with alkane ligands. This could be used to combine different kinds of nanoparticles such as plasmonic metal particles, catalytic oxide particles, and fluorescent semiconductor quantum dots to form new functional supraparticles. If particles in the resulting agglomerates could remain mobile as has been indicated depending on the choice of ligand shell [190] changes in the arranged supraparticles could be used to sense pressure differences in the environment.

Chapter 4

Equilibrium phase behaviour of Mackay icosahedra

Mackay icosahedron is a repeating motif in different types of nanocrystals and therefore an important element in self-assembly of superlattices. In this chapter we investigate the equilibrium phase behaviour for a monodisperse system of Mackay icosahedra using molecular simulations. We define icosahedra as nonlinear polyatomic molecules composed of a set of Lennard-Jones subparticles arranged on a surface of the Mackay icosahedron. After equilibration of initially ordered or disordered states we find either a fluid phase, a crystal phase or rotator phases with different degrees of rotational correlations. To analyse the correlations in equilibrated states we calculate their positional and orientational pair correlation functions and find that at high enough temperatures icosahedral molecules function similar to hard geometric icosahedra for which the densest lattice packing and the rotator crystal phase have been calculated before. New behaviour is observed at lower temperatures where increased importance of energetic interactions results in preferred face to face alignment forming rotator crystal or presumably complex crystal arrangements. This leads to the re-entrant behaviour with increasing temperature where first a transition to the densest lattice crystal occurs and then the rotator phase is formed at higher temperatures due to the prevailing excluded volume effects.

4.1 Introduction

When small numbers of atoms or molecules interacting through simple isotropic potentials with repulsive cores and short ranged attractions are forced together they tend to form local densely packed clusters where a central atom is covered with 12 nearest neighbours located at the vertices of an icosahedron. Since these structures posses a five fold symmetry which is a forbidden crystal symmetry they can not extend to large length scales but are instead often seen as favoured, persisting local structures in supercooled liquids and glass-forming substances [140, 191].

Mackay generalised this construction to larger multiply twinned superlattices of densely packed spherical subparticles with icosahedral symmetry [148]. These are composed of 20 slightly deformed close-packed tetrahedra which are merged together in such a way that their adjacent planes form twinning crystal domains while their outer planes constitute the 20 faces on the surface of an icosahedron (Figure 4.1). For not too large numbers of constituent particles Mackay icosahedra have been shown to globally minimise the Lennard-Jones potential energy surfaces [192], result in enthalpy-driven assembly of colloids [83] and maximise entropy in spherical confinement of hard-spheres [81]. These polyhedral nanocrystals are favoured local structures in diverse systems such as noble gas atoms and molecules [193], gold nanoparticles [26] and clusters of metal atoms [194]. They are thus ubiquitous in nature and constitute an important class of structures.

Confinement of spherical gold nanoparticles inside spherical surfaces of emulsion droplets leads to an assembly of nanocrystals with superlattices corresponding to Mackay icosahedra [26]. Structures of such clusters keep the polyhedral character also for binary mixtures of particles with different attractions [195] while differences in atmospheric pressure can determine the formation of either a complex binary crystal superlattice or core-shell or Janus clusters in dispersions of nanoparticle with binary size distributions [164]. Mackay icosahedra have also been observed for collections of nanometer- and micrometer-sized hard, spherical colloids in spherical confinement [81]. If a monodisperse system of such icosahedral nanocrystals was created it could be used in a bottom up design of functional materials. To determine the properties of these materials an understanding of their equilibrium phase behaviour is necessary.

Finding the optimal arrangements of congruent objects that do not tile space and its associated maximal density is an ancient mathematical challenge that remains unsolved for all non-trivially shaped objects except for the sphere whose densest packing was conjectured already by Kepler and has only been proven about a decade ago [196]. A more recent conjecture suggests that the densest packings of centrally symmetric Platonic and Archimedean solids are their corresponding optimal Bravais lattice packings [197]. For hard icosahedra (and several other regular polyhedra) such densest lattice packing has been determined using different numerical optimisation algorithms [197–199]. This putative optimal arrangement is a locally

jammed packing with density 0.8363574 where each icosahedron contacts 12 neighbours and is represented by a Bravais lattice with a triclinic unit cell where each point contains a single uniformly oriented body (see Figure 4.2b). Another work has shown that a dense fluid of hard icosahedra assembles into a close packed (FCC or HCP) rotator crystal where particles are allowed to freely rotate about their lattice positions [200]. Packing small numbers of hard icosahedra in a hard-spherical container results in clusters that resemble or match sphere clusters (optimal sphere codes) despite significant faceting of these objects [201].

Bulk behaviour of Mackay icosahedra has not yet been studied systematically although such structures are ubiquitous in Nature and could have technologically important implications for material science. In the present work we attempt to explore equilibrium phase behaviour at finite temperatures using Monte Carlo simulations. We choose to study phase behaviour for an icosahedron composed of 55 particles arranged in a Mackay fashion as its size is small enough to be computationally feasible while it still captures the geometrical features of icosahedra and allows for a description of energetic attributes of such objects. We show that the predicted densest packing and rotator phases for hard icosahedra are also stable at finite temperatures. In the low temperature regime we investigate the re-entrant behaviour due to increased importance of energetic interactions which are not captured by the hard icosahedron model. We also give a description of simulation methods and structural measures used in the analysis of equilibrated phases.

4.2 Simulation methods

The Mackay icosahedron shown in Figure 4.1 is composed of 55 subparticles arranged in two complete shells around its centre. This quasi-spherical arrangement is a particularly stable motif in the minimal energy Lennard-Jones diagrams for binary systems of particles in a wide range of different attraction ratios [195]. Some of its geometrical properties are given in Table 4.1 where we see that the volume of icosahedron fills only 58.2% of the circumscribed sphere. Due to this significant deviation from a spherical shape entropical effects are expected to play an important role in systems of such molecules. We estimated the volume of the molecule with a Monte Carlo integration using an effective repulsive radius of subparticles, $r_{\mathrm{rep}}^{\mathrm{eff}} = 2^{1/6}\sigma/2$, where σ is the usual Lennard-Jones potential range parameter.

The interaction energy between two icosahedral molecules depends on the distance between their centres and on their mutual orientation. The icosahedron is a nonlinear, rigid molecule whose configuration is given by a translational vector of its centre $r = (x, y, z)$ and a quaternion $q = (a, b, c, d)$ specifying its orientation. To calculate the positions of all subparticles

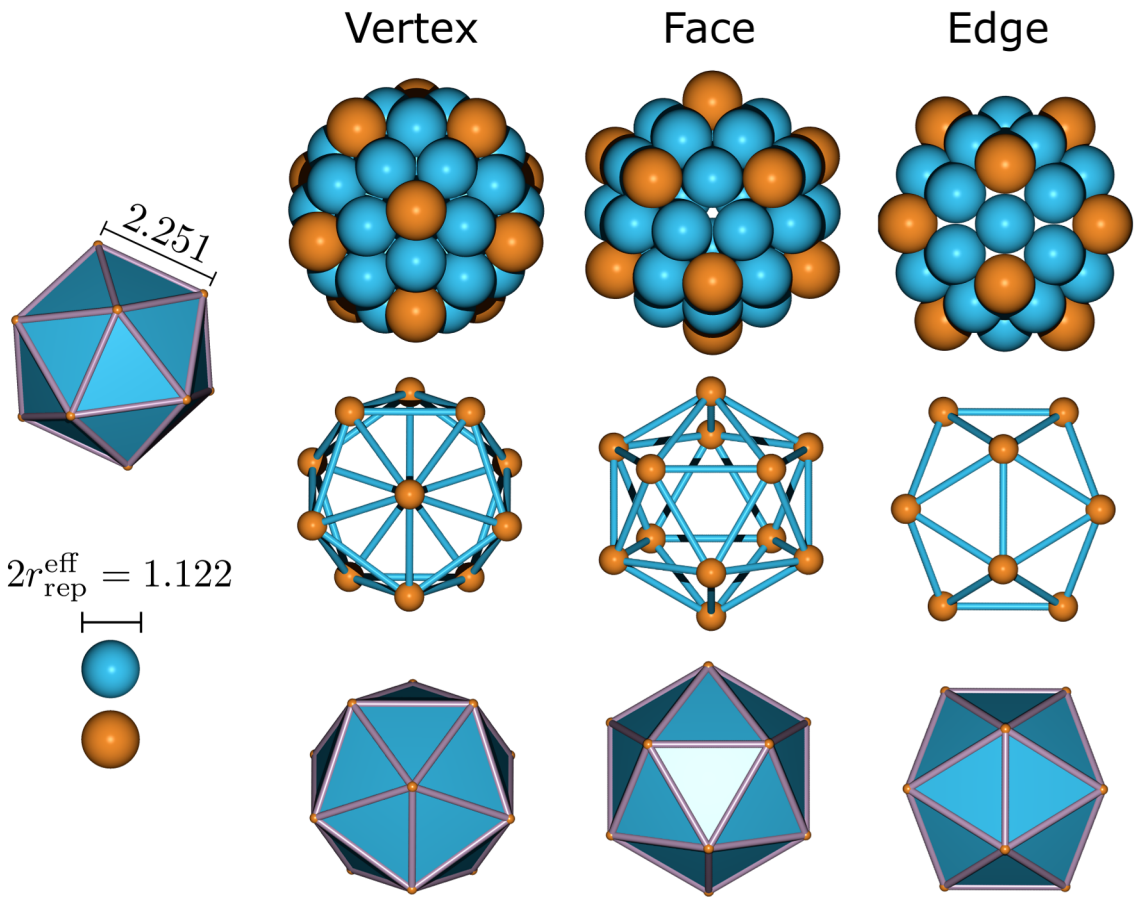

Figure 4.1: Mackay icosahedron is composed of 55 subparticles but only the 42 centres on the surface are considered as a model in simulations. Three different projections (vertex, face, edge on) and three visualisation models (space filling, ball and stick, polyhedron) with dimensions in units of σ are shown. Orange color denotes particles sitting at the 12 vertices of the shell. The radius of spheres is the effective (repulsive) LJ radius $r_{\mathrm{rep}}^{\mathrm{eff}} = 2^{1/6}\sigma/2$. To ease the visualisation of a system of such model particles we present them as regular polyhedra by a collection of flat faces with round edges and vertices.

inradius r_{in} $[\sigma]$	1.835
circumradius r_{out} $[\sigma]$	2.141
effective circumradius $r_{\mathrm{out}}^{\mathrm{eff}}$ $[\sigma]$	2.702
effective volume V^{eff} $[\sigma^3]$	48.091
equivalent spherical radius $r_{\mathrm{ic}}^{\mathrm{ES}} = (V^{\mathrm{eff}})^{1/3}$	3.637
scaled exclusion volume $V^{\mathrm{eff}}/V_{\mathrm{out}}^{\mathrm{eff}}$	0.582

Table 4.1: Geometrical properties of the Mackay icosahedron model particle (Figure 4.1) used in the simulations. σ is the Lennard-Jones potential range parameter describing interactions between pairs of subparticles. The effective radius and volume take into account the repulsive range of the Lennard-Jones potential, $r_{\mathrm{rep}}^{\mathrm{eff}} = 2^{1/6}\sigma/2$.

after the rotation we use a rotation matrix given by

$$R = \begin{pmatrix} a^2+b^2-c^2-d^2 & 2(bc-ad) & 2(bd+ac) \\ 2(bc+ad) & a^2-b^2+c^2-d^2 & 2(cd-ab) \\ 2(bd-ac) & 2(cd+ab) & a^2-b^2-c^2+d^2 \end{pmatrix}. \tag{4.1}$$

We then calculate a sum of Lennard-Jones terms of all the pairs of subparticles

$$U(r_1, r_2, q_1, q_2) = 4\epsilon \sum_{i=1}^{N} \sum_{j \neq i}^{N} \left[\left(\frac{\sigma}{r_{ij}} \right)^{12} - \left(\frac{\sigma}{r_{ij}} \right)^{6} \right], \tag{4.2}$$

where r_{ij} is the distance between subparticles i and j and $N = 42$. We apply a cutoff of $2.5\,\sigma$ to the interaction between two subparticles and thus exclude the contribution of the core particles. Additionally a cutoff of $7.0\,\sigma$ is applied on the interaction between a pair of icosahedra.

The effective (repulsive) diameter of icosahedron is in a range $d_{\text{rep}}^{\text{eff}} \in [4.7922 - 5.4046]\,\sigma$. Taking into account that the Lennard-Jones system compares to a square-shoulder system with parameter $\lambda \sim 1.5$ [202] we estimate that a system of icosahedra is comparable to a square shoulder potential with attractive range coefficient $\lambda \sim 1.1$. It is expected that equilibrium behaviour of icosahedra will show qualitative features similar to those in polymer-colloid mixtures of a comparable attraction range which can be tuned by the size ratio of the depletant and colloids [203].

To equilibrate a monodisperse system of icosahedra with periodic boundaries we use a Monte Carlo method [65] in the isobaric-isothermal ensemble with variable box size technique [204, 205]. To release the eventual stresses in the orthogonal simulation box we additionally employ Parrinello-Rahman sampling of the variable box shape [67, 206–209]. The deformations of the simulation box are limited to avoid nonphysically deformed systems. Initially the icosahedra are forming a low density disordered fluid without any overlaps or they are positioned on a spherical FCC lattice with arbitrary orientations. Two million Monte Carlo cycles are performed to equilibrate several different initial conditions at given pressures and temperatures of the system. Displacement and rotational moves are used to sample configurations where random orientations of nonlinear molecules are generated by sampling quaternions on the surface of the 4D unit sphere [210]. We chose the sizes of steps such that acceptance rates were around 30% but we did not change them during the simulation.

We use different structural descriptors to analyse the positional and orientational behaviour in a system of icosahedra. The positional order is monitored by computing the radial distribution function. Steinhardt bond orientational order parameters are used to quantify the bond network of nearest neighbours [140]. In both quantities icosahedra are replaced by

points lying in their centres (centroids). To measure the amount of orientational order in a system of nonlinear molecules we define a set of characteristic vectors attached to the model molecule. In the case of Mackay icosahedra we chose either the normals of the 20 triangles or the vectors pointing from the centre to the 12 vertices on the surface of icosahedron, the results are similar for both choices. The orientational pair correlation function (OPCF) can then be defined as [211]

$$g_{\mathrm{opcf}}(r) = \frac{\sum_{i=1}^{N}\sum_{j\neq i}^{N} \delta(r - r_{ij}) \left(\sin^2 \alpha_{ij}^{F_1} + \sin^2 \alpha_{ij}^{F_2}\right)/2}{\sum_{i=1}^{N}\sum_{j\neq i}^{N} \delta(r - r_{ij})} \tag{4.3}$$

where $\alpha_{ij}^{F_1}$ and $\alpha_{ij}^{F_2}$ denote the first and the second minimal angles formed by any pair of the characteristic vectors associated to particles i and j such that $\alpha_{ij}^{F_1} \leq \alpha_{ij}^{F_2}$. The values of such a pair correlation function can get arbitrarily close to zero for highly orientationally ordered systems while its maximum values are limited with the largest values of the minimal angles which depend on the choice of characteristic vectors.

4.3 Equilibrium phase behaviour

To explore the possible equilibrium phases in a system of 500 monodisperse icosahedra we carry out Monte Carlo simulations in the NPT ensemble for a range of temperatures and pressures. We quantify the positional and orientational correlations in the equilibrated systems using radial distribution function and orientational pair correlation function. Snapshots of the systems with four different structures that were observed as stable are shown in Figure 4.2.

In Figure 4.3 we analyse the behaviour of positional order in a system at constant pressure for three different temperatures. We see that icosahedra arrange on a FCC lattice at low temperatures, then transform into a BCC lattice with increasing temperature and then turns back into the FCC. This trend was observed at almost all values of the pressure that we studied but became less strong at higher pressures where icosahedra form phases without long range positional or orientational order at low temperatures.

The orientational pair correlations were computed using the normals of the 20 faces of an icosahedron and are shown in Figure 4.4 for the same three systems. Small values correspond to high mutual alignments while the strong oscillations are a consequence of regular particle positions as OPCF is defined analogously to the RDF histogram but with different weighting factors. A system at $T = 4$ shows large and long-range orientational correlations and by visual inspection we can indeed confirm that icosahedra are almost entirely uniformly aligned. In the other two systems icosahedra are orientationally disordered but show different

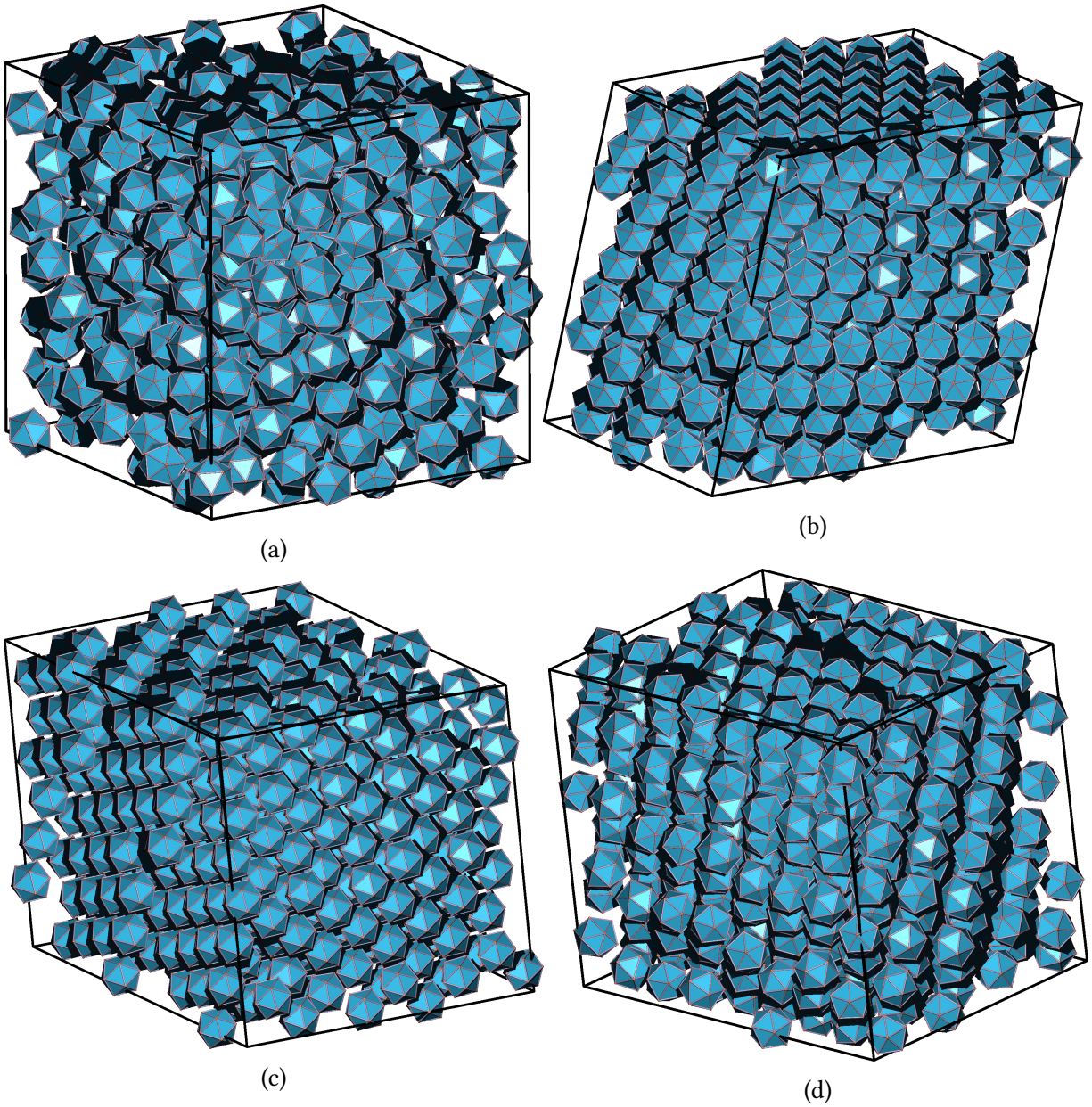

Figure 4.2: Snapshots showing different phases that formed after the equilibration of systems with 500 icosahedra in a deformable parallelepiped with periodic boundary conditions. (a) A liquid phase formed at $T = 1$, $p = 2$ shows neither long range orientational nor positional correlations. (b) A crystal phase with densest icosahedral lattice packing was produced at $T = 3, p = 1$. (c) Another orientationally aligned crystal phase formed at $T = 4, p = 1$, but time icosahedra arranged on a BCC lattice. (d) At higher temperatures orientationally uncorrelated rotator crystal phases with FCC positional order were formed, here a system at $T = 5$ and $p = 1$ is shown.

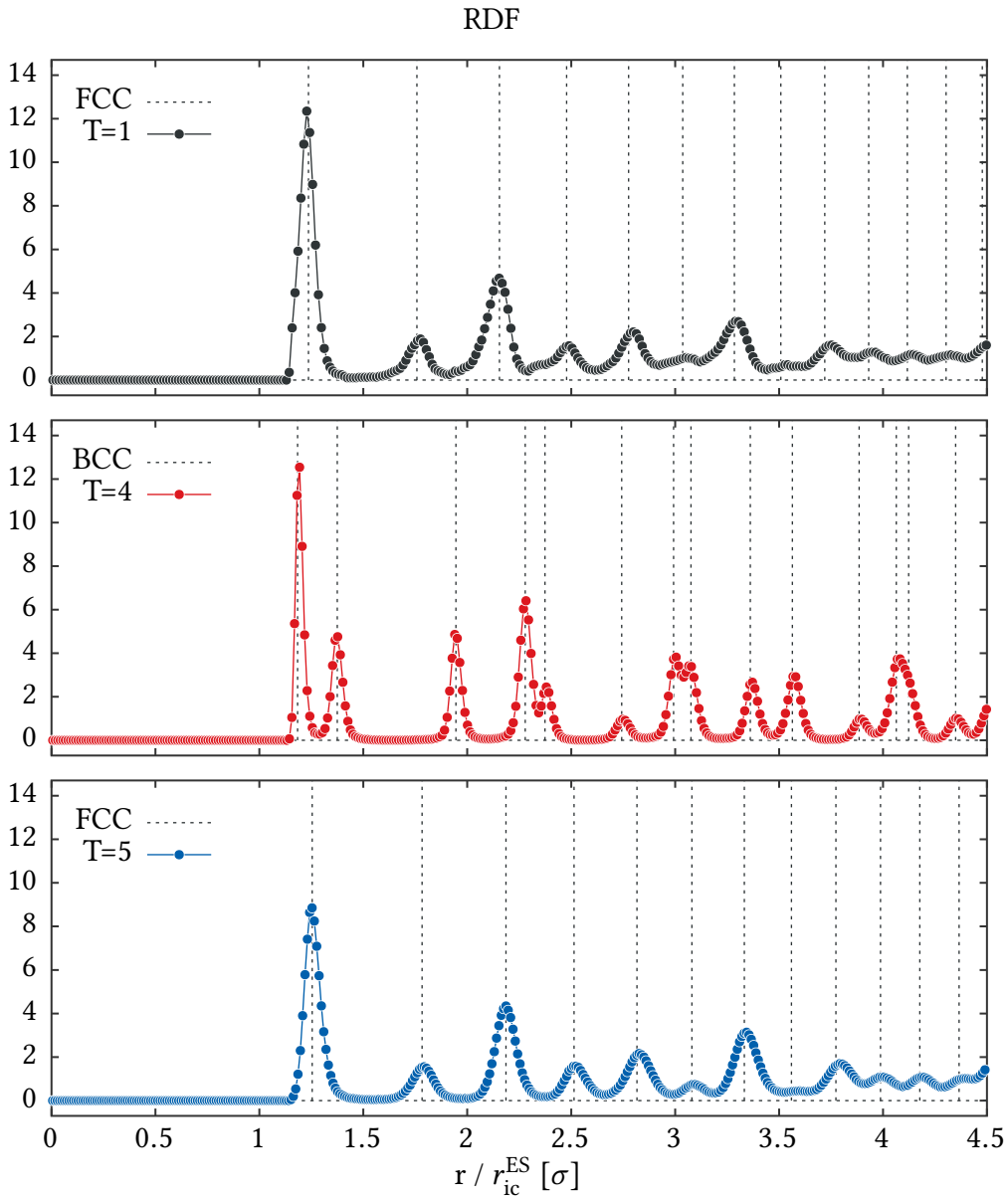

Figure 4.3: Radial distribution function for an equilibrated system of 500 monodisperse icosahedra at $p = 1$ for three different temperatures. The pair distances are given in units of an equivalent spherical radius of icosahedra r_{ic}^{ES}. The dashed lines show the distances represented in an FCC or BCC crystal lattices. The corresponding effective packing fractions, defined as the ratio of the volume taken by spheres with effective repulsive radius, are $\rho^{eff} = 0.46$ (for $T = 1$) and $\rho^{eff} = 0.69$ (for $T = 4$ and $T = 5$).

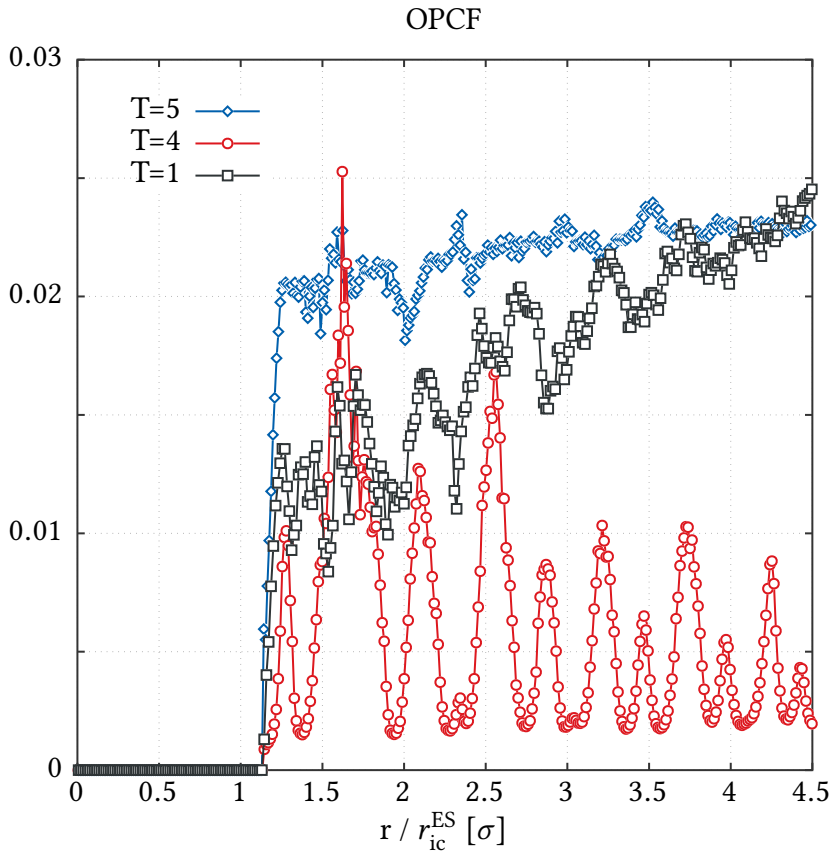

Figure 4.4: Orientational pair correlation function $g_{\mathrm{opcf}}(r)$ for an equilibrated system of 500 monodisperse icosahedra at $p = 1$ for three different temperatures. Long-range orientational correlations are present at $T = 4$ while the other two systems are orientationally disordered with different degrees of orientational correlations.

degrees of orientational correlations. At low temperature we see indications of short-range orientational correlations which are expected due to preferable face-to-face orientations of the nearest neighbours. With increasing temperature the system at $p = 1$ therefore undergoes a re-entrant transition from a rotationally disordered FCC crystal to an aligned BCC crystal and back to a rotationally disordered FCC lattice.

The results for equilibrated systems at a number of different pressures and temperatures are shown in Figure 4.5. We tried to categorise the resulting phases into four groups according to the measures of the orientational and positional correlations and the bond orientational order parameters [140, 143]. At very low pressures, the box deformation moves in the Monte Carlo algorithm sometimes produced unphysically shaped boxes that induced long-range orientational order, but otherwise no valid equilibrated states with liquid crystalline order were observed. We find the trend of going from a rotator crystal to a crystal and back to a rotator crystal phase with the increasing temperature for a range of pressures. This confirms our expectations that the exact geometrical shape of an icosahedron is relevant only up to some

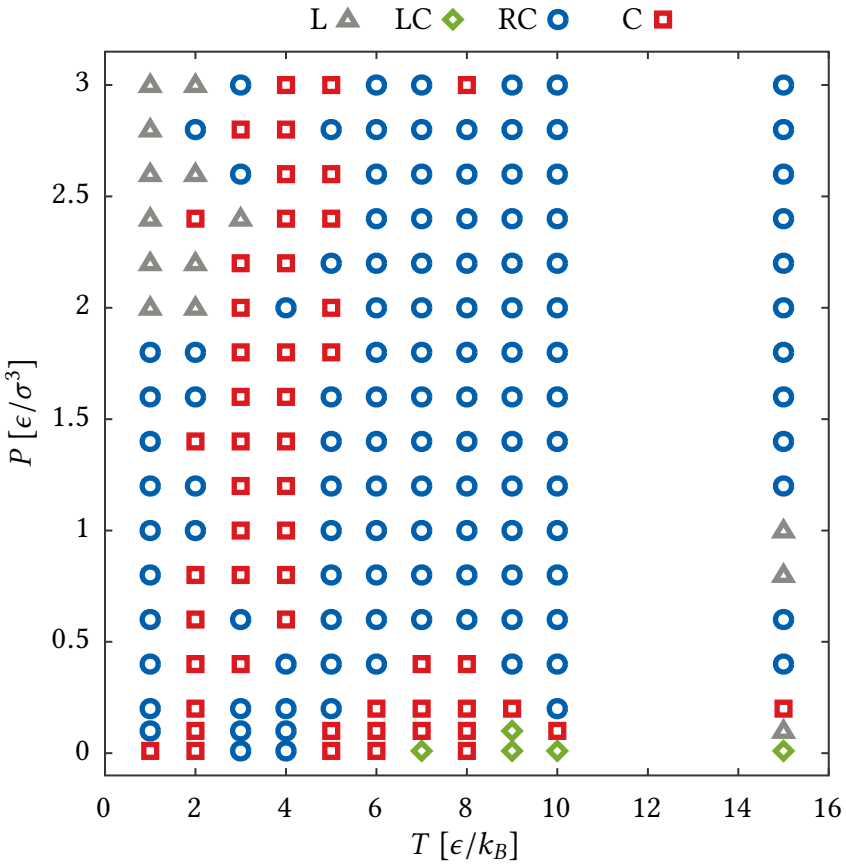

Figure 4.5: Scan of a phase diagram obtained by equilibrating a system of 500 Mackay icosahedra at constant values of temperature and pressure. The resulting structures are classified into four categories, crystal (C), rotator crystal (RC), LC (liquid crystal) and liquid (L), based on the criterion including the average value of OPCF and the values of the average bond order parameters Q_4 and Q_6.

temperature above which icosahedra behave as spheres while at low temperatures energetic interactions become important and destabilise long-range orientational order.

In the analysis of the phase diagram scan we did not precisely categorise different crystal phases, we noticed however, that when positional order was present it was either FCC for rotator phases or BCC and densest icosahedral packing for crystal phases. The densest lattice packing of hard icosahedra was observed at low pressure, $p = 1$, and at temperature $T = 3$. Both correlation functions of this system are shown in Figure 4.6 where a comparison is done with the densest lattice of hard icosahedra [199], the snapshot from the system can be seen in Figure 4.2b.

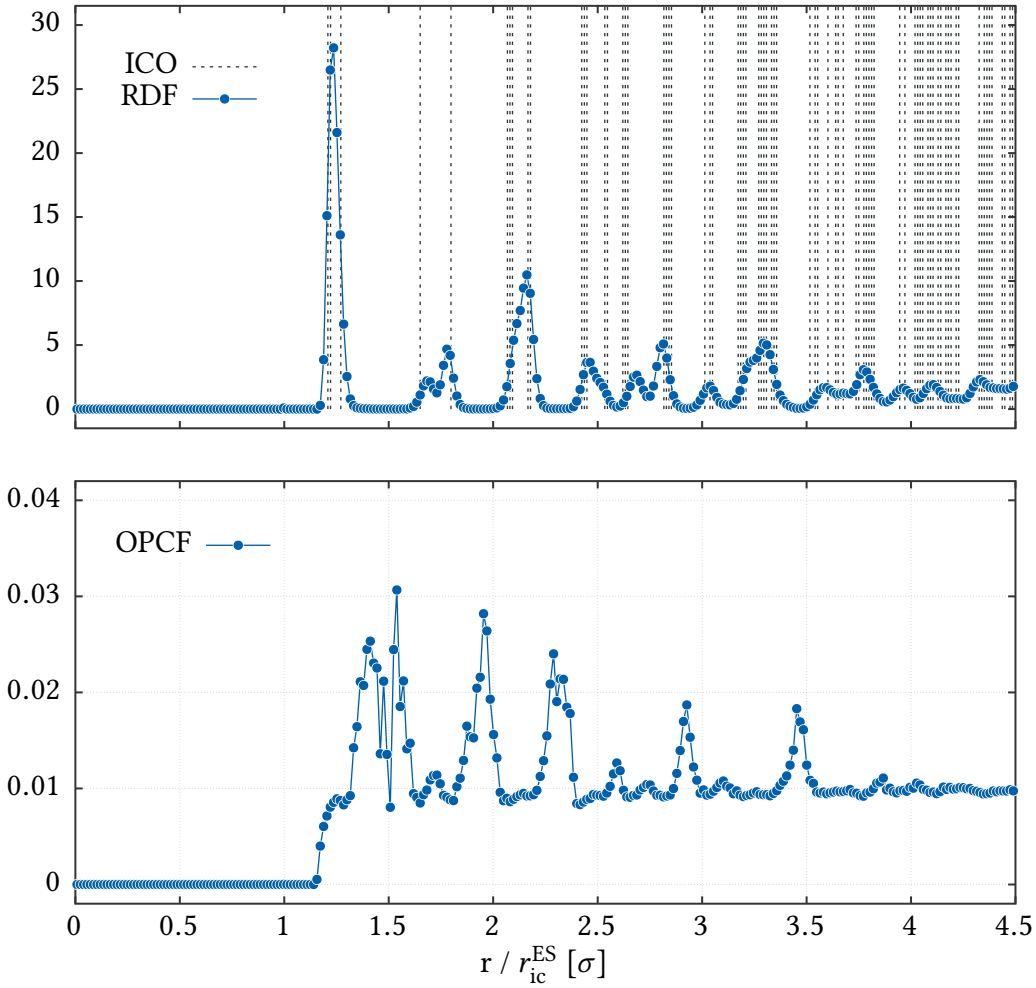

Figure 4.6: Positional and orientational pair correlation functions for a system with $T = 3$ and $p = 1$ ($\rho^{\text{eff}} = 0.51$). Radial distribution function is compared with the distances found in the densest lattice packing of icosahedra.

4.4 Conclusions

We have investigated the equilibrium phase behaviour for a monodisperse system of Mackay icosahedra composed from a collection of Lennard-Jones interacting subparticles which is a representative nanocrystal shape (Figure 1.1) that can be formed in experiments with agglomeration inside emulsion droplets as discussed in Chapter 2. We found that from ordered or disordered initial states different thermodynamically stable phases can form. The analysis of the order by the positional and orientational pair correlation functions showed a fluid phase, a rotationally disordered crystal with an FCC crystal lattice, and a uniformly oriented crystal phase with either BCC ordering or the densest lattice packing of hard icosahedra are stabilised.

Some of these phases have already been predicted before for hard regular icosahedra using different approaches but the densest icosahedral lattice packing is yet to be confirmed experimentally. New behaviour is observed at low temperatures where energetic interactions result in preferred face to face alignment forming rotator crystal or presumably unidentifiable complex crystal arrangements. This leads to the re-entrant behaviour with increasing temperature where first a transition to the crystal occurs and then the rotator phase is formed at higher temperatures due to the prevailing excluded volume effects. However, more detailed analysis of face-to-face alignment at lower temperatures would be needed to support this and identify the possibility of complex crystal structures with larger unit cells.

Our model has a disadvantage that it takes a considerable amount of time to evaluate all the pair energies of the subparticles within the cutoff range, but it also offers several ways of generalising the components under study. For example, interesting structures to study would be those where vertices have attractions with an increased range or other properties describing functionalised interaction sites in nanocrystals which can be achieved e.g. by DNA-based ligands [48, 212] or inclusion of magnetic subparticles that can assemble under external magnetic fields [213]. This would enable us to evaluate assembly of the patchy building blocks in the form of binary icosahedral clusters with symmetric or Janus arrangements of interacting sites on the surface of clusters which have been predicted before [195].

Chapter 5

Summary

The formation of ordered superlattices from single inorganic nanoparticles separated by organic ligands has received considerable attention of scientists in the last two decades due to their diversity in structure and composition. Combinations of metallic, magnetic and semiconductor [37, 157, 180] cores in a variety of sizes and shapes such as spheres, rods, plates, cubes, octapods etc. [58, 78, 214–216] can be stabilised with organic ligands of diverse complexity from well-known thiol monolayers to DNA and polymer brushes [48, 217, 218]. This abundance of components combined with the varying environments of different assembly techniques leads to unique mechanical, optical, magnetic, electronic, and catalytic properties [49–52] of superlattices with promising biomedical and optoelectronic applications [42, 82].

Structured nanocolloids are essential in the "bottom-up" approach to constructing mesoscale materials with peculiar properties, for example photonic crystals with a range of important applications [219]. In this approach sub-micron particles self-assemble into patterns and structures across several length-scales and play a similar role to atoms and molecules in molecular crystals but on a time and length scales that are much larger and thus allow for a better control over the process [220]. This renders colloidal systems ideal models for investigation using condensed matter techniques with an ultimate goal to determine precisely the effects of microscopic properties of colloids on the macroscopic material properties. Establishing this link provides a way to design materials with targeted properties by pre-programming them in the underlying colloidal building blocks of varying shapes and interactions [56]. This strategy that is still largely unexplored is an active area of research with a huge potential as an alternative to the so far prevalent "top-down" scheme to organising matter at small scales and surpasses limitations of fabrication techniques such as optical and electron beam lithography used to produce contemporary micro- and nanoelectromechanical systems.

One assembly protocol to forming regular supraparticles is in the spherical confinement provided by emulsion droplets from which the solvent is evaporated [78]. It was demonstrated that a monodisperse collection of nano- or micro-sized colloidal particles can assemble into

well defined structures ranging from minimal energy Lennard-Jones clusters, Mackay icosahedra, rhombicosidodecahedral and close-packed FCC structures [26, 81]. In this work we explored the possible arrangements that could be obtained using simple bimodal mixtures of spherical gold nanoparticles combined with this assembly technique. Although the attention has in the recent years turned to assembly of colloidal particles with anisotropic shapes and patchy interaction spots that are more promising and have already demonstrated the ability to produce a plethora of different phases [56, 221–223], we show here that when bimodal spherical mixtures are used in confinement this can lead to variable structures with potential applications as well.

We have at first considered a bimodal mixture of up to 200 spherical particles with unequal attractions and demonstrated that different structures can form in the protocol dominated by energy minimisation. Depending on the inter-species interactions either clusters with core-shell or Janus-type phase separated structures formed overall for a variety of cluster sizes and compositions. When Berthelot rule is used the clusters have polyhedral features similar to Mackay icosahedra that appear at specific cluster sizes but are independent of cluster compositions and result in a large range of attraction ratios. Clusters' shells can additionally organise in Janus-type separation or symmetric patches based on the triangles or vertices of an icosahedron and yield symmetries that are interesting as building blocks in assembly of colloidal crystals. Mixtures of particles with different attractions in confinement could be used as a general path to building structured supraparticles when energetic effects dominate the entropic contributions and particles are mobile enough to assemble their minimal energy configurations.

A more complex situation appears when a bimodal mixture of particles with different sizes is considered in spherical confinement. Here entropic effect are important and drive a mixture with a diameter ratio 1/2 and concentration ratio 1/13 to assemble into a complex AB_{13} crystal lattice. However, the effects of assembly environment through a choice of surfactant or the application of external pressure can lead to different formation pathways and results in contrasting structures. We demonstrate that this is a consequence of changes in particle solubilities and varying particle pair interactions with the pressure that can be used to select Janus, core-shell and AB_{13} supraparticle structures. Pressure affects the solubility of particles probably by changing the properties of ligand monolayers on their surfaces but more detailed studies are required to unveil the precise mechanism behind this relation.

Describing supraparticles as rigid assemblies of interactions sites enables us to study bulk phase behaviour in a diverse set of structures. A variable-box Monte Carlo algorithm was used to test this by simulating Mackay icosahedra composed of 42 Lennard-Jones particles on its surface. A scan of phase diagram showed that varying temperature and pressure can be used to choose between rotator crystal, crystal and liquid phases. Increasing temperature

led to a transition from rotator crystal with FCC positional order to a BCC crystal and back to FCC rotator crystal. At specific parameters densest lattice packing of hard icosahedra was reproduced. A more sophisticated behaviour is expected for models with binary mixtures of subparticles that can be used to mimic patchy particles and analyse properties of nanocrystal solids composed of them.

We have seen that agglomeration into predicted binary structures could provide a convenient assembly protocol for building blocks used in colloidal molecules and crystals where well-defined and monodisperse structures are required. Our studies have shown binary mixtures in confinement can lead to such intriguing supraparticles with precise structures. A further experimental study in a system of nanoparticles with heterogeneous inorganic cores could produce clusters comparable to the predicted minimal energy clusters for particles with dissimilar attractions. Varying ligand lengths on the otherwise identical metallic cores of nanoparticles are also expected to provide a way of constructing such clusters.

Mixtures of binary particles in a wider range of size and concentration ratios are expected to lead to a richer diversity of superlattices similar to the one observed in thin films [156]. The assortment of structures could additionally be enlarged by including disparate combinations of nanoparticles cores and shapes or eventually also ternary mixtures. The effect of pressure is to be determined in other techniques that are used to assemble nanoparticles, especially in the widespread process of evaporation in thin films. Detailed studies of the effect of pressure on the stabilising ligand monolayers are necessary to understand the complex behaviour of nanoparticles. Finally, the crystallisation pathway to form a complex AB_{13} crystal lattice from a disordered fluid phase could enable the detailed study of its formation mechanism and agglomeration kinetics.

References

[1] R. G. Jones, E. S. Wilks, W. V. Metanomski, J. Kahovec, M. Hess, R. Stepto, and T. Kitayama, eds., *Compendium of Polymer Terminology and Nomenclature* (The Royal Society of Chemistry, 2009).

[2] D. F. Evans and H. Wennerström, *The Colloidal Domain: Where Physics, Chemistry, Biology, and Technology Meet*, 2nd ed. (Wiley-VCH, 1999).

[3] R. A. Jones, *Soft condensed matter* (Oxford University Press, 2002).

[4] P.-G. De Gennes, *Soft matter*, Reviews of Modern Physics **64**, 645 (1992).

[5] R. Brown, *XXVII. A brief account of microscopical observations made in the months of June, July and August 1827, on the particles contained in the pollen of plants; and on the general existence of active molecules in organic and inorganic bodies*, Philosophical Magazine **4**, 161 (1828).

[6] T. Graham, *Liquid diffusion applied to analysis*, Philosophical Transactions of the Royal Society of London **151**, 183 (1861).

[7] J. P. F. Lagerwall and G. Scalia, *Liquid Crystals with Nano and Microparticles: (In 2 Volumes)*, Series in Soft Condensed Matter (WSPC, 2016).

[8] G. M. Whitesides and B. Grzybowski, *Self-assembly at all scales*, Science **295**, 2418 (2002).

[9] G. Whitesides, J. Mathias, and C. Seto, *Molecular self-assembly and nanochemistry: a chemical strategy for the synthesis of nanostructures*, Science **254**, 1312 (1991).

[10] A. V. Pinheiro, D. Han, W. M. Shih, and H. Yan, *Challenges and opportunities for structural DNA nanotechnology*, Nature Nanotechnology **6**, 763 (2011).

[11] I. A. Chen and P. Walde, *From self-assembled vesicles to protocells*, Cold Spring Harbor Perspectives in Biology **2**, a002170 (2010).

[12] K. A. Dill and J. L. MacCallum, *The protein-folding problem, 50 years on*, Science **338**, 1042 (2012).

[13] M. Schliwa and G. Woehlke, *Molecular motors*, Nature **422**, 759 (2003).

[14] M. M. Stevens and J. H. George, *Exploring and engineering the cell surface interface*, Science **310**, 1135 (2005).

[15] S. Maude, E. Ingham, and A. Aggeli, *Biomimetic self-assembling peptides as scaffolds for soft tissue engineering*, Nanomedicine **8**, 823 (2013).

[16] W. K. Kegel and P. van der Schoot, *Physical regulation of the self-assembly of tobacco mosaic virus coat protein*, Biophysical Journal **91**, 1501 (2006).

[17] S.-H. Kim, S. Y. Lee, S.-M. Yang, and G.-R. Yi, *Self-assembled colloidal structures for photonics*, NPG Asia Materials **3**, 25 (2011).

[18] L. Onsager, *The effects of shape on the interaction of colloidal particles*, Annals of the New York Academy of Sciences **51**, 627 (1949).

[19] D. Frenkel, *Order through entropy*, Nature Materials **14**, 9 (2015).

[20] P. N. Pusey and W. Van Megen, *Phase behaviour of concentrated suspensions of nearly hard colloidal spheres*, Nature **320**, 340 (1986).

[21] D. Frenkel, *Entropy-driven phase transitions*, Physica A: Statistical Mechanics and its Applications **263**, 26 (1999).

[22] D. V. Talapin and E. V. Shevchenko, *Introduction: Nanoparticle Chemistry*, Chemical Reviews **116**, 10343 (2016).

[23] M. A. Boles, M. Engel, and D. V. Talapin, *Self-assembly of colloidal nanocrystals: From intricate structures to functional materials*, Chemical Reviews **116**, 11220 (2016).

[24] T. P. Bigioni, X.-M. Lin, T. T. Nguyen, E. I. Corwin, T. A. Witten, and H. M. Jaeger, *Kinetically driven self assembly of highly ordered nanoparticle monolayers*, Nature Materials **5**, 265 (2006).

[25] Y. Cui, M. T. Björk, J. A. Liddle, C. Sönnichsen, B. Boussert, and A. P. Alivisatos, *Integration of colloidal nanocrystals into lithographically patterned devices*, Nano Letters **4**, 1093 (2004).

[26] J. Lacava, P. Born, and T. Kraus, *Nanoparticle clusters with Lennard-Jones geometries*, Nano Letters **12**, 3279 (2012).

[27] K. Miszta, J. De Graaf, G. Bertoni, D. Dorfs, R. Brescia, S. Marras, L. Ceseracciu, R. Cingolani, R. Van Roij, M. Dijkstra, *et al.*, *Hierarchical self-assembly of suspended branched colloidal nanocrystals into superlattice structures*, Nature Materials **10**, 872 (2011).

[28] Y. Wang, O. Zeiri, M. Raula, B. Le Ouay, F. Stellacci, and I. A. Weinstock, *Host–guest chemistry with water-soluble gold nanoparticle supraspheres*, Nature Nanotechnology **12**, 170 (2017).

[29] V. A. Parsegian, *Van der Waals forces: a handbook for biologists, chemists, engineers, and physicists* (Cambridge University Press, 2005).

[30] A. Ambrosetti, N. Ferri, R. A. DiStasio, and A. Tkatchenko, *Wavelike charge density fluctuations and van der Waals interactions at the nanoscale*, Science **351**, 1171 (2016).

[31] F. London, *The general theory of molecular forces*, Transactions of the Faraday Society **33**, 8b (1937).

[32] H. Hamaker, *The London—van der Waals attraction between spherical particles*, physica **4**, 1058 (1937).

[33] J.-P. Hansen and I. McDonald, *Theory of Simple Liquids* (Academic Press, 2006).

[34] J. N. Israelachvili, *Intermolecular and surface forces* (Academic press, 2015).

[35] D. Nykypanchuk, M. M. Maye, D. Van Der Lelie, and O. Gang, *DNA-guided crystallization of colloidal nanoparticles*, Nature **451**, 549 (2008).

[36] C. Stowell and B. A. Korgel, *Self-assembled honeycomb networks of gold nanocrystals*, Nano Letters **1**, 595 (2001).

[37] F. Reincke, S. G. Hickey, W. K. Kegel, and D. Vanmaekelbergh, *Spontaneous assembly of a monolayer of charged gold nanocrystals at the water/oil interface*, Angewandte Chemie International Edition **43**, 458 (2004).

[38] J. U. Kim and M. W. Matsen, *Interaction between polymer-grafted particles*, Macromolecules **41**, 4435 (2008).

[39] A. Widmer-Cooper and P. L. Geissler, *Ligand-Mediated Interactions between Nanoscale Surfaces Depend Sensitively and Nonlinearly on Temperature, Facet Dimensions, and Ligand Coverage*, ACS Nano **10**, 1877 (2016).

[40] P. Schapotschnikow, R. Pool, and T. J. Vlugt, *Molecular simulations of interacting nanocrystals*, Nano Letters **8**, 2930 (2008).

[41] B. W. Goodfellow, Y. Yu, C. A. Bosoy, D.-M. Smilgies, and B. A. Korgel, *The role of ligand packing frustration in body-centered cubic (bcc) superlattices of colloidal nanocrystals*, Journal of Physical Chemistry Letters **6**, 2406 (2015).

[42] M. A. Boles, D. Ling, T. Hyeon, and D. V. Talapin, *The surface science of nanocrystals*, Nature Materials **15**, 141 (2016).

[43] G. F. Mancini, T. Latychevskaia, F. Pennacchio, J. Reguera, F. Stellacci, and F. Carbone, *Order/disorder dynamics in a dodecanethiol-capped gold nanoparticles supracrystal by small-angle ultrafast electron diffraction*, Nano Letters **16**, 2705 (2016).

[44] P. Schapotschnikow and T. J. Vlugt, *Understanding interactions between capped nanocrystals: three-body and chain packing effects*, Journal of Chemical Physics **131**, 124705 (2009).

[45] A. Travesset, *Binary nanoparticle superlattices of soft-particle systems*, Proceedings of the National Academy of Sciences of the United States of America **112**, 9563 (2015).

[46] A. Travesset, *Topological structure prediction in binary nanoparticle superlattices*, Soft Matter **13**, 147 (2017).

[47] O. Gang and A. V. Tkachenko, *DNA-programmable particle superlattices: Assembly, phases, and dynamic control*, MRS Bulletin **41**, 381–387 (2016).

[48] W. B. Rogers, W. M. Shih, and V. N. Manoharan, *Using DNA to program the self-assembly of colloidal nanoparticles and microparticles*, Nature Reviews Materials **1**, 16008 (2016).

[49] J. Chen, A. Dong, J. Cai, X. Ye, Y. Kang, J. M. Kikkawa, and C. B. Murray, *Collective dipolar interactions in self-assembled magnetic binary nanocrystal superlattice membranes*, Nano Letters **10**, 5103 (2010).

[50] J. J. Urban, D. V. Talapin, E. V. Shevchenko, C. R. Kagan, and C. B. Murray, *Synergism in binary nanocrystal superlattices leads to enhanced p-type conductivity in self-assembled PbTe/Ag_2Te thin films*, Nature Materials **6**, 115 (2007).

[51] Y. Kang, X. Ye, J. Chen, Y. Cai, R. E. Diaz, R. R. Adzic, E. A. Stach, and C. B. Murray, *Design of Pt–Pd binary superlattices exploiting shape effects and synergistic effects for oxygen reduction reactions*, Journal of the American Chemical Society **135**, 42 (2013).

[52] C. L. Poyser, T. Czerniuk, A. Akimov, B. T. Diroll, E. A. Gaulding, A. S. Salasyuk, A. J. Kent, D. R. Yakovlev, M. Bayer, and C. B. Murray, *Coherent acoustic phonons in colloidal semiconductor nanocrystal superlattices*, ACS Nano **10**, 1163 (2016).

[53] Z. Nie, A. Petukhova, and E. Kumacheva, *Properties and emerging applications of self-assembled structures made from inorganic nanoparticles*, Nature Nanotechnology **5**, 15 (2010).

[54] S. Mann, *Self-assembly and transformation of hybrid nano-objects and nanostructures under equilibrium and non-equilibrium conditions*, Nature Materials **8**, 781 (2009).

[55] A. S. Arico, P. Bruce, B. Scrosati, J. M. Tarascon, and W. V. Schalkwijk, *Nanostructured materials for advanced energy conversion and storage devices*, Nature Materials **4**, 366 (2005).

[56] S. C. Glotzer and M. J. Solomon, *Anisotropy of building blocks and their assembly into complex structures.*, Nature Materials **6**, 557 (2007).

[57] A. A. Antipov, S. Arakelian, S. Kutrovskaya, A. Kucherik, and T. Vartanian, *Deposition of bimetallic Au/Ag clusters by the method of laser deposition of nanoparticles from colloidal systems*, Optics and Spectroscopy **116**, 324 (2014).

[58] K. Park and R. a. Vaia, *Synthesis of complex Au/Ag nanorods by controlled overgrowth*, Advanced Materials **20**, 3882 (2008).

[59] C. J. Serpell, J. Cookson, D. Ozkaya, and P. D. Beer, *Core@shell bimetallic nanoparticle synthesis via anion coordination*, Nature Chemistry **3**, 478 (2011).

[60] M. P. Allen and D. J. Tildesley, *Computer simulation of liquids, Second Edition* (Oxford university press, 2017).

[61] D. Frenkel and B. Smit, *Understanding molecular simulation: from algorithms to applications* (Academic Press, San Diego, 2001).

[62] D. P. Landau and K. Binder, *A guide to Monte Carlo simulations in statistical physics* (Cambridge university press, 2014).

[63] E. Winsberg, *Computer Simulations in Science*, in *The Stanford Encyclopedia of Philosophy*, edited by E. N. Zalta (Metaphysics Research Lab, Stanford University, 2015) summer 2015 ed.

[64] N. Metropolis and S. Ulam, *The monte carlo method*, Journal of the American Statistical Association **44**, 335 (1949).

[65] N. Metropolis, A. W. Rosenbluth, M. N. Rosenbluth, A. H. Teller, and E. Teller, *Equation of state calculations by fast computing machines*, Journal of Chemical Physics **21**, 1087 (1953).

[66] W. K. Hastings, *Monte Carlo sampling methods using Markov chains and their applications*, Biometrika **57**, 97 (1970).

[67] S. Yashonath and C. Rao, *A Monte Carlo study of crystal structure transformations*, Molecular Physics **54**, 245 (1985).

[68] B. J. Alder and T. E. Wainwright, *Studies in molecular dynamics. I. General method*, Journal of Chemical Physics **31**, 459 (1959).

[69] S. Nosé, *A unified formulation of the constant temperature molecular dynamics methods*, Journal of Chemical Physics **81**, 511 (1984).

[70] W. G. Hoover, *Canonical dynamics: equilibrium phase-space distributions*, Physical Review A **31**, 1695 (1985).

[71] K. Sattler, *Binary metal alloy clusters*, Zeitschrift für Physik D Atoms, Molecules and Clusters **3**, 223 (1986).

[72] F. Baletto and R. Ferrando, *Structural properties of nanoclusters: Energetic, thermodynamic, and kinetic effects*, Reviews of Modern Physics **77**, 371 (2005).

[73] D. Chakrabarti, S. N. Fejer, and D. J. Wales, *Chapter 3: Self-Assembly of Nanoclusters: An Energy Landscape Perspective*, in *Computational Nanoscience* (The Royal Society of Chemistry, 2011) pp. 58–81.

[74] C. Singh, P. K. Ghorai, M. A. Horsch, A. M. Jackson, R. G. Larson, F. Stellacci, and S. C. Glotzer, *Entropy-Mediated Patterning of Surfactant-Coated Nanoparticles and Surfaces*, Physical Review Letters **99**, 226106 (2007).

[75] A. Walther, M. Hoffmann, and A. Müller, *Emulsion Polymerization Using Janus Particles as Stabilizers*, Angewandte Chemie International Edition **47**, 711 (2008).

[76] A. Bachinger, S. Ivanovici, and G. Kickelbick, *Formation of Janus TiO_2 Nanoparticles by a Pickering Emulsion Approach Applying Phosphonate Coupling Agents*, Journal of Nanoscience and Nanotechnology **11**, 8599 (2011).

[77] V. N. Manoharan, *Colloidal spheres confined by liquid droplets: Geometry, physics, and physical chemistry*, Solid State Communications **139**, 557 (2006).

[78] V. N. Manoharan, M. T. Elsesser, and D. J. Pine, *Dense Packing and Symmetry in Small Clusters of Microspheres*, Science **301**, 483 (2003).

[79] O. Chen, L. Riedemann, F. Etoc, H. Herrmann, M. Coppey, M. Barch, C. T. Farrar, J. Zhao, O. T. Bruns, H. Wei, P. Guo, J. Cui, R. Jensen, Y. Chen, D. K. Harris, J. M. Cordero, Z. Wang, A. Jasanoff, D. Fukumura, R. Reimer, M. Dahan, R. K. Jain, and M. G. Bawendi, *Magneto-fluorescent core-shell supernanoparticles*, Nature Communications **5**, 5093 (2014).

[80] J. I. Park, T. D. Nguyen, G. de Queirós Silveira, J. H. Bahng, S. Srivastava, G. Zhao, K. Sun, P. Zhang, S. C. Glotzer, and N. A. Kotov, *Terminal supraparticle assemblies from similarly charged protein molecules and nanoparticles*, Nature Communications **5**, 3593 (2014).

[81] B. de Nijs, S. Dussi, F. Smallenburg, J. D. Meeldijk, D. J. Groenendijk, L. Filion, A. Imhof, A. van Blaaderen, and M. Dijkstra, *Entropy-driven formation of large icosahedral colloidal clusters by spherical confinement.*, Nature Materials **14**, 56 (2015).

[82] D. V. Talapin, J.-S. Lee, M. V. Kovalenko, and E. V. Shevchenko, *Prospects of colloidal nanocrystals for electronic and optoelectronic applications*, Chemical Reviews **110**, 389 (2010).

[83] S. M. Rupich, E. V. Shevchenko, M. I. Bodnarchuk, B. Lee, and D. V. Talapin, *Size-dependent multiple twinning in nanocrystal superlattices*, Journal of the American Chemical Society **132**, 289 (2009).

[84] J. C. Love, L. A. Estroff, J. K. Kriebel, R. G. Nuzzo, and G. M. Whitesides, *Self-Assembled Monolayers of Thiolates on Metals as a Form of Nanotechnology*, Chemical Reviews **105**, 1103 (2005).

[85] S. Casalini, C. A. Bortolotti, F. Leonardi, and F. Biscarini, *Self-assembled monolayers in organic electronics*, Chemical Society Reviews **46**, 40 (2017).

[86] D. Napper, *Steric stabilization*, Journal of Colloid and Interface Science **58**, 390 (1977).

[87] P. J. Flory and W. R. Krigbaum, *Statistical Mechanics of Dilute Polymer Solutions. II*, The Journal of Chemical Physics **18**, 1086 (1950).

[88] M. A. Boles and D. V. Talapin, *Self-Assembly of Tetrahedral CdSe Nanocrystals: Effective "Patchiness" via Anisotropic Steric Interaction*, Journal of the American Chemical Society **136**, 5868 (2014).

[89] Y. Yang, H. Qin, and X. Peng, *Intramolecular Entropy and Size-Dependent Solution Properties of Nanocrystal–Ligands Complexes*, Nano Letters **16**, 2127 (2016).

[90] N. Horst and A. Travesset, *Prediction of binary nanoparticle superlattices from soft potentials*, Journal of Chemical Physics **144**, 014502 (2016).

[91] C. A. Silvera Batista, R. G. Larson, and N. A. Kotov, *Nonadditivity of nanoparticle interactions*, Science **350**, 1242477 (2015).

[92] D. Vanmaekelbergh, *Self-assembly of colloidal nanocrystals as route to novel classes of nanostructured materials*, Nano Today **6**, 419 (2011).

[93] M. V. Kovalenko, L. Manna, A. Cabot, Z. Hens, D. V. Talapin, C. R. Kagan, V. I. Klimov, A. L. Rogach, P. Reiss, D. J. Milliron, P. Guyot-Sionnnest, G. Konstantatos, W. J. Parak, T. Hyeon, B. A. Korgel, C. B. Murray, and W. Heiss, *Prospects of Nanoscience with Nanocrystals*, ACS Nano **9**, 1012 (2015).

[94] S. Badaire, C. Cottin-Bizonne, and A. D. Stroock, *Experimental Investigation of Selective Colloidal Interactions Controlled by Shape, Surface Roughness, and Steric Layers*, Langmuir **24**, 11451 (2008).

[95] D. J. Kraft, R. Ni, F. Smallenburg, M. Hermes, K. Yoon, D. A. Weitz, A. van Blaaderen, J. Groenewold, M. Dijkstra, and W. K. Kegel, *Surface roughness directed self-assembly of patchy particles into colloidal micelles*, Proceedings of the National Academy of Sciences of the United States of America **109**, 10787 (2012).

[96] J. Lacava, A.-A. Ouali, B. Raillard, and T. Kraus, *On the behaviour of nanoparticles in oil-in-water emulsions with different surfactants*, Soft Matter **10**, 1696 (2014).

[97] J. P. Doye and D. J. Wales, *Structural consequences of the range of the interatomic potential a menagerie of clusters*, Journal of the Chemical Society, Faraday Transactions **93**, 4233 (1997).

[98] B. Raoult, J. Farges, M. De Feraudy, and G. Torchet, *Comparison between icosahedral, decahedral and crystalline Lennard-Jones models containing 500 to 6000 atoms*, Philosophical Magazine B: Physics of Condensed Matter: Structural, Electronic, Optical and Magnetic Properties **60**, 881 (1989).

[99] J. P. Doye, D. J. Wales, and R. S. Berry, *The effect of the range of the potential on the structures of clusters*, Journal of Chemical Physics **103**, 4234 (1995).

[100] D. J. Wales and J. P. K. Doye, *Global Optimization by Basin-Hopping and the Lowest Energy Structures of Lennard-Jones Clusters Containing up to 110 Atoms*, Journal of Physical Chemistry A **101**, 5111 (1997).

[101] M. A. Boles and D. V. Talapin, *Many-body effects in nanocrystal superlattices: departure from sphere packing explains stability of binary phases*, Journal of the American Chemical Society **137**, 4494 (2015).

[102] J. E. Jones, *On the determination of molecular fields. II. From the equation of state of a gas*, Proceedings of the Royal Society of London A: Mathematical, Physical and Engineering Sciences **106**, 463 (1924).

[103] R. Eisenschitz and F. London, *Über das Verhältnis der van der Waalsschen Kräfte zu den homöopolaren Bindungskräften*, Zeitschrift für Physik **60**, 491 (1930).

[104] T. Cosgrove, *Colloid science: principles, methods and applications* (John Wiley & Sons, 2010).

[105] D. Schebarchov and D. J. Wales, *Communication: a new paradigm for structure prediction in multicomponent systems.*, Journal of Chemical Physics **139**, 221101 (2013).

[106] D. Schebarchov and D. J. Wales, *Structure Prediction for Multicomponent Materials Using Biminima*, Physical Review Letters **113**, 156102 (2014).

[107] T. V. Bogdan, D. J. Wales, and F. Calvo, *Equilibrium thermodynamics from basin-sampling*, Journal of Chemical Physics **124**, 044102 (2006).

[108] D. Wales, *Energy landscapes: Applications to clusters, biomolecules and glasses* (Cambridge University Press, 2003).

[109] Z. Li and H. A. Scheraga, *Monte Carlo-minimization approach to the multiple-minima problem in protein folding*, Proceedings of the National Academy of Sciences of the United States of America **84**, 6611 (1987).

[110] S. Goedecker, *Minima hopping: An efficient search method for the global minimum of the potential energy surface of complex molecular systems*, Journal of Chemical Physics **120**, 9911 (2004).

[111] G. G. Rondina and J. L. Da Silva, *Revised basin-hopping Monte Carlo algorithm for structure optimization of clusters and nanoparticles*, Journal of Chemical Information and Modeling **53**, 2282 (2013).

[112] G. M. Morris, D. S. Goodsell, R. S. Halliday, R. Huey, W. E. Hart, R. K. Belew, A. J. Olson, *et al.*, *Automated docking using a Lamarckian genetic algorithm and an empirical binding free energy function*, Journal of Computational Chemistry **19**, 1639 (1998).

[113] A. L.-S. Chua, N. A. Benedek, L. Chen, M. W. Finnis, and A. P. Sutton, *A genetic algorithm for predicting the structures of interfaces in multicomponent systems*, Nature Materials **9**, 418 (2010).

[114] J. Jellinek and E. Krissinel, *Ni_nAl_m alloy clusters: analysis of structural forms and their energy ordering*, Chemical Physics Letters **258**, 283 (1996).

[115] R. Ferrando, A. Fortunelli, and R. L. Johnston, *Searching for the optimum structures of alloy nanoclusters*, Physical Chemistry Chemical Physics **10**, 640 (2008).

[116] J. P. K. Doye and L. Meyer, *The structure of binary Lennard-Jones clusters: The effects of atomic size ratio*, arXiv:cond-mat/0604250 (2006).

[117] I. Kolossváry and K. J. Bowers, *Global optimization of additive potential energy functions: Predicting binary Lennard-Jones clusters*, Physical Review E **82**, 056711 (2010).

[118] D. J. Wales, J. P. K. Doye, A. Dullweber, M. P. Hodges, F. Y. Naumkin, F. Calvo, J. Hernández-Rojas, and T. F. Middleton, *The Cambridge Cluster Database*, `http://www-wales.ch.cam.ac.uk/CCD.html` (2001).

[119] J. P. K. Doye and L. Meyer, *Mapping the magic numbers in binary Lennard-Jones clusters*, Physical Review Letters **95**, 1 (2005).

[120] S. M. Woodley and R. Catlow, *Crystal structure prediction from first principles*, Nature Materials **7**, 937 (2008).

[121] R. Ferrando, J. Jellinek, and R. L. Johnston, *Nanoalloys: from theory to applications of alloy clusters and nanoparticles*, Chemical Reviews **108**, 845 (2008).

[122] K. A. Dill, S. B. Ozkan, M. S. Shell, and T. R. Weikl, *The protein folding problem*, Annual Review of Biophysics **37**, 289 (2008).

[123] G. E. Santoro, R. Martoňák, E. Tosatti, and R. Car, *Theory of quantum annealing of an Ising spin glass*, Science **295**, 2427 (2002).

[124] M. Hoare, *Structure and dynamics of simple microclusters*, Advances in Chemical Physics **40**, 49 (1979).

[125] J. P. Doye, M. A. Miller, and D. J. Wales, *The double-funnel energy landscape of the 38-atom Lennard-Jones cluster*, Journal of Chemical Physics **110**, 6896 (1999).

[126] J. P. Doye, M. A. Miller, and D. J. Wales, *Evolution of the potential energy surface with size for Lennard-Jones clusters*, Journal of Chemical Physics **111**, 8417 (1999).

[127] R. L. Johnston, *Evolving better nanoparticles: genetic algorithms for optimising cluster geometries*, Dalton Transactions **22**, 4193 (2003).

[128] A. R. Oganov and C. W. Glass, *Crystal structure prediction using ab initio evolutionary techniques: Principles and applications*, Journal of Chemical Physics **124**, 244704 (2006).

[129] D. J. Wales and H. A. Scheraga, *Global optimization of clusters, crystals, and biomolecules*, Science **285**, 1368 (1999).

[130] Y. Xiang, L. Cheng, W. Cai, and X. Shao, *Structural distribution of Lennard-Jones clusters containing 562 to 1000 atoms*, Journal of Physical Chemistry A **108**, 9516 (2004).

[131] B. W. Kernighan and S. Lin, *An efficient heuristic procedure for partitioning graphs*, The Bell System Technical Journal **49**, 291 (1970).

[132] T. H. Cormen, C. E. Leiserson, R. L. Rivest, and C. Stein, *Introduction to algorithms, 3rd ed.* (MIT press, 2009).

[133] J. Nocedal, *Updating quasi-Newton matrices with limited storage*, Mathematical Programming **35**, 773 (1980).

[134] D. C. Liu and J. Nocedal, *On the limited memory BFGS method for large scale optimization*, Mathematical Programming **45**, 503 (1989).

[135] W. H. Press, S. A. Teukolsky, W. T. Vetterling, and B. P. Flannery, *Numerical recipes third edition: the art of scientific computing*, Cambridge University Press **32**, 10013 (2007).

[136] A. S. Lewis and M. L. Overton, *Nonsmooth optimization via quasi-Newton methods*, Mathematical Programming **141**, 135 (2013).

[137] J. L. Morales and J. Nocedal, *Remark on "Algorithm 778: L-BFGS-B: Fortran subroutines for large-scale bound constrained optimization"*, ACM Transactions on Mathematical Software **38**, 7 (2011).

[138] X. Lai, R. Xu, and W. Huang, *Geometry optimization of bimetallic clusters using an efficient heuristic method*, Journal of Chemical Physics **135**, 164109 (2011).

[139] X. G. Shao, *Global minimal energies and coordinates of the LJ clusters up to n = 1610*, `http://chinfo.nankai.edu.cn/chmm/pubmats/LJ/ljstructures` (2014).

[140] P. J. Steinhardt, D. R. Nelson, and M. Ronchetti, *Bond-orientational order in liquids and glasses*, Physical Review B **28**, 784 (1983).

[141] S. Dorosz, T. Voigtmann, and T. Schilling, *Dissipation by a crystallization process*, Europhysics Letters **113**, 10004 (2016).

[142] L. D. Landau and E. M. Lifshitz, *Quantum Mechanics, 3rd Edition, Non-Relativistic Theory* (Butterworth-Heinemann, 1981).

[143] Y. Wang, S. Teitel, and C. Dellago, *Melting of icosahedral gold nanoclusters from molecular dynamics simulations*, Journal of Chemical Physics **122**, 214722 (2005).

[144] I. D. Morrison and S. Ross, *Colloidal dispersions: suspensions, emulsions, and foams* (Wiley-Interscience, 2002).

[145] D. Berthelot, *Sur le mélange des gaz*, Comptes Rendus **126**, 1703 (1898).

[146] D. Boda and D. Henderson, *The effects of deviations from Lorentz–Berthelot rules on the properties of a simple mixture*, Molecular Physics **106**, 2367 (2008).

[147] *Minimal energy binary Lennard-Jones clusters*, `http://softmattertheory.lu/clusters.html` (2016).

[148] A. L. Mackay, *A dense non-crystallographic packing of equal spheres*, Acta Crystallographica **15**, 916 (1962).

[149] M. Schmitt, J. Zhang, J. Lee, B. Lee, X. Ning, R. Zhang, A. Karim, R. F. Davis, K. Matyjaszewski, and M. R. Bockstaller, *Polymer ligand–induced autonomous sorting and reversible phase separation in binary particle blends*, Science Advances **2** (2016), 10.1126/sciadv.1601484.

[150] B. Blaiszik, S. Kramer, S. Olugebefola, J. Moore, N. Sottos, and S. White, *Self-Healing Polymers and Composites*, Annual Review of Materials Research **40**, 179 (2010).

[151] A.-P. Hynninen, J. H. Thijssen, E. C. Vermolen, M. Dijkstra, and A. Van Blaaderen, *Self-assembly route for photonic crystals with a bandgap in the visible region*, Nature Materials **6**, 202 (2007).

[152] A. Alexeev, W. E. Uspal, and A. C. Balazs, *Harnessing Janus Nanoparticles to Create Controllable Pores in Membranes*, ACS Nano **2**, 1117 (2008).

[153] N. Kern and D. Frenkel, *Fluid–fluid coexistence in colloidal systems with short-ranged strongly directional attraction*, Journal of Chemical Physics **118**, 9882 (2003).

[154] F. Romano and F. Sciortino, *Patterning symmetry in the rational design of colloidal crystals*, Nature Communications **3**, 975 (2012).

[155] O. Velev, K. Furusawa, and K. Nagayama, *Assembly of latex particles by using emulsion droplets as templates. 2. Ball-like and composite aggregates*, Langmuir **12**, 2385 (1996).

[156] E. V. Shevchenko, D. V. Talapin, N. A. Kotov, S. O'Brien, and C. B. Murray, *Structural diversity in binary nanoparticle superlattices*, Nature **439**, 55 (2006).

[157] W. H. Evers, B. D. Nijs, L. Filion, S. Castillo, M. Dijkstra, and D. Vanmaekelbergh, *Entropy-driven formation of binary semiconductor-nanocrystal superlattices*, Nano Letters **10**, 4235 (2010).

[158] K. Whitham, J. Yang, B. H. Savitzky, L. F. Kourkoutis, F. Wise, and T. Hanrath, *Charge transport and localization in atomically coherent quantum dot solids*, Nature Materials **15**, 557 (2016).

[159] S. Wooh, H. Huesmann, M. N. Tahir, M. Paven, K. Wichmann, D. Vollmer, W. Tremel, P. Papadopoulos, and H.-J. Butt, *Synthesis of mesoporous supraparticles on superamphiphobic surfaces*, Advanced Materials **27**, 7338 (2015).

[160] S.-H. Hu and X. Gao, *Nanocomposites with Spatially Separated Functionalities for Combined Imaging and Magnetolytic Therapy*, Journal of the American Chemical Society **132**, 7234 (2010).

[161] M. Lattuada and T. A. Hatton, *Synthesis, properties and applications of Janus nanoparticles*, Nano Today **6**, 286 (2011).

[162] M. R. Hoffmann, S. T. Martin, W. Choi, and D. W. Bahnemann, *Environmental applications of semiconductor photocatalysis*, Chemical Reviews **95**, 69 (1995).

[163] A. Schofield, P. Pusey, and P. Radcliffe, *Stability of the binary colloidal crystals AB_2 and AB_{13}*, Physical Review E **72**, 031407 (2005).

[164] T. Kister, M. Mravlak, T. Schilling, and T. Kraus, *Pressure-controlled formation of crystalline, Janus, and core–shell supraparticles*, Nanoscale **8**, 13377 (2016).

[165] S. Plimpton, *Fast parallel algorithms for short-range molecular dynamics*, Journal of Computational Physics **117**, 1 (1995).

[166] J. D. Weeks, D. Chandler, and H. C. Andersen, *Role of repulsive forces in determining the equilibrium structure of simple liquids*, Journal of Chemical Physics **54**, 5237 (1971).

[167] M. Eldridge, P. Madden, and D. Frenkel, *Entropy-driven formation of a superlattice in a hard-sphere binary mixture*, Nature **365**, 35 (1993).

[168] W. Shinoda, M. Shiga, and M. Mikami, *Rapid estimation of elastic constants by molecular dynamics simulation under constant stress*, Physical Review B **69**, 134103 (2004).

[169] M. E. Tuckerman, J. Alejandre, R. López-Rendón, A. L. Jochim, and G. J. Martyna, *A Liouville-operator derived measure-preserving integrator for molecular dynamics simulations in the isothermal–isobaric ensemble*, Journal of Physics A: Mathematical and General **39**, 5629 (2006).

[170] C. L. Farrow and S. J. L. Billinge, *Relationship between the atomic pair distribution function and small-angle scattering: implications for modeling of nanoparticles*, Acta Crystallographica Section A: Foundations of Crystallography **65**, 232 (2009).

[171] A. Guinier and G. Fournet, *Small-angle scattering of X-rays*, Structure of matter series (Wiley, 1955).

[172] B.-H. Wu, H.-Y. Yang, H.-Q. Huang, G.-X. Chen, and N.-F. Zheng, *Solvent effect on the synthesis of monodisperse amine-capped Au nanoparticles*, Chinese Chemical Letters **24**, 457 (2013).

[173] T. D. C. Company, *Technical Data Sheet*, Triton, `http://www.dow.com` (2015).

[174] J. Ketelaar, *The crystal structure of alloys of zinc with the alkali and alkaline earth metals and of cadmium with potassium*, Journal of Chemical Physics **5**, 668 (1937).

[175] D. P. Shoemaker, R. E. Marsh, F. J. Ewing, and L. Pauling, *Interatomic distances and atomic valences in $NaZn_{13}$*, Acta Crystallographica **5**, 637 (1952).

[176] J. Sanders, *Close-packed structures of spheres of two different sizes I. Observations on natural opal*, Philosophical Magazine A: Physics of Condensed Matter: Defects and Mechanical Properties **42**, 705 (1980).

[177] M. Murray and J. Sanders, *Close-packed structures of spheres of two different sizes II. The packing densities of likely arrangements*, Philosophical Magazine A: Physics of Condensed Matter: Defects and Mechanical Properties **42**, 721 (1980).

[178] S. Hachisu and S. Yoshimura, *Optical demonstration of crystalline superstructures in binary mixtures of latex globules*, Nature **283**, 188 (1980).

[179] P. Bartlett, R. Ottewill, and P. Pusey, *Superlattice formation in binary mixtures of hard-sphere colloids*, Physical Review Letters **68**, 3801 (1992).

[180] F. X. Redl, K.-S. Cho, C. B. Murray, and S. O'Brien, *Three-dimensional binary superlattices of magnetic nanocrystals and semiconductor quantum dots*, Nature **423**, 968 (2003).

[181] Y. Sakamoto, Y. Kuroda, S. Toko, T. Ikeda, T. Matsui, and K. Kuroda, *Electron Microscopy Study of Binary Nanocolloidal Crystals with ico-AB_{13} Structure Made of Monodisperse Silica Nanoparticles*, Journal of Physical Chemistry C **118**, 15004 (2014).

[182] E. Hendarto and Y. B. Gianchandani, *Size sorting of floating spheres based on Marangoni forces in evaporating droplets*, Journal of Micromechanics and Microengineering **23**, 075016 (2013).

[183] J. J. Hegseth, N. Rashidnia, and A. Chai, *Natural convection in droplet evaporation*, Physical Review E **54**, 1640 (1996).

[184] W. Ramsden, *Separation of Solids in the Surface-Layers of Solutions and 'Suspensions' (Observations on Surface-Membranes, Bubbles, Emulsions, and Mechanical Coagulation). –Preliminary Account*, Proceedings of the Royal Society of London , 156 (1903).

[185] F. Menger, *Laplace pressure inside micelles*, Journal of Physical Chemistry **83**, 893 (1979).

[186] P. S. Shah, J. D. Holmes, K. P. Johnston, and B. A. Korgel, *Size-selective dispersion of dodecanethiol-coated nanocrystals in liquid and supercritical ethane by density tuning*, Journal of Physical Chemistry B **106**, 2545 (2002).

[187] S. J. Khan, F. Pierce, C. Sorensen, and A. Chakrabarti, *Self-assembly of ligated gold nanoparticles: phenomenological modeling and computer simulations*, Langmuir **25**, 13861 (2009).

[188] G. A. Sotiriou, A. M. Hirt, P.-Y. Lozach, A. Teleki, F. Krumeich, and S. E. Pratsinis, *Hybrid, silica-coated, Janus-like plasmonic-magnetic nanoparticles*, Chemistry of Materials **23**, 1985 (2011).

[189] M. A. C. Stuart, W. T. Huck, J. Genzer, M. Müller, C. Ober, M. Stamm, G. B. Sukhorukov, I. Szleifer, V. V. Tsukruk, M. Urban, *et al.*, *Emerging applications of stimuli-responsive polymer materials*, Nature Materials **9**, 101 (2010).

[190] T. Geyer, P. Born, and T. Kraus, *Switching Between Crystallization and Amorphous Agglomeration of Alkyl Thiol-Coated Gold Nanoparticles*, Physical Review Letters **109**, 128302 (2012).

[191] F. C. Frank, *A discussion on theory of liquids - Supercooling of liquids*, Proceedings of the Royal Society of London A: Mathematical, Physical and Engineering Sciences **215**, 43 (1952).

[192] D. J. Wales, *Surveying a complex potential energy landscape: Overcoming broken ergodicity using basin-sampling*, Chemical Physics Letters **584**, 1 (2013).

[193] J. Farges, M. De Feraudy, B. Raoult, and G. Torchet, *Noncrystalline structure of argon clusters. II. Multilayer icosahedral structure of Ar_N clusters* $50 < N < 750$, Journal of Chemical Physics **84**, 3491 (1986).

[194] K. H. Kuo, *Mackay, Anti-Mackay, Double-Mackay, Pseudo-Mackay, and Related Icosahedral Shell Clusters*, Structural Chemistry **13**, 221 (2002).

[195] M. Mravlak, T. Kister, T. Kraus, and T. Schilling, *Structure diagram of binary Lennard-Jones clusters*, Journal of Chemical Physics **145**, 024302 (2016).

[196] T. C. Hales, *A proof of the Kepler conjecture*, Annals of Mathematics **162**, 1065 (2005).

[197] S. Torquato and Y. Jiao, *Dense packings of the Platonic and Archimedean solids*, Nature **460**, 876 (2009).

[198] U. Betke and M. Henk, *Densest lattice packings of 3-polytopes*, Computational Geometry **16**, 157 (2000).

[199] J. H. Conway and S. Torquato, *Packing, tiling, and covering with tetrahedra*, Proceedings of the National Academy of Sciences of the United States of America **103**, 10612 (2006).

[200] P. F. Damasceno, M. Engel, and S. C. Glotzer, *Predictive self-assembly of polyhedra into complex structures*, Science **337**, 453 (2012).

[201] E. G. Teich, G. van Anders, D. Klotsa, J. Dshemuchadse, and S. C. Glotzer, *Clusters of polyhedra in spherical confinement*, Proceedings of the National Academy of Sciences of the United States of America **113**, E669 (2016).

[202] A. Lang, G. Kahl, C. N. Likos, H. Löwen, and M. Watzlawek, *Structure and thermodynamics of square-well and square-shoulder fluids*, Journal of Physics: Condensed Matter **11**, 10143 (1999).

[203] K. Binder, P. Virnau, and A. Statt, *Perspective: The Asakura Oosawa model: A colloid prototype for bulk and interfacial phase behavior*, Journal of Chemical Physics **141**, 559 (2014).

[204] W. Wood, *Monte Carlo Calculations for Hard Disks in the Isothermal-Isobaric Ensemble*, Journal of Chemical Physics **48**, 415 (1968).

[205] W. Wood, *NpT-Ensemble Monte Carlo Calculations for the Hard-Disk Fluid*, Journal of Chemical Physics **52**, 729 (1970).

[206] M. Parrinello and A. Rahman, *Crystal Structure and Pair Potentials: A Molecular-Dynamics Study*, Phys. Rev. Lett. **45**, 1196 (1980).

[207] M. Parrinello and A. Rahman, *Polymorphic transitions in single crystals: A new molecular dynamics method*, Journal of Applied Physics **52**, 7182 (1981).

[208] R. Najafabadi and S. Yip, *Observation of finite-temperature bain transformation (f.c.c. → r b.c.c.) in Monte Carlo simulation of iron*, Scripta Metallurgica **17**, 1199 (1983).

[209] L. Filion, M. Marechal, B. van Oorschot, D. Pelt, F. Smallenburg, and M. Dijkstra, *Efficient method for predicting crystal structures at finite temperature: variable box shape simulations*, Physical Review Letters **103**, 188302 (2009).

[210] F. J. Vesely, *Angular Monte Carlo integration using quaternion parameters: A spherical reference potential for CCl4*, Journal of Computational Physics **47**, 291 (1982).

[211] D. Chen, Y. Jiao, and S. Torquato, *Equilibrium phase behavior and maximally random jammed state of truncated tetrahedra*, Journal of Physical Chemistry B **118**, 7981 (2014).

[212] Y. Zhang, F. Lu, K. G. Yager, D. Van Der Lelie, and O. Gang, *A general strategy for the DNA-mediated self-assembly of functional nanoparticles into heterogeneous systems*, Nature Nanotechnology **8**, 865 (2013).

[213] L. Ye, T. Pearson, Y. Cordeau, O. Mefford, and T. Crawford, *Triggered self-assembly of magnetic nanoparticles*, Scientific Reports **6**, 23145 (2016).

[214] B. Abécassis, M. D. Tessier, P. Davidson, and B. Dubertret, *Self-assembly of CdSe nanoplatelets into giant micrometer-scale needles emitting polarized light*, Nano Letters **14**, 710 (2014).

[215] L. Rossi, S. Sacanna, W. T. Irvine, P. M. Chaikin, D. J. Pine, and A. P. Philipse, *Cubic crystals from cubic colloids*, Soft Matter **7**, 4139 (2011).

[216] M. P. Arciniegas, M. R. Kim, J. De Graaf, R. Brescia, S. Marras, K. Miszta, M. Dijkstra, R. Van Roij, and L. Manna, *Self-assembly of octapod-shaped colloidal nanocrystals into a hexagonal ballerina network embedded in a thin polymer film*, Nano Letters **14**, 1056 (2014).

[217] C. Vericat, M. Vela, G. Benitez, P. Carro, and R. Salvarezza, *Self-assembled monolayers of thiols and dithiols on gold: new challenges for a well-known system*, Chemical Society Reviews **39**, 1805 (2010).

[218] X. Ye, C. Zhu, P. Ercius, S. N. Raja, B. He, M. R. Jones, M. R. Hauwiller, Y. Liu, T. Xu, and A. P. Alivisatos, *Structural diversity in binary superlattices self-assembled from polymer-grafted nanocrystals*, Nature communications **6**, 10052 (2015).

[219] G. von Freymann, V. Kitaev, B. V. Lotsch, and G. A. Ozin, *Bottom-up assembly of photonic crystals*, Chemical Society Reviews **42**, 2528 (2013).

[220] Y. Xia and G. M. Whitesides, *Soft lithography*, Annual review of materials science **28**, 153 (1998).

[221] D. J. Lunn, J. R. Finnegan, and I. Manners, *Self-assembly of "patchy" nanoparticles: a versatile approach to functional hierarchical materials*, Chemical Science **6**, 3663 (2015).

[222] M. Kamp, M. Hermes, C. M. Van Kats, D. J. Kraft, W. K. Kegel, M. Dijkstra, and A. Van Blaaderen, *Selective depletion interactions in mixtures of rough and smooth silica spheres*, Langmuir **32**, 1233 (2016).

[223] J. R. Wolters, J. E. Verweij, G. Avvisati, M. Dijkstra, and W. K. Kegel, *Depletion-Induced Encapsulation by Dumbbell-Shaped Patchy Colloids Stabilize Microspheres against Aggregation*, Langmuir **33**, 3270 (2017).

Publications

[1] Marko Mravlak, Thomas Kister, Tobias Kraus, Tanja Schilling, *Structure diagram of binary Lennard-Jones clusters*, The Journal of Chemical Physics **145**, 024302 (2016).

[2] Thomas Kister, Marko Mravlak, Tanja Schilling, Tobias Kraus, *Pressure-controlled formation of crystalline, Janus, and core-shell supraparticles*, Nanoscale **8**, 13377-13384 (2016).

[3] Marko Mravlak and Tanja Schilling, *Phase diagram of Mackay icosahedra*, Submitted (2017).